

**PERMEABILITY CHARACTERIZATION OF SHEAR ZONES IN THE
HICKORY SANDSTONE MEMBER, RILEY FORMATION, TEXAS**

A Thesis

by

JORGE ENRIQUE NIETO CAMARGO

Submitted to the Office of Graduate Studies of
Texas A&M University
in partial fulfillment of the requirements for the degree of

MASTER OF SCIENCE

December 2004

Major Subject: Petroleum Engineering

**PERMEABILITY CHARACTERIZATION OF SHEAR ZONES IN THE
HICKORY SANDSTONE MEMBER, RILEY FORMATION, TEXAS**

A Thesis

by

JORGE ENRIQUE NIETO CAMARGO

Submitted to Texas A&M University
in partial fulfillment of the requirements
for the degree of

MASTER OF SCIENCE

Approved as to style and content by:

Jerry L. Jensen
(Co-Chair of Committee)

Frederick Chester
(Co-Chair of Committee)

Bryan Maggard
(Member)

Steve Holditch
(Head of Department)

December 2004

Major Subject: Petroleum Engineering

ABSTRACT

Permeability Characterization of Shear Zones in the Hickory Sandstone Member, Riley Formation, Texas. (December 2004)

Jorge Enrique Nieto Camargo, B.S., Universidad Industrial de Santander, Colombia, M.S., The University of Texas at Austin

Co-Chairs of Advisory Committee: Dr. Jerry L. Jensen
Dr. Frederick Chester

Reservoir compartments, typical targets for new infill locations, are commonly created by faults that may reduce or enhanced permeabilities. Faults often contain narrow zones of intense shear comprised of geometrically complex elements that reduce permeability and compartmentalize blocks as a function of time and pressure. This thesis characterizes the permeability structure of shear zones and the relationship between fault permeability, host rock properties and the relative degree of deformation.

The main objectives of this work are to (1) characterize the geometry and permeability of deformation elements within shear zones; (2) determine permeability anisotropy in shear zones according to fault characteristics and host lithology; and (3) develop a process to predict permeability anisotropy of faults in reservoirs using probabilistic approaches.

The study results give a better understanding of fluid flow behavior of shear zones and their potential to create reservoir heterogeneity and compartmentalization. Fluid flow in a reservoir with faults is controlled by variables such as fault throw, shear-zone thickness, undeformed and deformed rock permeability and the geometry of all deformation elements.

Methodology to predict permeability structure was developed using analytical and numerical simulation of selected core samples and laboratory measurements. We

found useful relationships between permeability of the host rock and highly deformed elements according to the amount of throw of the fault. The high lateral continuity of the highly deformed elements and their predictable low permeability make these elements most important in controlling permeability in shale-free and low-shale shear zones created by low displacement (subseismic) faulting.

Probe permeameter data is a precise, inexpensive and non-destructive source of permeability information that can be effectively incorporated in detailed models to investigate the effect of individual deformation elements in the whole shear zone permeability and their effect at the field scale.

DEDICATION

To my lovely wife Martha and to my daughters Maria Paula and Gaby who gave me great support and inspiration.

To my parents, Dorita & Jorge and Esperancita & Manuel because we have received the best legacy that my family could get, the confidence, support and love in all moments of our life.

To my sister Claudia for her encouragement; and to the greatest man in my family, Eduardo, who with his example makes us believe that there is always a new goal to achieve.

ACKNOWLEDGMENTS

I sincerely express my gratitude and appreciation to Dr. Jerry Jensen and Dr. Fred Chester for their assistance and guidance throughout this research.

Thank you to Dr. Bryan Maggard for his technical contribution serving as member of my graduate advisory committee.

I sincerely thank Dr. Brann Johnson for his advice, suggestions and comments during all my research. I also thank the Industrial Associates Program for providing core samples and data for this study.

Funding for my study came in part from the Petroleum Research Fund of the American Chemical Society and part from the BMFFFS project directed by Heriot-Watt University (Edinburgh). I thank both agencies for this support.

I sincerely thank my friend Loretta Coleman for her hard work in editing and my friends in Aggield; all of them were part of my great time here.

TABLE OF CONTENTS

	Page
ABSTRACT	iii
DEDICATION	v
ACKNOWLEDGMENTS.....	vi
TABLE OF CONTENTS	vii
LIST OF FIGURES.....	ix
LIST OF TABLES	xiii
 CHAPTER	
I INTRODUCTION	1
II HICKORY SHEAR ZONES AND DEFORMATION ELEMENTS.....	11
2.1 Shear Zones in Hickory Sandstone Member.....	11
2.2 Deformation Elements in the Shear Zone	18
III SHEAR ZONE PERMEABILITY AND INTERNAL ARCHITECTURE	22
3.1 Probe Permeameter Data Acquisition	22
3.2 Probe Permeameter Data Comparison with Ibañez ²⁵	38
3.3 Permeability in the Shear Zone Versus Throw	39
3.4 The Analysis of Shear Zone Thickness and Deformation Element Thickness	40
3.5 CT Scanning Integration	44
3.6 Whole Core Permeability Measurements.....	48
3.7 Hassler Permeameter Measurements.....	51

CHAPTER	Page
IV	PERMEABILITY UPSCALING USING AVERAGING TECHNIQUES57
	4.1 Upscaling Permeability at Core Scale57
	4.2 Sensitivity of Power Exponents to Facies Proportions and Permeability61
	4.3 Upscaling Permeability at Plug Scale64
V	PERMEABILITY UPSCALING USING GEOMETRICAL AND PERMEABILITY MODELING71
	5.1 Data Loading and Core Stratigraphic Grid Building71
	5.2 Permeability Modeling74
	5.3 NNR4-404 Shear Zone78
	5.4 NNR5-291 Shear Zone (Upper Section)80
	5.5 NNR4-300 Shear Zone85
	5.6 NNR3-269 Shear Zone86
VI	NUMERICAL SIMULATION AND LABORATORY MATCHING91
	6.1 Testing of the Numerical Model91
	6.2 Numerical Simulation of Detailed Models94
	6.3 Numerical Analysis Incorporating Results from Sensitivity of Power Exponents100
	6.4 The Internal Permeability Anisotropy of the Shear Zone as an Independent Body103
VII	INTEGRATION OF HIGH DETAIL CHARACTERISTICS OF SUBSEISMIC FAULT SHEAR ZONES AT FIELD SCALE109
	7.1 The Permeability Scale Issue and Proposed Method109
	7.2 Future Work115
VIII	CONCLUSIONS117
	REFERENCES120
	APPENDIX 1126
	VITA...139

LIST OF FIGURES

FIGURE	Page
1.1 Models and quantitative calibration according to clay smearing assessment. (a) and (b) for the Clay Smear Potential (CSP); (c) and (d) Shale Smear Factor (SSF); (e) and (f) for the Shale Gouge Ratio (SGR).	4
1.2 Permeability estimates for different strike-slip fault regions in the Valley of Fire State Park, Nevada. (a) a strike-slip fault with 6 m of slip, (b) a strike-slip fault with 14 m of slip, and (c) a strike-slip fault with 150 m of slip. k_1 and k_2 are the computed across and along permeability in md for the area of analysis.....	7
2.1 Regional geologic map and specific area of study.	12
2.2 Cross section with general facies description by Wilson, 2001. ²⁶	13
2.3 Western cross section through wells NNR3, NNR6, NNR5, and NNR4 showing the detailed stratigraphy and structural interpretation updated by Wilson. ²⁶	15
2.4 Selected high-fault throw samples. a) NNR4_404 b) NNR5_291. Upper picture shows interpreted deformation elements (section 2.2) , the extension of the shear zone, and relative movement.	17
2.5 Selected low-fault throw samples. a) NNR4_300 b) NNR3_269.....	19
2.6 Comparative macro- and microscopic texture of highly deformed (HDss), moderate deformed (MDss), and relatively undeformed (RUDss) sandstones.....	21
3.1 Boxplots of permeability by deformation elements.....	23
3.2 Boxplot of the ratio of logarithm of permeability between deformation elements and undeformed (host) rock.....	28
3.3 Surface map of core NNR4_404 with interpreted continuity of deformation elements and permeability transects from probe measurements.....	30

FIGURE	Page
3.4 Surface map of core NNR5_291 with interpreted continuity of deformation elements and permeability transects from probe measurements. P4, plug analyzed. Greens arrows show key deformation element contacts and control surfaces.....	33
3.5 Surface map of core NNR4_300 with interpreted continuity of deformation elements and permeability transects from probe measurements.....	36
3.6 Surface map of core NNR3_269 with interpreted continuity of deformation elements and permeability transects from probe measurements.....	37
3.7 Correlation of probe permeameter data (point measurements) for samples at NNR4_404, NNR5_291, NNR4_300 and NNR3_269	39
3.8 Permeability of HDss elements versus Fault Throw according to arithmetic and geometric means of protolith permeability.....	41
3.9 Total Shear Zone Thickness –Fault Throw Correlation	44
3.10 HD element Thickness –Fault Throw Correlation.....	45
3.11 Permeability, CT #, and deformation elements (color scale, 0 Undeformed – 6 Highly deformed clay) for the four shear zones in the Hickory	47
3.12 NNR4_404 top section. a) permeability profile, b) tangential cut at the top of the core, c) vertical cut through the core showing shear layering.....	48
3.13 Design for laboratory measurement of horizontal permeability and theoretical curve for the determination of geometrical factor. From Ref. 41.	50
3.14 Plug permeability (Hassler-sleeve Permeameter) versus overburden pressure for protolith at NNR3_269 and two calibration samples.....	54
4.1 Sensitivity of power exponents to errors in facies proportions and permeability – Core NNR4_404.....	65
4.2 Sensitivity of power exponents to errors in facies proportions and permeability – Core NNR5_291.....	66

FIGURE	Page
4.3 Sensitivity of power exponents to errors in facies proportions and permeability – Core NNR4_300.....	67
4.4 Sensitivity of power exponents to errors in facies proportions and permeability – Core NNR3_269.....	68
4.5 Probe Average permeability versus Hassler permeability for selected plugs.....	69
5.1 Modeling steps for shear zone 3-D characterization. (a) The first steps involve the CT scaling, conversion to ASCII format and loading. (b) Creation of the 3D Ct volume and integration with probe permeameter data. (c)Identification of bounding surfaces and contacts modeling a discrete volume of deformation elements for data analysis and population.	72
5.2 Variogram model showing the ellipsoid of anisotropy for core NNR3-269.	76
5.3 Scaling of geostatistical models for reproducing laboratory samples. (a) Geostatistical model of permeability. (b) Regular grid with parallel layers for simulation purposes. (c) Final volume of permeability for numerical simulation (kriging estimate for core NNR4-404).....	79
5.4 Comparison of Input and Output data for the kriging estimation of permeability in core NNR4-404	81
5.5 Comparison between input and output data for the kriging estimation of permeability in core NNR5-291.	82
5.6 Comparison between input and output data for one Sequential Gaussian Simulation realization of permeability in core NNR5-291.....	84
5.7 Comparison between input and output data for the kriging estimate, kriging with external drift and one realization of sequential gaussian simulation of permeability in core NNR4-300.	87
5.8 Kriging , Kriging with external drift, and three selected conditional simulation realizations for core NNR4-300.....	88

FIGURE	Page
5.9 Comparison between input and output data for the kriging estimate, kriging with external drift and one realization of sequential gaussian simulation of permeability in core NNR3-269.	89
5.10 Kriging , Kriging with external drift, and three selected conditional simulation realizations for core NNR3-269.	90
6.1 Vertical simulation models for numerical testing.	92
6.2 Along (a) and across (b) flow models for numerical testing.	92
6.3 Numerical simulation results for deterministic (kriging and kriging with external drift) and two randomly selected conditional simulation models.	96
6.4 Simulation and laboratory measurements for vertical flow.	97
6.5 Simulation and laboratory measurements for across flow for kriging estimates and two conditional simulations.	98
6.6 Simulation and laboratory measurements for along flow.	99
6.7 Results from reduction of permeability of HDss in core NNR3_269.	101
6.8 Results from reduction of permeability of HDss in core NNR5_291.	101
6.9 Results from reduction of permeability and increase in proportions of HDss in core NNR4_300.	102
6.10 Simulation of the independent shear zone unit in core NNR3-269. a) Permeability model. b) Pressure volume after two time steps for the vertical flow simulation.	104
6.11 Correlation between Mean and Median HDss permeability and total shear zone permeability	107
7.1 TransGen method for calculation of transmissibility multipliers. a) Schematic procedure, b) areal analysis of shear zone permeability, c) modeling steps	112
7.2 Method for the characterization of Shear zones and Integration to full field model simulation.	114

LIST OF TABLES

TABLE	Page
3.1 Proportion, Mean and Median permeability values of deformation elements.....	31
3.2 Shear Zone geometry and permeability characteristics.	42
3.3 Laboratory estimations of porosity, permeability and grain density for whole-core.....	49
3.4 Hassler permeameter plug data for various deformation element arrangements and according to different net overburden pressure (NOBP). Included here, probe permeameter data and averaging results.	52
4.1 Comparison between arithmetic, geometric, and harmonic averaging with laboratory whole-core permeability measurements.	59
4.2 Solving for power exponents matching laboratory calculations	62
6.1 Test results for a cylindrical grid (50x50x60) before simulation runs.....	95
6.2 Comparison of shear zone permeabilities from Ibañez and results of the evaluation from the two low throw samples..	106

CHAPTER I

INTRODUCTION

There are innumerable studies and discussions about the superlative importance of faults for hydrocarbon exploration and production. In exploration, they have been studied according to either their ability to facilitate migration for a time period when the fluid pressure difference is above the critical entry pressure during earthquake cycles¹, or their efficiency for entrapment of fluids.²

Some studies have concentrated the effort in the investigation of the reactivation phenomena and variable sealing character of faults occurred by changes in *in-situ* stress and the variation in the pore pressure by dynamic and fluid changes.³ Others, with small-scale analysis, have investigated the fault juxtaposition complexity and the sealing capacity and transmissibility of fault zones to identify compartments in hydrocarbon reservoirs and potential leak points along the fault plane.⁴⁻⁶

In reservoir development, more emphasis in detailed characterization has come for understanding the mechanics of faulting in addition to cross-fault juxtaposition analysis in order to develop more sophisticated models that allow to reduce risk in appraisal steps. These models also help to understand and predict fluid movement, visualize un-swept compartments and localize important untapped reserves in new and mature fields.

Many attempts have been made to characterize the effects of shear and fault zones on fluid flow. Faults can be considered as both constraints on fluid flow as well as features that enhance fluid flow in a parallel direction.^{7,8} Watts⁹ and Knipe¹⁰ have recognized four main mechanisms to account for the sealing behavior of shear zones: the juxtaposition of rocks against low-permeability sediments with high entry pressure, the reduction of grain size and porosity resulting from cataclasis, the incorporation and redistribution of clay material within the shear zone, and the synfaulting or post-faulting

This thesis follows the style and format of *Journal of Petroleum Technology*.

diagenesis that reduces porosity. Typical causes of enhanced permeability are the presence of fractures, joints, and slip surfaces.

Some authors¹¹⁻¹⁴ have concentrated their investigation on the effects of shale content into the shear zone because of the inherent sealing character of this material. From this point of view, some models such as clay smear potential (CSP),^{11,12} shale smear factor (SSF),¹³ and shale gauge ratio (SGR)¹⁴ try to predict the sealing character of diverse elements according to the thickness of impermeable layers present in the sequence (**Fig. 1.1**). A common problem in the prediction of across-fault characteristics from all these methods is that, with higher throw of faults or distance from source bed, each approach can underestimate the sealing character. This is due to the fact that all the methods are based solely on the existence of clay smearing at the location of analysis; they do not consider the effects of deformation (cataclasis) occurring during fault generation.

For example, CSP (**Fig. 1.1a**) is measured as:

$$CSP = \sum \frac{Shale_bed_thickness^2}{Distance_from_source_bed} \quad (1.1)$$

and indicates the relative amount of clay that has been smeared along the fault plane at different locations. Different threshold values have been reported for diverse reservoirs to obtain a seal.¹⁵ The threshold value for a particular reservoir will depend on cross-fault pressure gradients. Higher CSP values have been found at particular locations with higher across-fault pressure to ensure sealing behavior (**Fig. 1.1b**).¹⁵

SSF values (**Fig. 1.1c**) are defined as:

$$SSF = \frac{Throw_of_Fault}{Shale_Layer_Thickness} \quad (1.2)$$

SSF values have been calculated for specific areas such as the Gulf of Suez, Egypt by Younes¹⁶, Niger Delta by Yielding *et al.*¹⁴, and Columbus Basin, Trinidad by Gibson¹⁷; estimating SSF threshold values of 6, 7, and 8 respectively (for the case of iso across-fault pressure) (**Fig. 1.1d**).

The SGR (**Fig. 1.1e**) is defined as:

$$SGR = \frac{\sum (Shale_bed_thickness)}{Fault_Throw} \times 100\% \quad (1.3)$$

and threshold values of >15% for the Columbus Basin and >20% for the Niger Delta have been estimated by Yielding *et al.* (**Fig. 1.1f**).^{11,14}

Some studies approach the common phenomena of the presence of barriers produced by frictional wear of the host rock due to normal and shear stresses across the fault. The barriers or fault rock zones, as defined by Flodin *et al.*¹⁸, are generally bound on either side by slip surfaces which represent planar features that accommodate large amounts of displacement. Flodin *et al.*¹⁸ investigated the effect of faulted zones in the Jurassic Aztec Sandstone in Southern Nevada using highly detailed two-dimensional maps with an areal coverage of 1 to 20 square meters. Detailed permeability calculations were the output from a three-component mixture consisting of host rock, fault rock/sheared joints and joints/slip surfaces.

For extrapolation to full field scale, Flodin *et al.*¹⁸ incorporated a general correlation between slip and the width of the damage zone. For specific cases, they were able to match all production history and demonstrated the huge impact when considering a variable fault property model compared with a simplistic approach of a constant permeability fault.¹⁸

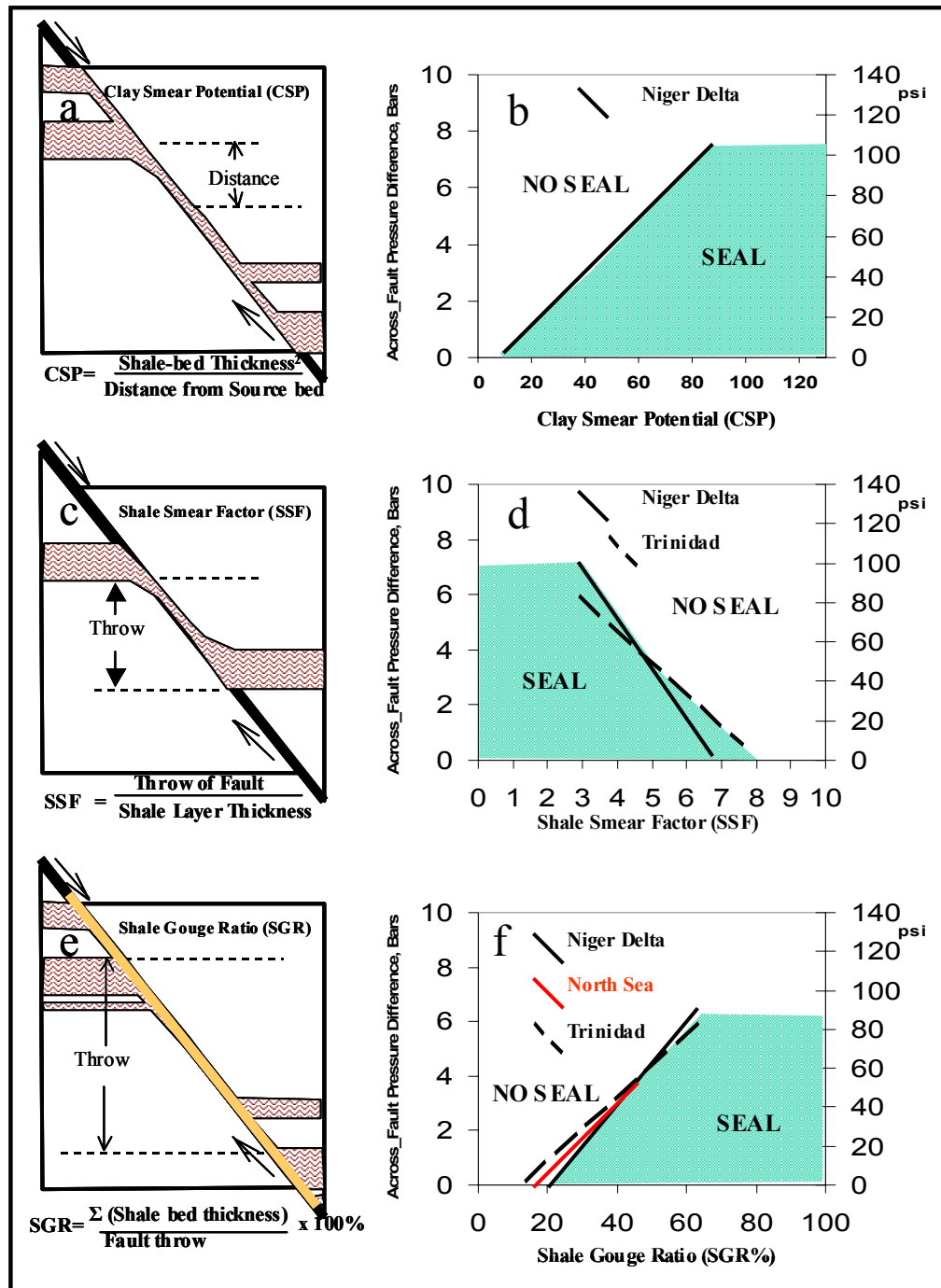


Fig.1.1 – Models and quantitative calibration according to clay smearing assessment. (a) and (b) for the Clay Smear Potential (CSP); (c) and (d) Shale Smear Factor (SSF); (e) and (f) for the Shale Gouge Ratio (SGR).

Myers¹⁹ used power averages to match numerical (flow) simulations, and found a clear relationship to finally apply a power exponent depending on fault slip. The upscaled permeability in the desired direction K_i^* is given by:

$$K_i^* = (V_j K_j^{\omega_i} + V_g K_g^{\omega_i} + V_h K_h^{\omega_i})^{1/\omega_i} \quad (1.4)$$

where V_j is the volume fraction of joints, K_j the joint permeability, V_g the volume fraction of fault rock, K_g the fault rock permeability, V_h the volume fraction of host rock, K_h the host rock permeability. ω_i , the averaging exponent, had to be determined from the simulation results.

Davies and Handschy²⁰ state another common mechanism controlling fault seals in unlithified sediments to be the juxtaposition of reservoir against non-reservoir lithologies. This approach works well where faults are single surfaces but can provide inaccurate results in the case when faults have multiple segments.²¹ In such cases, juxtaposition maps do not have practical meaning when the same lithology and petrophysical characteristics are in contact due to low scale faulting, constant lithology, and cases of net strike slip displacement.

Many investigators have focused their research on the understanding of fault rocks (shear zones) and their petrophysical properties. Jourde *et al.*²² studied the permeability anisotropy at large-scale using laboratory measurements for each fault element in the porous sandstone sequence in the Valley of Fire State Park in Nevada. In their model, they assumed permeability values for joints, sheared joint/deformation bands, slip surfaces, fault rock, and host rock of 10^6 , 0.1, 10^6 , 0.1, and 200 md respectively for a series of detailed maps based on outcrop cartography (**Fig. 1.2**).²² Using flow simulation, they found consistently high fault-parallel permeability (between 5.05 and 7.95 times the assumed average host rock permeability), due to the general N-S distribution of joints and slip surfaces contrasting with lower permeability values found for the cross-fault estimates (a decrease of 4.5 to 285 times the host rock permeability).

From these maps and subsequent permeability calculations, we can observe the impact and significance of permeability according to the area where this property is estimated.

Two main key scale factors arise when using this kind of approach (i.e. ref. 20). The first is related to overall scale of evaluation. Discrete values of calculated permeability will depend on the area considered. For example, Jourde *et al.*²² compare permeabilities for areas of different size, avoiding direct comparison of the representative values for each input map or understanding the effects of specific rock types, deformation elements or joints (**Figs.1-2a, 1-2b, and 1-2c**). First impression from output calculations makes believe that faults effects in the highest displacement fault (**Fig.1-2c**) are creating lowest permeability in the across fault direction. Although this statement could be true, in this study the scale or area of evaluation is not the same for each fault region. If a detailed analysis is required in order to determine the degree of compartmentalization, mainly caused by the presence of the fault (shear) rock, a more systematic approach has to be taken. In other words, the internal structure and petrophysical properties of the shear zone have to be addressed to investigate the interblock connectivity and the variability of the fault rock. As demonstrated by Jourde *et al.*²⁰ the fault rock is clearly controlling the across fault permeability and important detailed should be focused to investigate its variability along the fault zone.

The second key factor that should be carefully considered will depend on *in situ* conditions, which is the presence of joints or slip surfaces that connect the blocks at each side of the fault rock region (**Fig. 1.2b**). In the Valley of Fire State Park example, the identification of these small conduits crossing the fault rock and joining the adjacent blocks created a flow path that substantially increased across-fault permeability.

As derived from Jourde's study and some additional investigations, the shear zone controls the flow across the fault plane, and special identification and modeling have to be done to characterize the elements causing variable transmissibility. In this way, researchers as Shipton *et al.*²³, Antonellini and Aydin²⁴, Ibanez²⁵, and Wilson²⁶ have investigated the petrophysical properties of deformation bands as the primary control of total shear zone permeability.

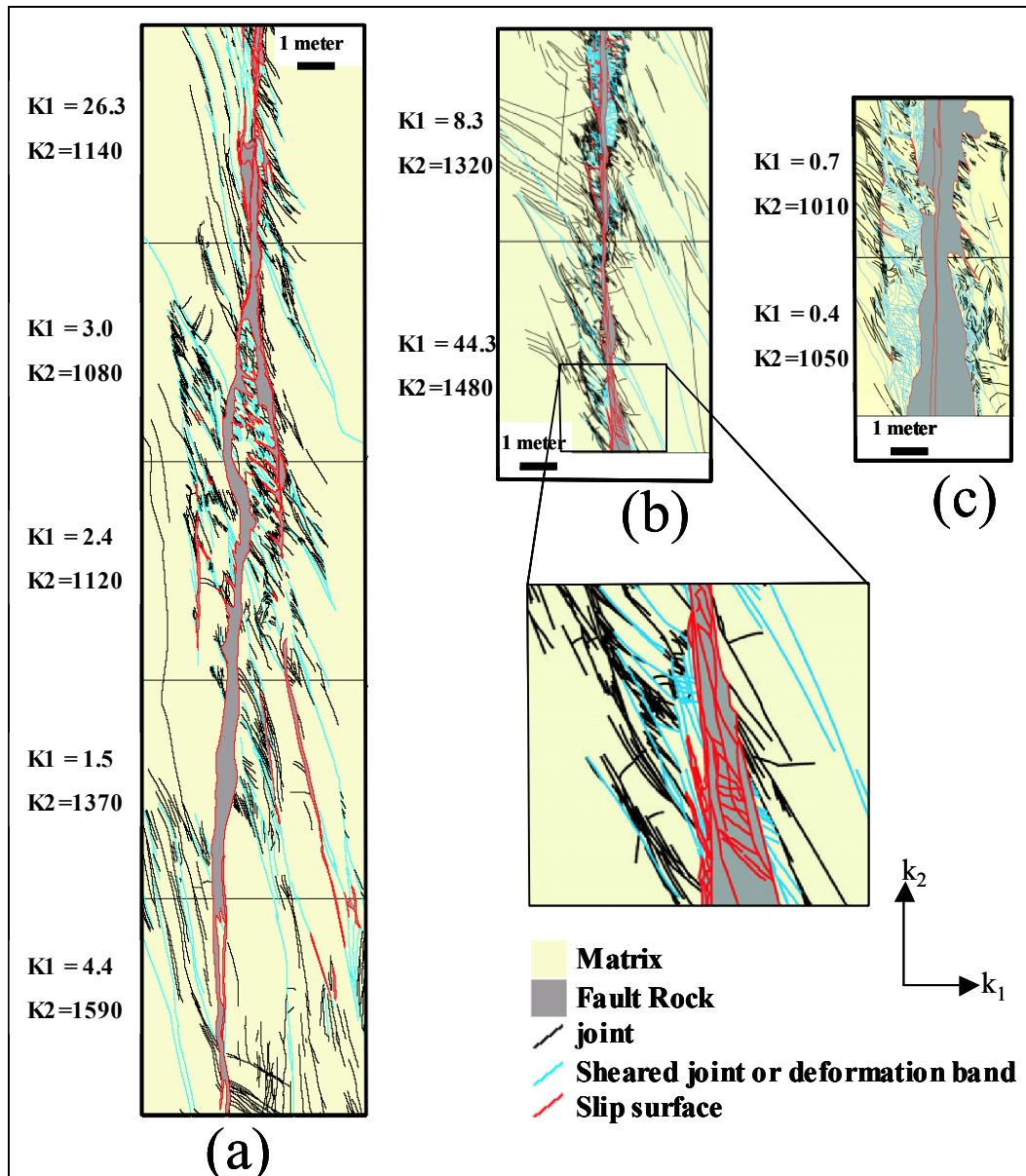


Fig. 1.2 – Permeability estimates for different strike-slip fault regions in the Valley of Fire State Park, Nevada. (a) a strike-slip fault with 6 m of slip, (b) a strike-slip fault with 14 m of slip, and (c) a strike-slip fault with 150 m of slip. k_1 and k_2 are the computed across and along permeability in md for the area of analysis. (Modified from Jourde *et al.* 2002)²²

Other important characteristics that should be evaluated for the determination of the flow character of shear zones are the thickness of the deformed zone and the continuity of internal deformation elements or facies. In many studies, a general relationship has been defined to predict thickness of the shear zone according to displacement,²⁵⁻²⁶ but thickness can vary by over two orders of magnitude. Nevertheless, all predictors represent statistically similar relationships.²⁶ For the particular area of the Hickory Sandstone Member in the Mason County, Ibanez¹⁹ and Wilson²⁰ investigated this relationship and the evolution of the main fault, being the main source for the present research addressing the internal architecture and the effects of deformation elements in fluid flow performance and prediction.

Ibañez study was focused in the understanding of how shear-zones evolve with increasing displacement and the effect of this evolution on fluid flow characteristics. In this way, Ibañez studied the geometry and permeability structure of a characteristic normal, dip-slip dominant, fault zone, finding useful relationships between the analyzed structure, the stratigraphic throw of the fault, the lithology, and permeability. Methods used for this effective shear zone characterization included surface mapping of texture, composition, and geometric characteristics of deformation elements, incorporation of mineralogic analysis of clay-rich intervals using standard x-ray diffraction techniques, and permeability measurements using steady-state probe and Hassler-sleeve permeameters.

Wilson's research was concentrated in the recognition of a high resolution structural and stratigraphic framework of this faulted reservoir volume in the Hickory Sandstone member, investigating fault structure and its evolution, and refining previously defined depositional models. All these studies have shown the importance of a detailed shear zone characterization to understand the mechanisms controlling shear zone development and the internal architecture and continuity of detailed features within the shear zone.

Although the continuity of particular elements is always an important issue of debate, the incorporation of a data set, as available for this project, allows us to consider

the spatial framework of shear zones with the analysis of subsurface unaltered samples at diverse fault locations.

We concentrated this study on the determination and integration of deformation elements, petrophysical properties and geometric attributes of shear zones in detailed three-dimensional models to analyze common and predictable effects in fluid flow and solve for best approximations to be used in upscaled geological models. This study integrated detailed petrological and sedimentary description of deformation elements from continuous core samples of shear zones in the Hickory Sandstone Member with permeability measurements obtained with an unsteady-state permeameter and a density framework from tomography scanning. This integration gives us an understanding of the mechanical processes affecting the rock during a diverse magnitude of faulting independently of the incorporation of shaly material within the shear zone.

From this and previous studies, we have found that highly deformed elements in the shear zone represent the greatest degree of distributed deformation where matrix material is mainly composed of sheared, fractured, and rotated sand grains. Permeability in these bands may be as much as two orders of magnitude smaller than protolith permeability, although the effect on density (porosity) is not as great.

The direct relationship between fault throw and the continuity and characteristics of deformation layers within the shear zone suggest that we can integrate this information in numerical simulation grids to match dynamic data of the field and analyze flow behavior across and along specific faulted zones in the reservoir.

Low-displacement faults create more discontinuous, deformed elements where the flow can travel randomly. High-displacement faults tend to form more continuous and layered flow units where the flow could occur longitudinally. Depending upon the permeability distribution, enough pressure drop could occur through cross-fault flow to break the minimum permeability restriction, changing the sealing character as a function of time.

When no 3D geological models are available, harmonic and arithmetic average permeability upscalers, depending of direction and thickness of deformation elements,

have demonstrated to be the best technique to match whole core permeability measurements in the shear zone, reproducing typical anisotropy seen in small scale and understanding general flow patterns. When detailed geocellular models have been built, full tensor permeability upscalers solving Darcy's flow equation are the most precise and sophisticated techniques to reproduce permeability anisotropy. Building such models will help us understand the effect of small/tiny deformation elements in overall shear zone permeability and how to account for those in certain conditions where dynamic and fluid conditions create possible compartmentalization.

This work did not pretend to solve the high complexity and uncertainty in determining deformation element continuity and properties, but it is a step forward to understand the importance of the internal architecture of shear zones, the characteristics of individual elements and their correlation with tectonic and geological variables. It also presents a systematic approach to predict shear zone permeability and thickness, information that should be integrated in static and dynamic models to account for drainage anomalies and the presence of reservoir compartments.

CHAPTER II

HICKORY SHEAR ZONES AND DEFORMATION ELEMENTS

2.1 Shear Zones in Hickory Sandstone Member

Fault zones cored from the Nickie Noble Ranch in the Hickory sandstone outcrop belt, northeast of Katemcy, Mason county in the central Texas hill country, were the source of samples in this study for the characterization of shear zones in sand-shale stratigraphic sequences (**Fig. 2.1a**).

The cores form part of a major drilling program that was initiated in 1996 to collect data from selected shear zones of a fault that has been evaluated by prior geologic and hydrogeologic fieldwork.²⁷ Nearly 3500 feet of rock sample, from eleven 2.4 inch-diameter cores, were obtained to sample the Hickory sandstone member and interpret the local stratigraphy and characterize the shear zone and fault structure (**Fig. 2.1b**).

Wells NNR-1 and NNR-2 penetrated the fault zone above the saturated interval and finished 10-20' after crossing the fault.²⁶ Wells NNR-3 through NNR-10 contacted the fault below the saturated zone, while the wellbore GKR-5 is merely contacting the footwall without hitting the fault zone.

The Hickory sandstone member of the Riley formation consists of three subunits (**Fig. 2.2**): the lower Hickory, about 185 ft thick, composed of yellow-brown, medium- to coarse-grained, poorly sorted, friable- to weakly-cemented, non fossiliferous quartzose, subarkosic and arkosic sandstone with some thin discontinuous mudstone intervals. The middle Hickory, approximately 200 ft thick, is composed of red-yellow-white-green, fine-grained sandstones and numerous clay-rich beds. The upper Hickory, between 50 and 75 ft thick, consists of red-maroon, coarse-grained, well-rounded, moderately sorted, fossiliferous, quartz sandstones with iron oxide-oids and calcite cement.

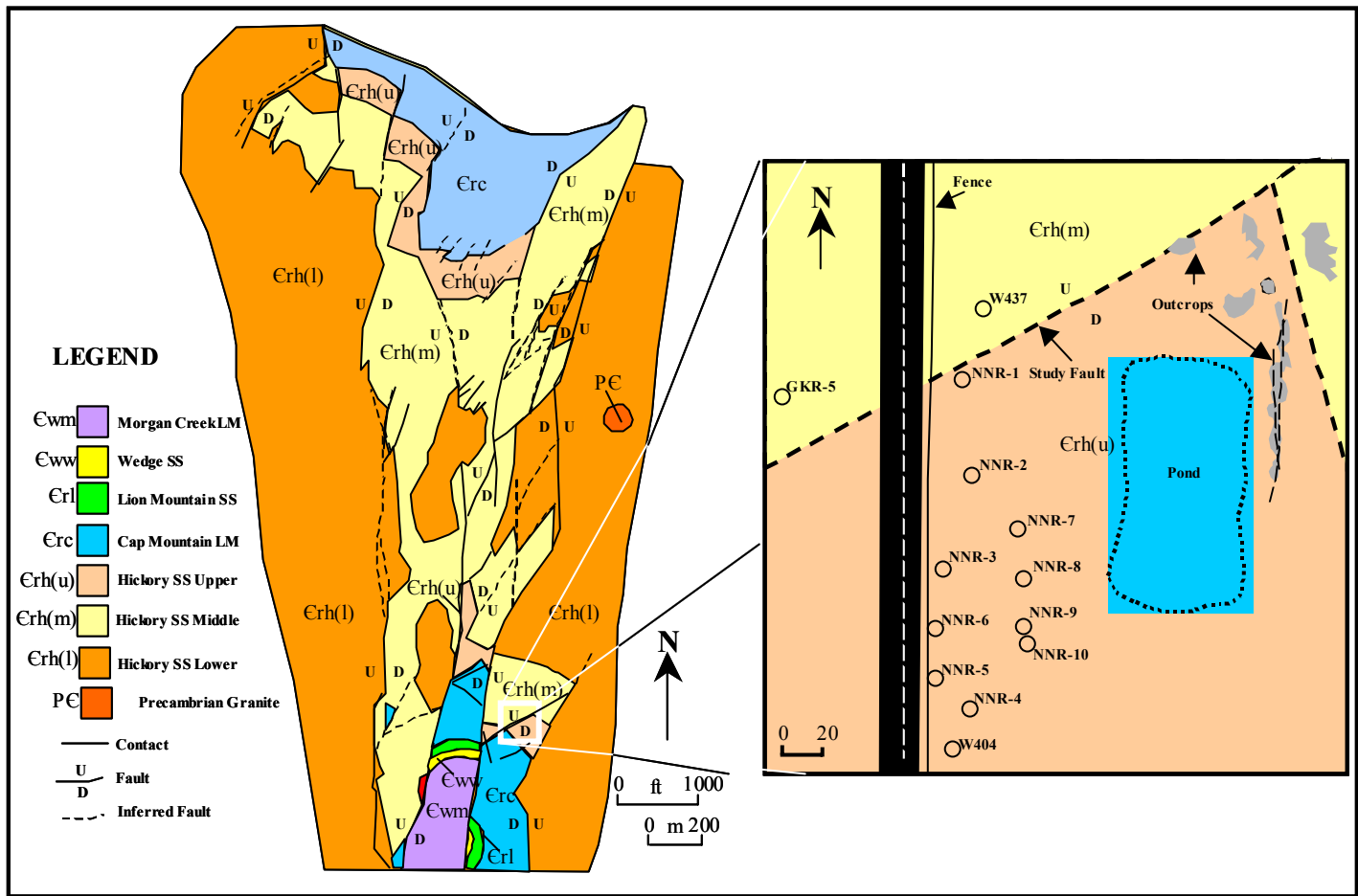


Fig. 2.1 – Regional geologic map and specific area of study. (Adapted from Wilson, 2001²⁶)

Wilson²⁶ identified cross-bedded facies as a main constituent in the lower Hickory. The typical sequence has 2 to 4 large-scale bed sets overlain by 5 to 10 moderately sorted, small-scale cross-bed sets overlain in turn by a massively bedded or small scale cross-bedded arkosic sandstones²⁶ (Fig. 2.2).

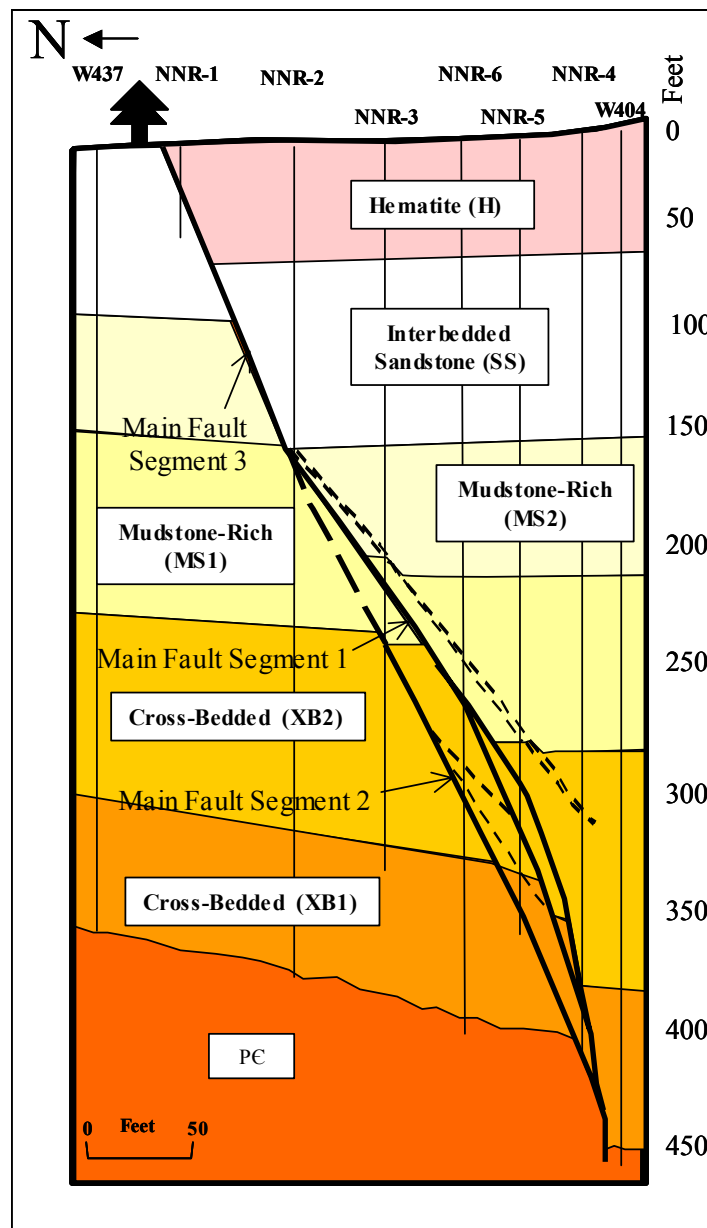


Fig. 2.2 – Cross section with general facies description by Wilson, 2001.²⁶

Differences between cross bedded facies XB1 and XB2 are the lower sorting, thinner large-scale cross beds, and the greater abundance of very coarse, chaotic strata elements in subfacies XB2. Additionally, XB2 subfacies exhibits greater abundance of mudstone with low degree of bioturbation (**Fig. 2.2**).

The Middle Hickory is composed of interbedded sandstone facies (SS) and mudstone-rich facies (MS) (**Fig. 2.2**). The Lower Middle Hickory is associated with mudstone-rich facies composed primarily of 5 cm to meter thick packages of mudstone and arkosic sandstone elements. Intense bioturbation is a common characteristic present that destroys primary sedimentary structures. Subfacies MS1 and MS2 have been differentiated according to color, thickness and relative abundance.²⁶

The Upper Middle Hickory comprises interbedded sandstone facies (SS). Lower to Upper Middle contact is transitional and it is distinguished by a change in sandstone color (buff to reddish-maroon) and by overall increase in grain size of the sandstones. SS facies are generally coarse to very coarse grain, fossiliferous with large-scale cross bed sets. Up in the section this facies becomes brown to greenish-brown. Hematite cement and hematite coated quartz grains are commonly found in the upper part of this facies.

Environmentally, the lower Hickory was deposited under braided-stream processes grading into marginal marine in the middle and upper Hickory. Ibañez²⁵ studied and characterized 29 out of 35 recovered shear zones in a relatively unaltered state and Wilson²⁶ developed a high-resolution stratigraphic and structural model from the area, studies that are the starting point for this project.

Wilson²⁶ described the overall fault zone geometry to be composed of a main fault, an upper fault and some additional small faults structurally above and below the main feature (**Fig. 2.3**). The main fault consists of three segments (segment 1, segment 2, and segment 3). Segment 1 and 2 overlap and form the main fault structure where they cut the Lower and the Lower-Middle Hickory sandstone unit. The segment 3 (**Fig. 2.2**) corresponds to the major segment that cuts the Upper Middle and Upper Hickory.²⁶ The

maximum stratigraphic throw for this fault is 17.5 meters (60 feet), found in the NNR4_404 shear zone interval.

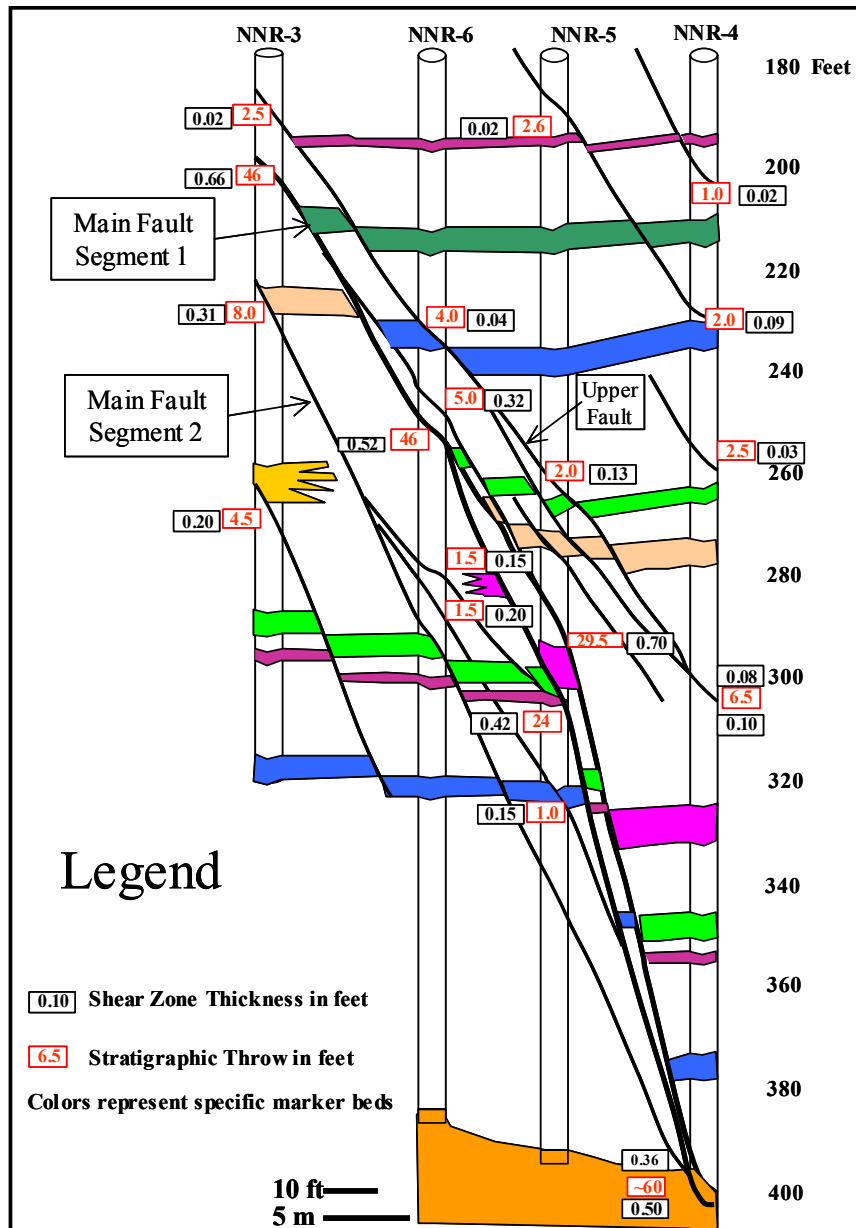


Fig. 2.3 – Western cross section through wells NNR3, NNR6, NNR5, and NNR4 showing the detailed stratigraphy and structural interpretation updated by Wilson.²⁶

According to fault striae in clay-rich slip surfaces, pitch is about 70° Northeast indicating a left-lateral strike slip component for the fault. In general for the area, striae show oblique, normal, dip-slip dominant displacement.²⁶

Four fault shear zones (NNR4_404, NNR5_291, NNR4_300 and NNR3_269) from the lower Hickory sandstone represent the input data for the present characterization (**Fig. 2.3**). Two samples, NNR4 at depth 404 ft, and NNR5 at depth 291 ft, correspond to high-throw shear zones. Attributes from the fault in NNR4_404 are N73E strike, dip of 75° SE, 0.853 feet of shear zone thickness, and 60 ft of calculated throw.²⁶ NNR5_291 shear zone has a fault strike of N27E, dip of 60° SE, 0.696 ft shear zone thickness, and 29.5 ft of calculated throw.

The NNR4_404 core, the highest fault throw sample, corresponds to the upper most section of the shear zone (**Fig. 2.4a**). The second high throw sample comes from the upper most part of the shear zone at NNR5_291 (**Fig. 2.4b**). This core sample is comprised of more than 63% of relative undeformed or protolith.

Although none of these two former samples recorded the total shear zone, they are key samples for the understanding of anisotropy and geometry of deformation at high displacement faulting and evaluate the impact of specific elements in the overall structure.

Ibañez²⁵ reported 13 and 10 percent of clay content in the shear zone for intervals at NNR4_404 and NNR5_291 respectively. Samples for this research missed the main shaly portion and just a small percentage (~5.6%) is included in the chosen interval for NNR4_404.

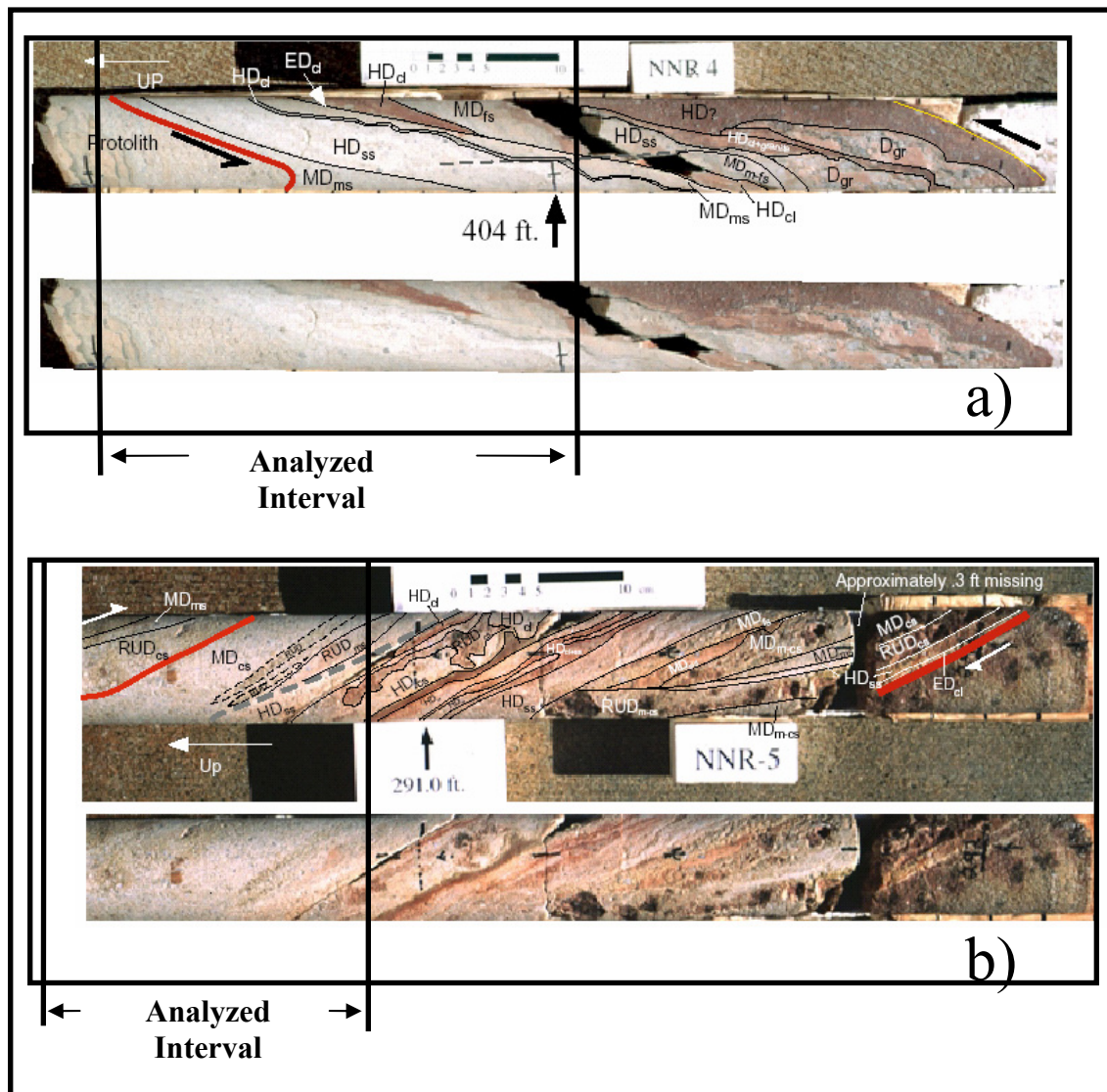


Fig. 2.4 – Selected high-fault throw samples. a) NNR4_404 b) NNR5_291. Upper picture shows interpreted deformation elements (section 2.2), the extension of the shear zone, and relative movement. Adapted from Ibañez.²⁵

The low-throw shear zones are represented by core NNR4 at 300 ft, fault strike of N65-57E, 67° SE dip, 0.184 ft thick and 6.5 ft of calculated throw, and core NNR3 at

269 ft has a fault strike of N53E, 69° SE of dip, 0.2 ft thick and 4.5 ft of calculated throw.²⁰ Sample at NNR4_300 represents the half upper part of total shear zone at this location and is part of the upper fault feature described by Wilson (**Fig. 2.3**).²⁶ Clay content in this shear zone is about 3% (**Fig. 2.5a**).²⁵

The lowest fault throw sample analyzed corresponds to the shear zone at NNR3_269, a small fault under the main fault plane, with local throw of 1.4 meters (4.5 feet). This core sample comprises more than 95% of the total shear zone for this particular location. Hence, further permeability estimations for this particular interval can be directly attributed to the inherent properties of the shear zone. Although this sample does not represent the main structural feature under investigation in the study area, its analysis can determine a good example of anisotropy of shear zones in the area. **Fig. 2.5b** shows the physical location of the modeled, simulated and measured sample according to the stratigraphic record for NNR3.

2.2 Deformation Elements in the Shear Zone

According to Chester and Logan²⁸ and Evans *et al.*,²⁹ shear zones are the points of fault zones where most displacement is accommodated and consist of zones of intense deformation of a finite thickness. Shear zones are identified by mesoscopic features such as the presence of a layered structure with orientations different from normal bedding, an abrupt termination of normal bedding against a zone of deformed material, an abrupt decrease in grain size relative to the adjacent protolith, a color change compared to typical undeformed sandstone, and distinctive pore size and porosity reduction.

Ibañez²⁵ subdivided deformation elements into three categories according to degree of distributed deformation. In his study, a map showing the distribution of each element in the shear zone was done with the integration of a subscript indicating the inferred protolith lithology. This information was the basic input in the present approach for the determination of spatial correlations and dynamic properties of selected fault zones.

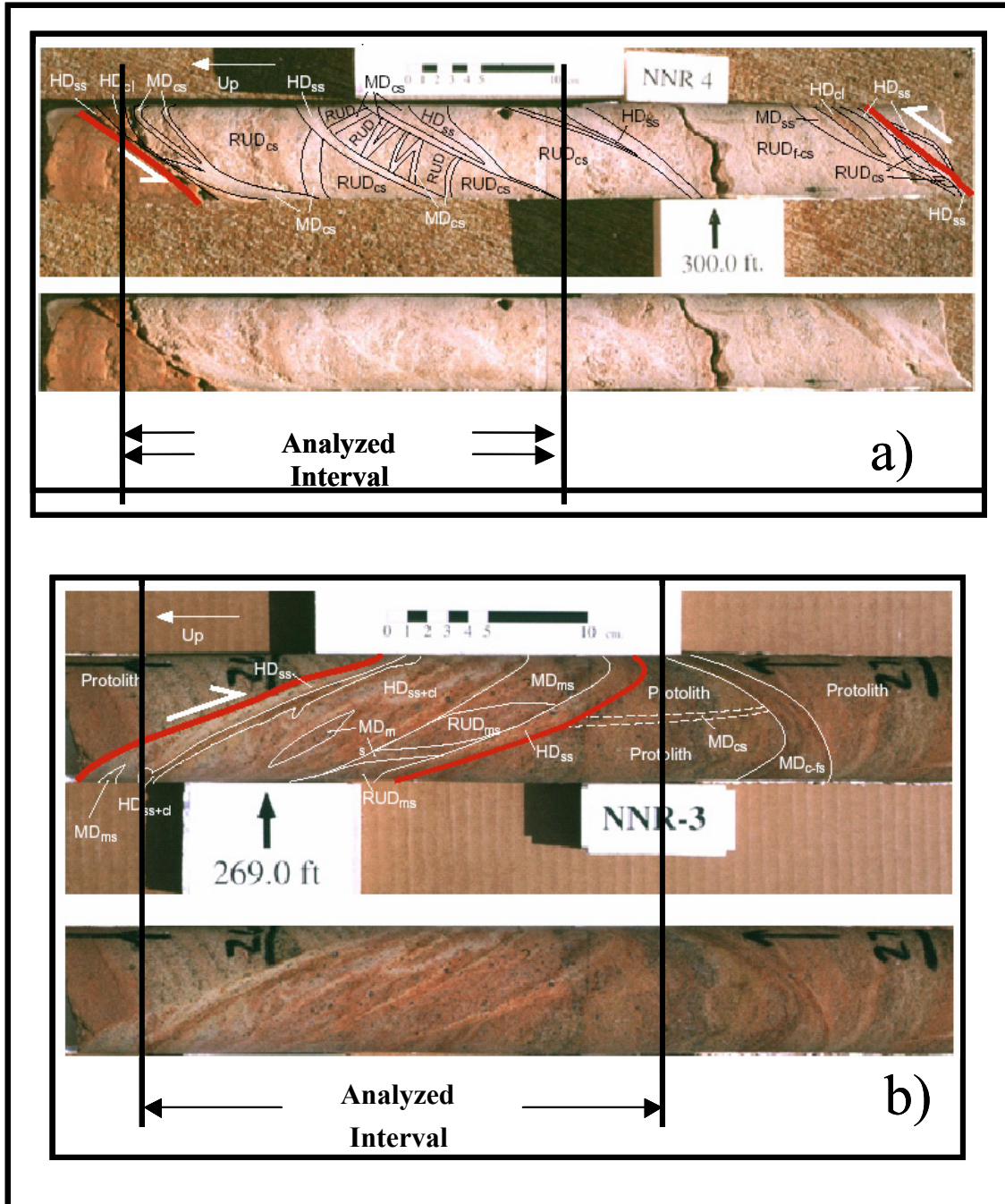


Fig. 2.5 – Selected low-fault throw samples. a) NNR4_300 b) NNR3_269.

Highly deformed sandstone elements (HDss) represent regions (bands) with the greatest degree of deformation. Generally, they are lighter in color than other structural elements and also their inferred protolith. Microscopically this element is composed of a large fraction (more than 75%) of sheared, fractured, and rotated grains of quartz and feldspars (**Fig. 2.6**). Comparative SEM micrographs and mesoscopic texture for each deformation element in NNR3_231 shear zone are shown at bottom of **Fig. 2.6**. Micro images clearly discriminate the highly deformed elements by a major increment in the content of clay-sized grains and low sorting compared with moderate and relative undeformed elements. Most highly deformed elements (83%) in sandstone lithology are continuous throughout the width of the core.²⁵

Moderate deformed elements (MD) are identified mesoscopically by the presence of deformed material but with a lesser degree of deformation than highly deformed elements. They have a broad range of grain-size distribution where silt-to-clay-sized fraction of grains represents between 5 and 75% of the total element.²⁵ Microscopically moderate deformed elements are distinguished from highly deformed elements by the wide range of grain sizes and the presence of fractured feldspar grains (SEM micrographs, **Fig. 2.6**). Forty-three percent of the moderate deformed elements terminate within the width of the core, being less uniform in thickness and continuity than the highly deformed features.

Relative undeformed elements (RUD) represent features with minor or no deformation, looking macroscopically like protolith. They occur in the shear zone as elongated or lenticular pods, where just 36% of the RUD elements are continuous throughout the core.

Mudstone elements can experience high, moderate or low levels of deformation, but the distinction between HD and MD mudstones is not possible at the mesoscopic scale. RUD mudstone elements are distinguished by the presence of original layering. Microscopically, HD mudstones display a strong component of mixing and compaction where micas and clay minerals appear to be wrapped around the grains.²⁵

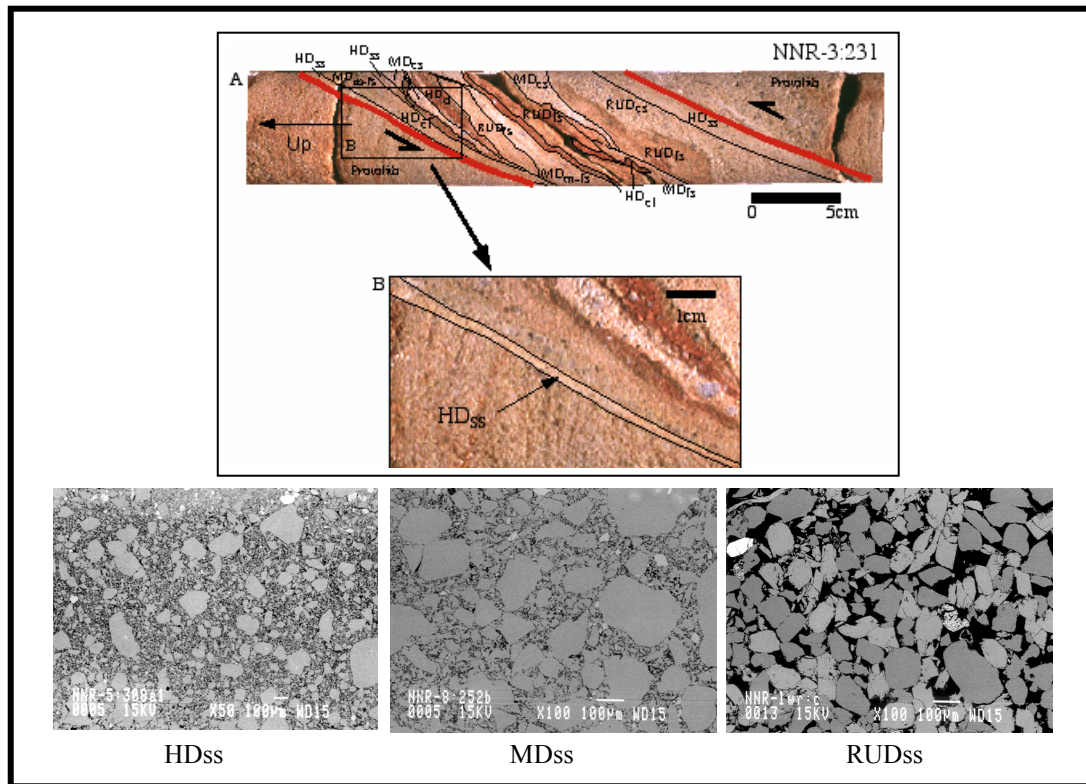


Fig. 2.6 – Comparative macro- and microscopic texture of highly deformed (HDss), moderate deformed (MDss), and relatively undeformed (RUDss) sandstones. Adapted from Ibañez²⁵.

CHAPTER III

SHEAR ZONE PERMEABILITY AND INTERNAL ARCHITECTURE

For the present study, measurements of permeability come from a probe permeameter based on a pressure-decay technique with useful range from 0.001 to 20,000 md³⁰ and from steady state air hassler permeameter for full-core and selected plugs samples. The analysis of three-dimensional architecture is derived from core surface mapping of facies and tomography scanning of each core, producing sequential cross-sectional slices that can be reconstructed for three-dimensional analysis³¹.

It is important to notice that when trying to model the shear zones and correlate results of numerical simulation with whole-core permeability measurements, a common inconvenient is the fact that shear zones get broken easily during coring avoiding to have a complete and continuous record of the shear zone, specially in the high throw, thick shear zone intervals. This problem reduces the chance of getting whole-core permeability measurements for the total shear zone extension. Three of the four analyzed core intervals represent partial shear zones and their analysis will be focused in the effects of individual deformation elements and no estimation of shear zone permeability (as independent unit) will be performed. In the other hand, core NNR3_269 shows a complete shear zone sequence and diverse solutions (analytical and numerical simulation) can be also used for the determination of the independent shear zone.

3.1 Probe Permeameter Data Acquisition

For the first step in the this project, four oriented (90°) sections of 6 mm-spaced probe permeameter measurements were taken from the surface of each shear zone core (pages 30, 33, 36, and 37). The probe permeameter is generally a very practical tool that facilitates to take many high-resolution measurements of permeability from the surface of selected samples. The main advantages of the incorporation of such data are the non-destructive character and the consideration of small-scale features and their effects in the

overall permeability. Special care should be taken when including this kind of source because some data anomalies can be generated by surface roughness, tip seal failure, cracks and diskings produced by mechanical reasons and decompression.

Conventional probe tools used to measure permeability consists of a gas-flow (nitrogen) measuring system that delivers gas at constant, measured pressure, using a probe tip and its flow rate is measured. At the same time, the gas flow rate is controlled by a mass-flow-controller and its delivered pressure is monitored. In this way, steady-state is achieved when pressure and flow rate become invariant with time. The major inconvenience in such a method is the large amount of time waiting until reaching steady-state conditions and the resolution achieved when dealing with low permeability samples.

Considering that shear zones are composed by low permeability material, this research considered the use of a pressure-decay permeameter³⁰ that obtains permeability values in a faster manner and with a substantially greater resolution in the range between 0.001 md and 20 darcys. This apparatus consists of a tank of internal volume that is filled with nitrogen to a desired fill pressure, and then the fill-valve is closed. After sealing the probe tip against the sample surface, a lower valve is opened allowing and the pressure in the tank is recorded as a function of time. Quantitatively, the slope of the pressure-decay curve (at any time after an initiation period, during which a smooth pressure gradient is established in the sample) yields an instantaneous flow-rate function.

Including geometrical factors calculated by Goggin *et al.* (in ref. 30) to account for the ratio of the outer-to-inner seal radius (for samples large enough to avoid that boundaries affect the measurements) and Klinkenberg's relationship to account for the gas slip factor, the equation that yields the slip-corrected permeability is given by,³⁰

$$K\alpha = \frac{29392\mu\gamma}{(G_o r_i)(p + 2Pa + 2b)} \quad (3.1)$$

where b is the Klinkenberg gas slip factor (psi) for the nitrogen, P_a the actual ambient atmospheric pressure, p the value of the gauge pressure at the point where the slope is evaluated, μ is the viscosity and γ (from the slope of a semi-logarithmic plot of the pressure decay data) is defined as,³⁰

$$\gamma_n = \frac{V_T \ln\left(\frac{P_n - 1}{P_n}\right)}{t_n - t_{n-1}} \quad (3.2)$$

where V_T is the internal volume of the tank, and P_n the pressure at any point of time t_n .

Due to the fact that only one point is obtained that lies on the Darcy flow line when using this technique,³⁰ the Klinkenberg slip factor should be determined from correlation, otherwise an iterative process is executed using the equation,

$$b^* = 6.9K_a^{-0.382} \quad (3.3)$$

where b^* is denoted because b is coming from a correlation. The iterative process using equations 3.1 and 3.3 should be performed until the change in b^* is less than 0.1 psi.³⁰

The probe rubber tip that was used for all the samples has an outer diameter of 1.7 cm and an internal (effective for measurement) open diameter of 6mm. With such configuration, the 6 mm step guarantees 3 mm of overlap between continuous measurements. Although with the 4 oriented transects were expected to have enough areal sampling and adequate characterization of the permeability behavior of all the deformation elements, some focused stations were added when minimum requirements of confidence in data analysis was not reached (defined as minimum number of samples equals to $(4Cv)^2$). In this way, the minimum sampling guideline was set equals to 16 times the square of the coefficient of variation $(4Cv)^2$, where Cv is defined as follows:

$$Cv = \frac{Var(k)^{1/2}}{E(k)} \quad (3.4)$$

where $Var(k)^{1/2}$ is the standard deviation of permeability and $E(k)$ is the expected or mean value.

Considering at least a number of samples equals to $(4Cv)^2$ for each particular deformation element, we can characterize statistically 95% (up to two standard deviations) of the population with a 50% tolerance on the average.³²

During the process of data acquisition, an exhaustive probe calibration was performed with standardized plug samples before and after each job section to guarantee precision of measurements, and at least two stations in each transect were repeated for quality control and repeatability. Additionally, extremely high values and outliers were also repeated controlling very carefully the surface condition and seal integrity to ensure the reliability and validity of the output. All the output data were then carefully correlated with deformation element type and integrated with subsequent tomography scanning (step two of the current investigation).

This approach intended to compare individual deformation values in each shear zone instead of considering averaging individual deformation element properties for all the zones. In this way, prediction of relative degree of smearing, and/or cataclasis and resulting petrophysical characteristics were evaluated for specific protolith texture and composition.

The general behavior of log-permeability shows a consistent decrease in flow potential with the increase in deformation (**Fig. 3.1**). Undeformed elements exhibit permeability values from 1 md to more than 5 darcies while moderate degree of deformation generates up to one order of magnitude decrease in permeability, with the lowest values at smaller grain size.

Highly deformed elements show a narrow range of variability in flow behavior with permeability ranging from 1 to 20 md (**Fig. 3-1** and Appendix 1). A clear decrease in the interquartile range is noticed for these facies, from 0.2073 to 0.8118 for the

logarithmic transformation of permeability in the analyzed samples. In general, the highly deformed clay material exhibits a median permeability of 0.061 md (-1.21 in the logarithmic domain) with a total range of 0.211 md.

Considering the ratio of log-permeability of each individual deformation element and the correspondent undeformed rock (**Fig. 3.2**), a systematic decrease in this relationship can be suggested with an increase in fault throw for the highly deformed sandstone elements. This observation will be complemented later with the incorporation of additional shear zone permeability measurements available from external sources. Unfortunately, this trend in permeability degeneration with fault movements is not clearly visualized for the moderate deformed facies (deformation elements 1 through 3) being their flow behavior more erratic and unpredictable.

From the analysis of high-throw shear zones available (NNR4_404 and NNR5_291), a decrease of 23 to 38 times (mean permeability) between RUD and protolith elements, and HD sandstone elements is present in the shear zone (**Table 3.1**). From the low-throw shear zones, the permeability ratio of RUD and HD sandstone elements varies between 10 and 13 times, suggesting a decrease in cataclasis and diagenetic effects consistent with the degree of displacement experienced.

These general statistics suggest that each shear zone and deformation element have to be evaluated separately and sampling should be quite effective to characterize each facies at particular locations. The following sections describe general statistics of the permeability field from probe permeameter for the selected shear zone samples; analysis that is also included in Appendix 1.

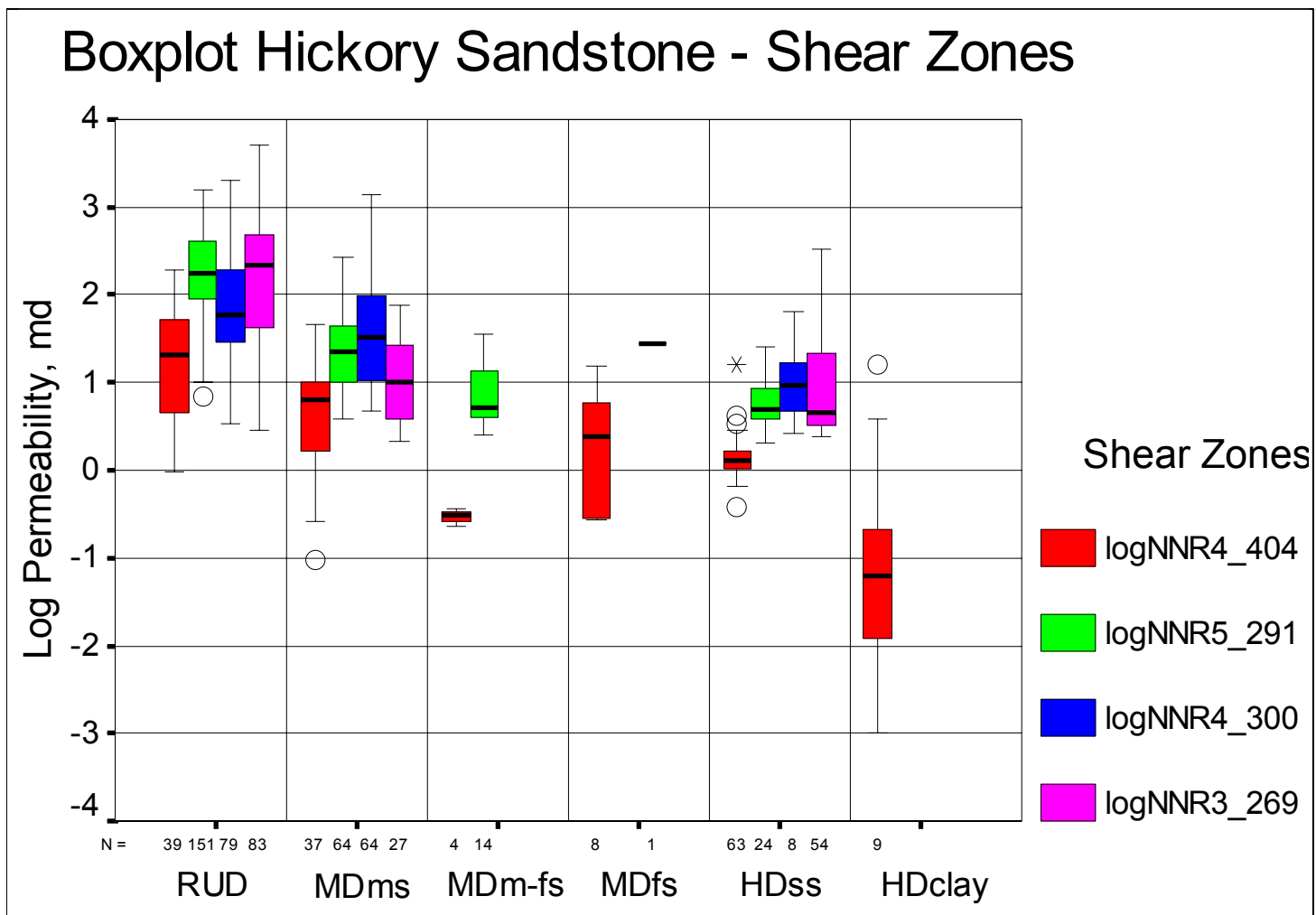


Fig. 3.1 – Boxplots of permeability by deformation elements.

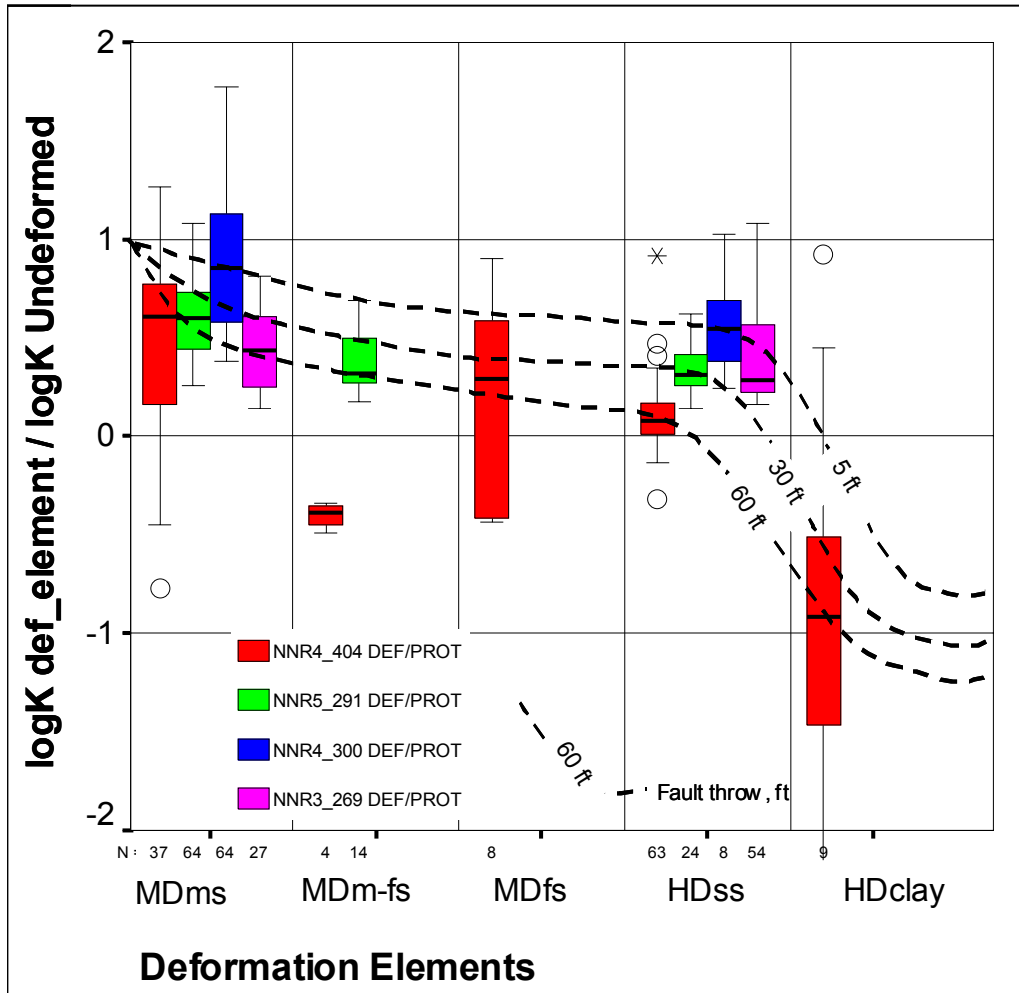


Fig. 3.2 – Boxplot of the ratio of logarithm of permeability between deformation elements and undeformed (host) rock.

3.1.1. NNR4_404 Shear Zone with 16.7 Meters of Throw

The protolith and relatively undeformed sandstone exhibit a mean permeability of 37.4 md with 48.38 md of standard deviation.

For the characterization of RUDss elements in sample NNR4_404, thirty-nine measurements were taken while $(4Cv)^2$ was 27 (**Fig. 3.1 and Fig. 3.3**). Moderate deformed elements represented by MDms, MDms-fs, and MDfs exhibited 8.96, 0.3 and 9.21 md of mean permeability with 10.74, 0.057, and 5.54 md of standard deviation respectively (**Appendix 1**).

Measurements originally taken for the four transects previously established were close to the limit of 50% tolerance at $(4Cv)^2$, for this reason, additional control points between main transects were added to better characterize the statistics of these elements. These moderate deformed elements exhibit a decrease in permeability of about 4 times compared to RUD and protolith rocks when dealing with moderate to good sorting (MDms and MDfs). Facies with low sorting (MDms-fs) showed a larger decrease in permeability, of about 100 times compared to the undeformed, host rock.

Highly deformed elements in this sample are represented by a very continuous band that extends through the whole core (**Fig. 3.3**), and form 39% of total elements (**Table 3.1**). This characteristic facies exhibits a very distinctive behavior with low variability, of the 63 analyzed measurements. The permeability of highly deformed elements in NNR4_404 is 23 times lower than host rock and structurally represents the control element (low permeability element) causing permeability anisotropy due to the high continuity parallel to the fault plane. These elements are playing big effect in across or perpendicular-to-fault-plane flow because more than 80% of them are continuous throughout the samples for all shear zones in the Hickory sandstone member.²⁵

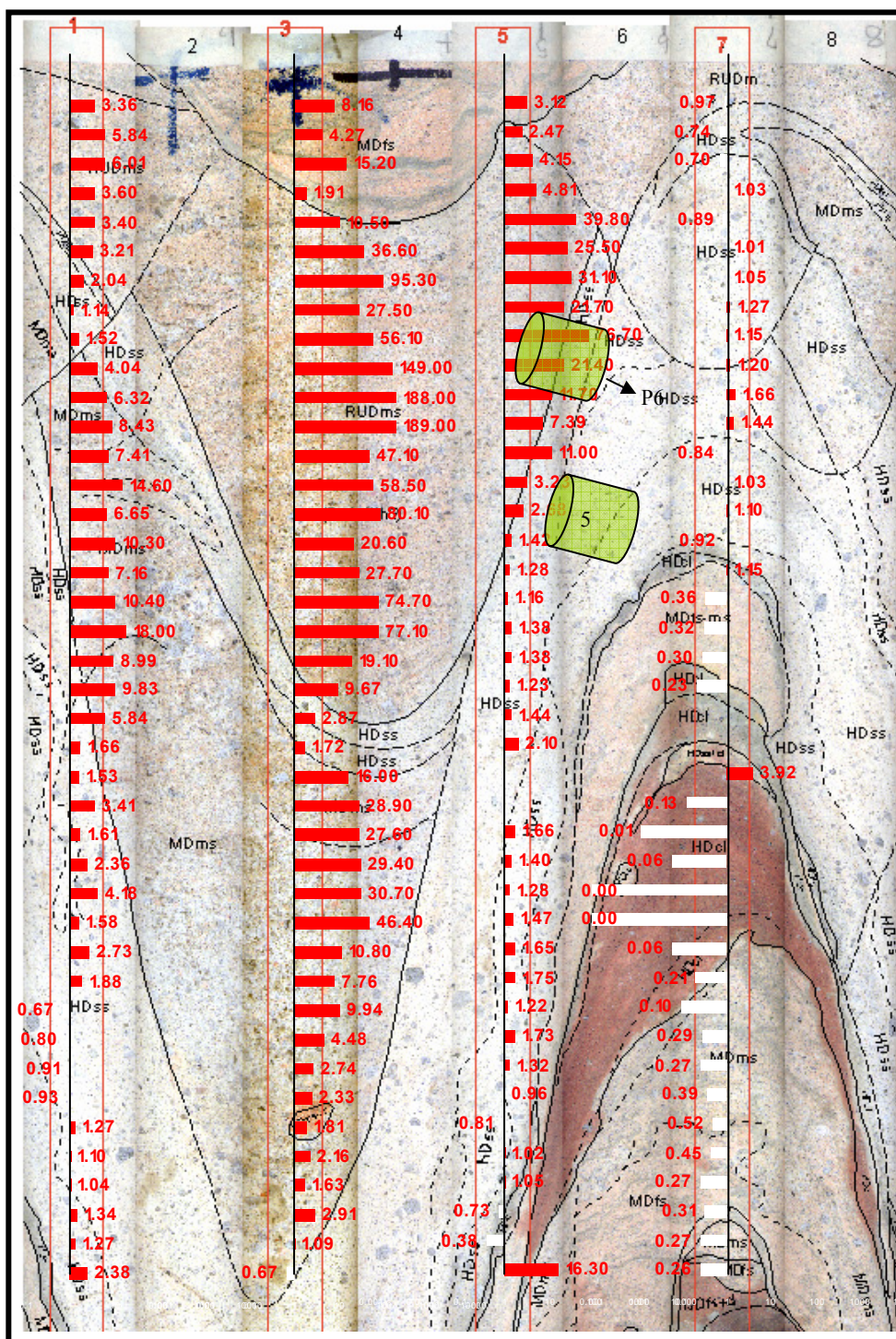


Fig. 3.3 – Surface map of core NNR4_404 with interpreted continuity of deformation elements and permeability transects from probe measurements. The permeability values are plotted using bars in logarithmic scale (values under 1 md correspond to white bars to the left). P5 and P6 correspond to plugs samples (Chapter IV)

Table 3.1 - Proportion, Mean and Median permeability values of deformation elements.

Shear Zone Throw (ft)	RUDcs			RUDm-cs			RUDms			MDcs			MDm-cs			MDms			MDms-fs			MDfs			HDss			HDcl			HDss+cl		
	P	Km	Kmd	P	Km	Kmd	P	Km	Kmd	P	Km	Kmd	P	Km	Kmd	P	Km	Kmd	P	Km	Kmd	P	Km	Kmd	P	Km	Kmd	P	Km	Kmd	P	Km	Kmd
NNR3_269 4.5							0.51	503.2	215							0.16	18.4	10.3							0.1	49.7	22.5				0.23	12.7	3.9
NNR4_300 6.5	0.16	951.7	157	0.13	120	55.1	0.25	63.1	34.2	0.06	53.6	24	0.10	190.5	62	0.24	81.8	26.1							0.05	16.9	9.3						
NNR5_291 29.5							0.64	281.7	180							0.27	37	22.8	0.06	9.4	5.3				0.03	7.3	5						
NNR4_404 60							0.24	37.4	20.6							0.23	9	6.3	0.03	0.3	0.3	0.05	0.4	0.3	0.39	1.6	1.3	0.06	0.1	0.1			

P: proportion of facies (%), RUDm-cs: Relatively Undeformed medium to coarse grain ss

MDms-fs: Moderate Deformed m-f ss, km: mean permeability, md

MDcs: Moderate Deformed coarse grain ss, MDfs: Moderate fine grain ss

Kmd: median permeability, md MDm-cs: Moderate Deformed medium to coarse grain ss, HDss: Highly Deformed ss

MDms: Moderate Deformed medium grain ss

HDcl: Highly Deformed clay, HDss+cl: Highly Deformed sandstone + clay

RUDcs: Relatively Undeformed coarse grain ss

The other low permeability facies, represented by the highly deformed clays, has an average permeability of 0.068 md and a standard deviation of 0.078 md. Although $(4Cv)^2$ for this element is 21 and our measurement density is substantially lower (7), no additional stations were measured to increase confidence in data analysis due to the lack of exposure at core surface. Nevertheless, range as low as 0.211 gives us the idea of the low permeability spectrum of this element. From the analysis of the entire shear zones,²⁵ clay facies continuity in cores is lower than the sandstone equivalents, suggesting that this lithology may be shorter in length. The stratigraphic thickness of this structural element in NNR4_404 is variable (from 2 mm up to 1.3 cm in the core sample) and represents a clear pinch out geometry of restricted continuity (**Fig. 2.4a**).

Although few available mudstones and clays are present and available for measurement in the chosen shear zones, probe permeabilities range from 0.001 (probe resolution) to 0.212 md. This is in contrast with a value of 0.0002 md for this facies suggested by Gibson.³³ Although Ibañez made a sensitivity analysis considering lower permeability values (as low as suggested by Gibson) founding an additional reduction in harmonic-average permeability (up to three orders of magnitude), this probe permeameter device and results suggest that the mean value of 0.068 md is quite reliable. This value compares in the middle range between the 0.6 md average in Ibañez analysis and 0.0002 md from Gibson approach. Obviously, the precision in determining permeability and especially in the lowest values will affect strongly the harmonic average. For this reason, shaly facies in shear zones should be also carefully characterized and, if necessary (when permeability reported equals to resolution limit), evaluate the effect in the average with values below the resolution of the device used. Further considerations about the effect of these particular elements will be discussed when detailed modeling and match with laboratory calculations are presented (Chapter 6).

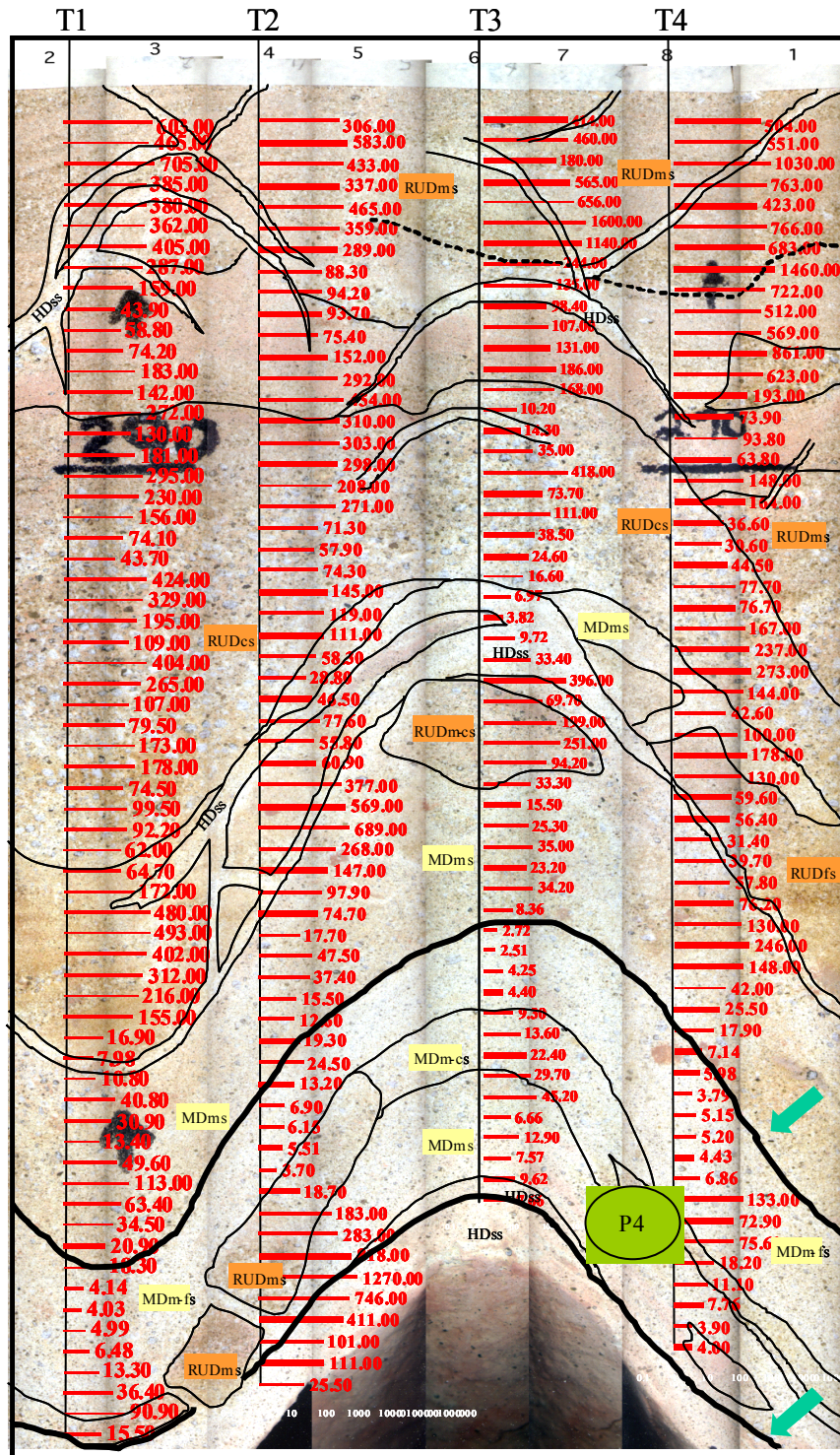


Fig. 3.4 – Surface map of core NNR5_291 with interpreted continuity of deformation elements and permeability transects from probe measurements. P4, plug analyzed. Greens arrows show key deformation element contacts and control surfaces.

3.1.2. NNR5_291 Shear Zone with 13.9 Meters of Throw

The second shear zone investigated with high throw, the NNR5_291, is composed by 64% of relatively undeformed elements with an average (mean) permeability of 281.7 md and a standard deviation of 278.8 (**Fig. 3.1 and Fig. 3.4**). Regardless of the high standard deviation exhibited, this facies was effectively tested by close to 10 times the $(4Cv)^2$ for the 95% confidence limit between two standard deviations (**Appendix 1**).

The moderate deformed elements represent 33% of total deformation facies for the core and reveal mean permeability values of 37 md in the medium grained sandstones and 9.4 md in the medium to fine grained sandstones. Standard deviation for these facies is in the order of 44.8 and 9.5 md respectively.

From surface mapping, the highly deformed elements have a complex framework composed by narrow bands more discontinuous upward in the sequence (for this particular sample) or at longer distance from shear zone mid point. These bands also have a tendency to exhibit a thinning upward structure constituting just the 3% of the total framework of the analyzed core and having 7.3 md of mean permeability with 5.6 md of standard deviation (**Fig. 3.4 , Appendix 1**). These elements show a reduction of permeability of about 38 times compared to host rock while moderate elements are between 8 and 30 times. This facies has been effectively measured with 24 samples under the prospected conditions equivalent to $(4Cv)^2$ that requires at least 9 stations for the proper statistical characterization.

3.1.3. NNR4_300 Shear Zone with 1.5 Meters of Throw

Sample NNR4_300 with a low throw of about 1.5 meters²⁶ is composed of a series of relatively undeformed elements (from RUDcs to RUDms) that account for 54% of the total framework in the core. The average permeability varies from 951.7 to 63.1 md with standard deviation from 610.4 to 69.6 md respectively (**Fig. 3.5, Appendix 1**).

Moderately deformed elements are represented by coarse, medium to coarse, and medium grain sandstones and have mean permeabilities of 53.6, 190.5, and 81.8 md

respectively. From this sample, this granulometric sequence does not show a consistent decrease in mean permeability as expected from general expectations according to grain size distribution. Possible reasons could be the moderate to high standard deviation observed in the undeformed rock, the difficulty in differentiating moderately deformed and undeformed facies and problems related to the areal resolution of the probe tip causing measurements in commingled facies.

The highly deformed elements represent 5% of the total facies evolution for this sample and show an average permeability of 16.9 md, about 10 times lower than the protolith rock. The standard deviation is 21 md and the continuity of such elements tend to be continuous throughout the core although with very low thickness (from 2 mm to 1 cm).

3.1.4. NNR3_269 Shear Zone with 0.5 Meters of Throw

Sample NNR3-269 representing the unique full shear zone, is composed by 51% of relatively undeformed elements and protolith, 16% of moderate deformed elements and 10% of highly deformed facies. The average protolith permeability is 503 md and standard deviation of 979.1 md (**Fig. 3.6, Appendix 1**). Such as high standard deviation compared to the mean, makes that more than 61 measurements had to be taken in order to characterize the statistics of these elements with 95% confidence (eighty three probe perm stations were measured in these facies).

Moderate deformed elements represented by moderate deformed medium sandstones have 18.4 md of average permeability (standard deviation of 18.6 md) 27 times lower than protolith while HDss elements have 49.7 md of mean permeability and 85.8 md of standard deviation. This average permeability corresponds to a 10 times reduction compared to host rock.

The mixed highly deformed lithology facies of sand and clay is also present with an average permeability of 12.7 md and 26.7 md of standard deviation, although the sampling rate does not allow having the desired confidence for the characterization of this particular deformation facies.

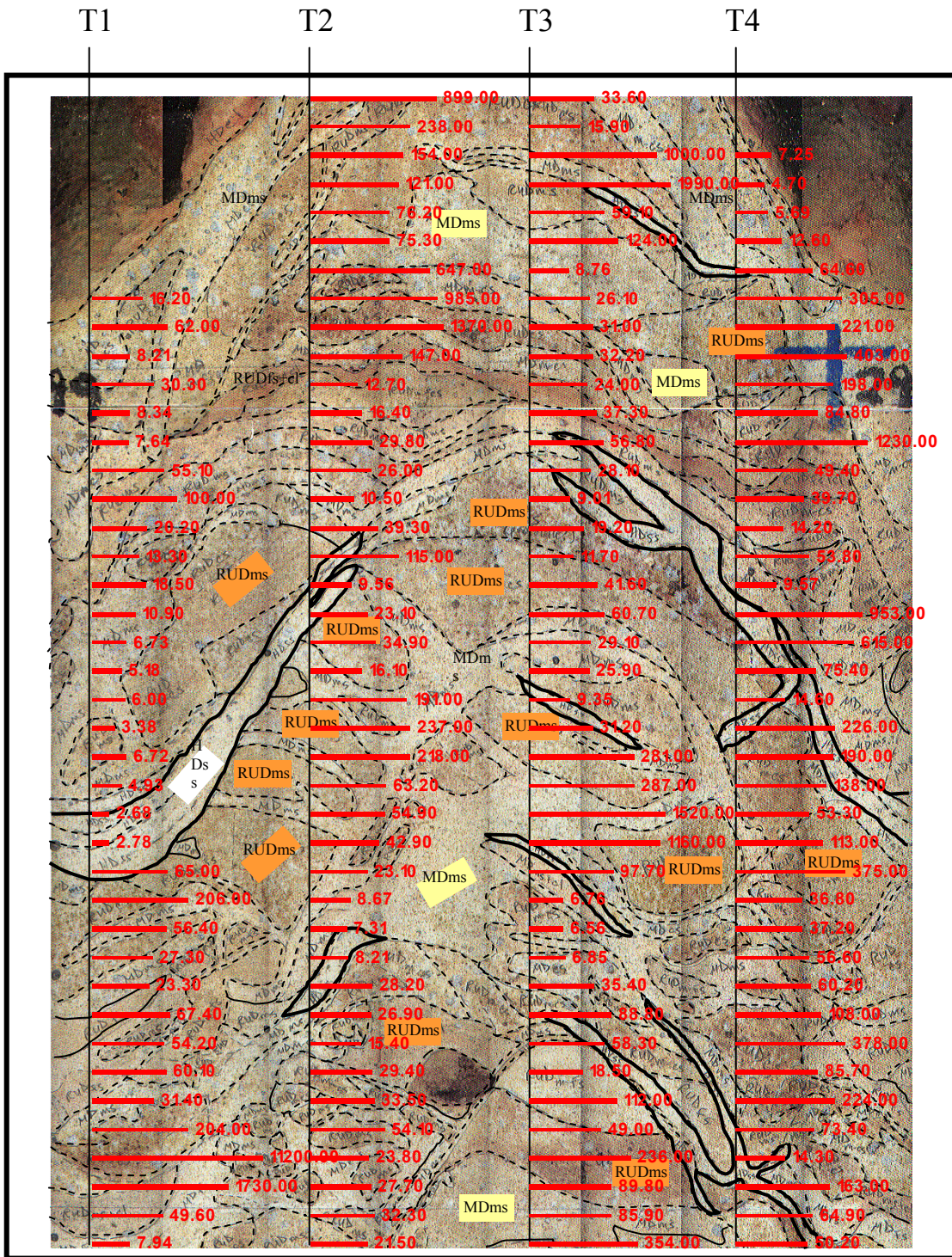


Fig. 3.5 – Surface map of core NNR4_300 with interpreted continuity of deformation elements and permeability transects from probe measurements

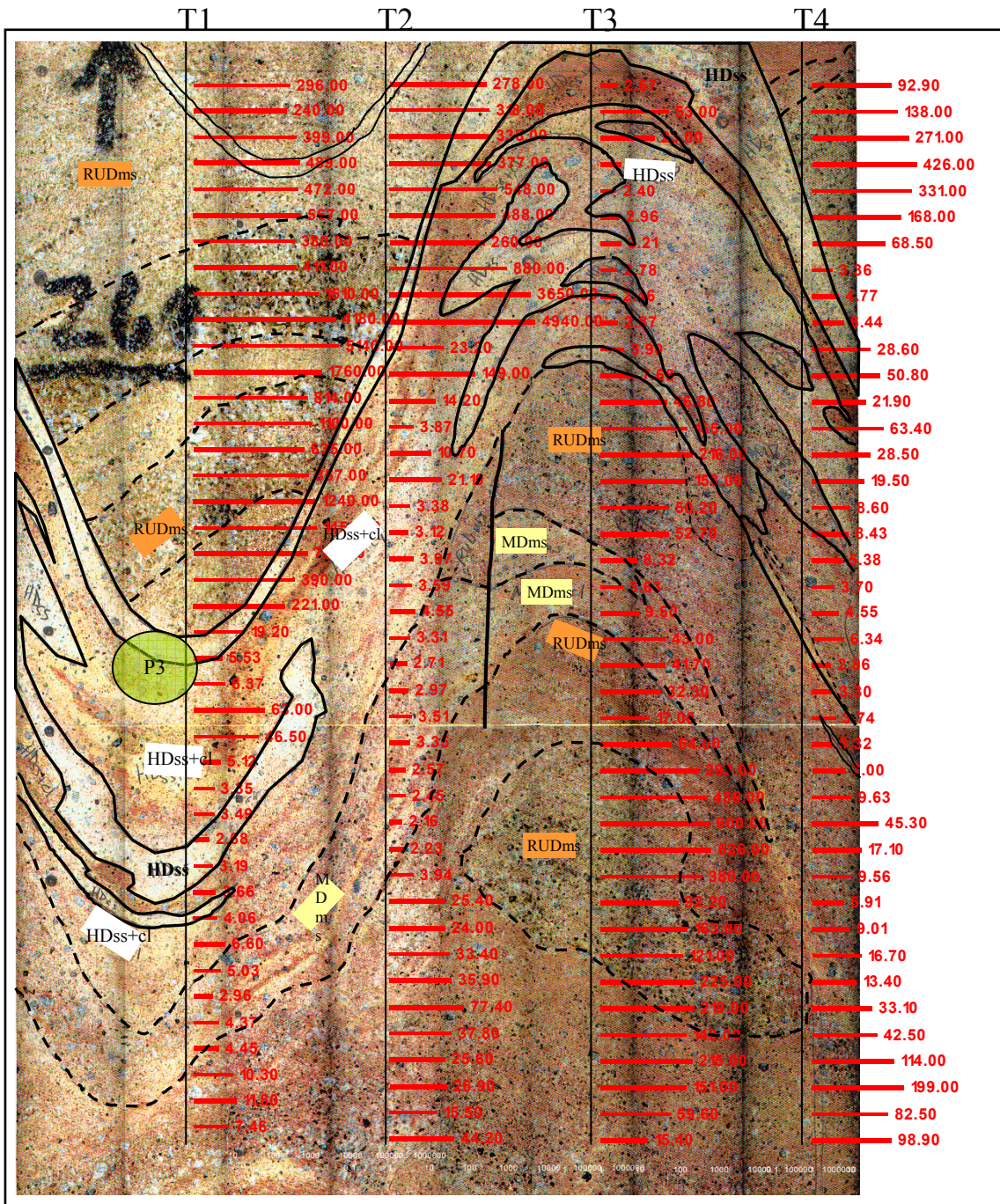


Fig. 3.6 – Surface map of core NNR3_269 with interpreted continuity of deformation elements and permeability transects from probe measurements.

3.1.5. Summary Comments

In general, a broad trend can be seen in the four selected intervals, with a decrease of the ratio of mean permeability between highly deformed elements and protolith with fault throw magnitude (**Fig. 3.2**). In other words, the reduction of permeability of the highly deformed elements seems to be dependent on the magnitude of movement experienced and obviously, depending of the quality of the original host rock involved in the deformation process. Further discussions and findings by diverse investigators^{25,34-36} have shown the additional control of throw and displacement to the thickness of gouge breccia and internal deformation elements. According to such investigations it is clear that the thickness of the shear zone plays a big role in fault conductance and the examination of field correlations with geological parameters should be a mandatory step to predict the flow potential and continuity of the shear zone.

3.2 Probe Permeameter Data Comparison with Ibañez²⁵

This research investigated high-resolution permeability anisotropy related to selected shear zones created by variable fault displacement in the Hickory sandstone member. A former study²⁵ considered all the available cores from shear zones in order to evaluate the mesoscopic and microscopic structure and identified the structural elements controlling the overall permeability.³⁷ The few points of comparison between Ibañez²⁵ probe measurements using a steady-state permeameter and those of this study show fair agreement (**Fig. 3.7**). A significant difference between this and Ibañez' study is caused by the low permeability resolution of the steady state permeameter used by Ibañez in the measurements of deformation elements in mudstones and some sandstones with high deformation (**Fig. 3.7**). Another source of disagreement is the fact that sampling locations are not identical and the high variability (anisotropy and heterogeneity) is inherent in the protolith and undeformed facies.

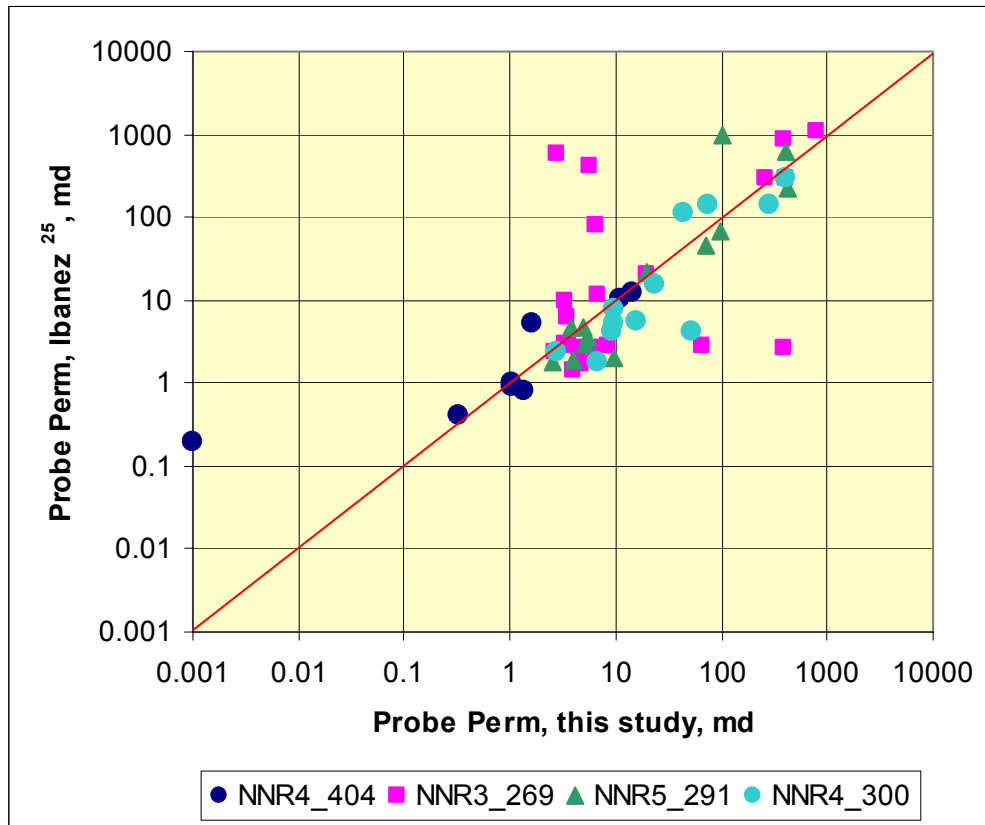


Fig. 3.7 – Correlation of probe permeameter data (point measurements) for samples at NNR4_404, NNR5_291, NNR4_300 and NNR3_269. Ibañez’s data²⁵ are from a steady-state permeameter, Nieto’s data from an unsteady-state permeameter

3.3 Permeability in the Shear Zone Versus Throw

Integration of our data with those from Ibañez has shown a systematic reduction of permeability of highly deformed elements with fault throw, as previously visualized and discussed with the selected core samples in Section 3.1 (**Fig. 3.8**). The plot of the average and geometric mean permeability of HDss elements versus fault throw for all the shear zones in the Hickory sandstone member shows a fair trend of overall reduction in permeability according to fault throw and the permeability of the protolith. Samples with no measurements at that particular facies were not included. For those cases when data were not obtained in those facies, Ibañez assigned a mean value of 1.9 md for HDss

elements. According to this plot (**Fig. 3.8**), we can see a high scatter in permeability values demonstrating the existing heterogeneity by element.

Deformation elements are facies with similar degree of cataclasis and not with similar permeability. For this reason, when trying to predict their flow characteristics, one should avoid averaging them for getting a representative permeability value for that particular element. For instance, for a zone with protolith permeability of around 30 md, highly deformed elements in a 60 feet throw fault will exhibit permeabilities around 1.6 md while in a 5 feet throw fault these facies could have around 9 md (from **Fig. 3.2**).

From this analysis, the effect of the host rock is clearly influencing HD permeability. Permeability versus fault displacement correlation (**Fig. 3.8**) demonstrates that faults with throw greater than 10 feet generate highly deformed elements with permeability less than 8 md and related to the host rock permeability. For the same fault throw, HD elements created from higher permeability host rock will exhibit better flow characteristics. For faults with throw less than 10 feet, the permeability of the HD elements is not predictable.

The same analysis can be executed for moderately deformed elements, although the degree of cataclasis is limited and variable that the correlation observed shows a general trend with large scatter.

3.4 The Analysis of Shear Zone Thickness and Deformation Element Thickness

An additional and import variable to predict the overall shear zone permeability is the thickness of total interval between slip surfaces, the internal architecture and distribution of deformation elements, and their own thickness. For this particular analysis, we have combined the shear zone geometry analysis by Ibañez²⁵ and the re-evaluation of fault characteristics by Wilson²⁶ with the detailed observations in the four high and low throw fault samples for the same area (**Table 3.2**). Surface maps (**Figs. 3.3 to 3.6**) were also incorporated in order to correlate permeability measurements with deformation element geometries.

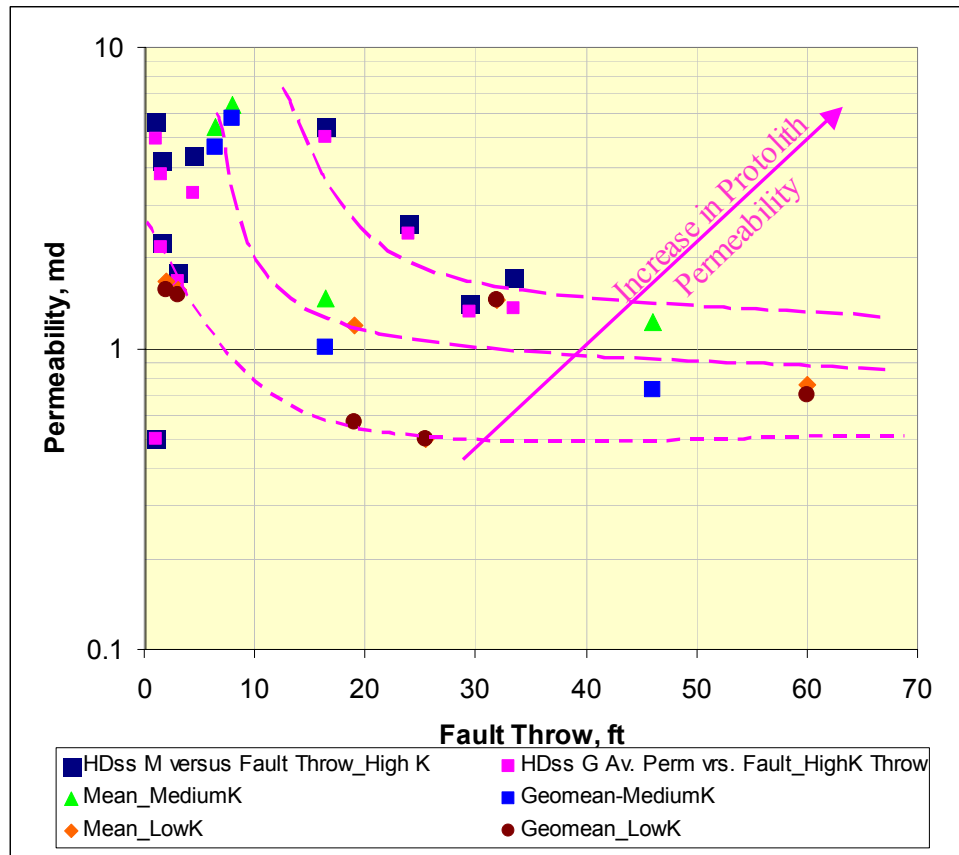


Fig. 3.8 – Permeability of HDss elements versus Fault Throw according to arithmetic and geometric means of protolith permeability.

Ibañez studied the spatial ordering of deformation elements defining matrixes for the studied intervals and evaluating the statistical meaningful tendency for certain deformation elements to be in contact with others. The matrixes were compared using the χ^2 statistic as described by Davis,³⁸ indicating that a key statistical relationship exists between the host rock and the highly deformed elements. He found that 83% of the time, the protolith is in contact with HD elements when the protolith is in contact with the shear zone. On the other hand, he states that there is not an apparent or predictable order of HD, MD and RUD elements, possibly due to the slip movements of the deformed rock within the shear zone.

The fact that most of the time protolith is in contact with highly deformed elements, joined to the predictable behavior of these elements, suggests that HD elements could be one of the most important elements affecting overall shear zone permeability when the amount of clay is low and its continuity is insignificant. This observation, disregarding lithologic considerations, suggests an important step for the characterization of shear zones in low shaliness sequences and the understanding of the effect on transmissibility between blocks for variable fault throws. The analysis of the importance of these specific elements will be further evaluated under analytical and numerical evaluation.

Data from Hickory sandstone member shear zones (at the particular fault of investigation) show a fair to good correlation between fault throw and the thickness of whole shear zone (**Fig. 3.9**) and thickness of highly deformed elements (**Fig. 3.10**). These correlations are based on compiled information from former investigators^{25,26} exhibiting coefficients of determination, R^2 , of 0.55 for the total shear zone thickness and 0.43 for HD element thickness. From same analysis and consistent with observations in permeability for moderate deformed elements, no practical correlation ($R^2=0.05$) is found from the integrated data for these particular facies.

Although the coefficients of determination are not totally statistically satisfactory, these trends observed in the correlation with geological variables can be used to reduce uncertainty in models that can be calibrated in different areas.

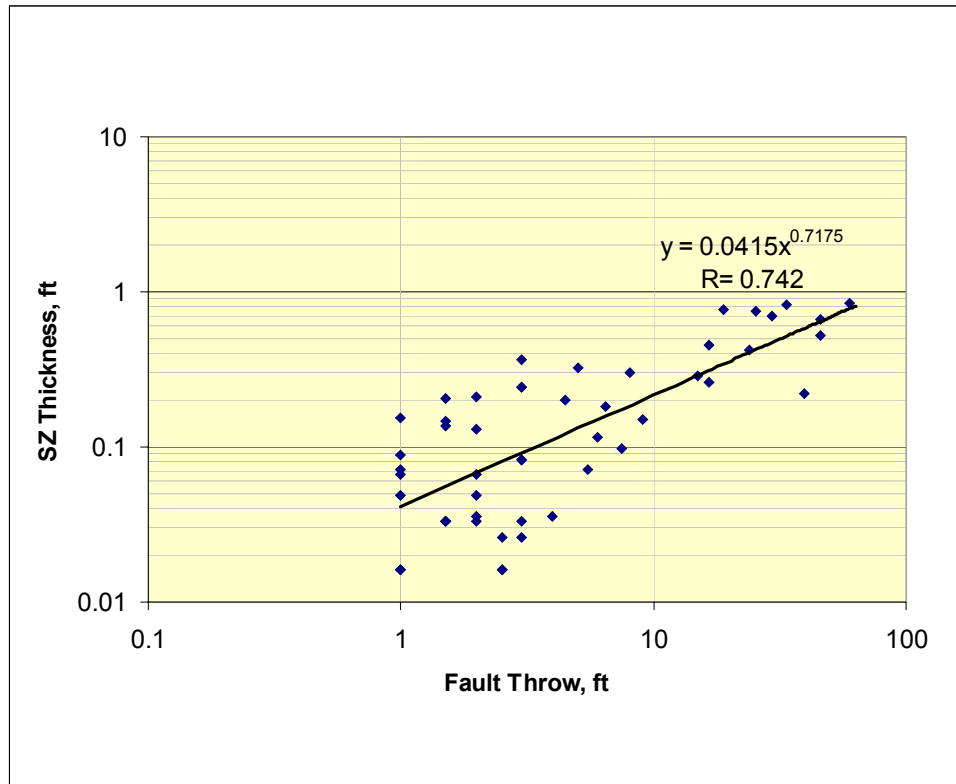


Fig. 3.9 – Total Shear Zone Thickness –Fault Throw Correlation. Data integrated from Ibañez and Wilson^{25,26}

As stated by Ibañez, the relationship found for thickness prediction has similar relationship to other studies that have investigated this function, such as Robertson (1983), Scholz (1987), Hull (1988), and Evans (1990).²⁵

3.5 CT Scanning Integration

We used and integrated CT images for analyzing the internal three-dimensional framework of the selected samples. CT predicts the density (and porosity) of deformation bands and was used to correlate with permeability. In subsequent stages of this integrated project, CT is used for the construction of numerical simulation models by defining the internal correlation, layering and controlling surfaces that allow to generate the property volume to predict the whole-core permeability.

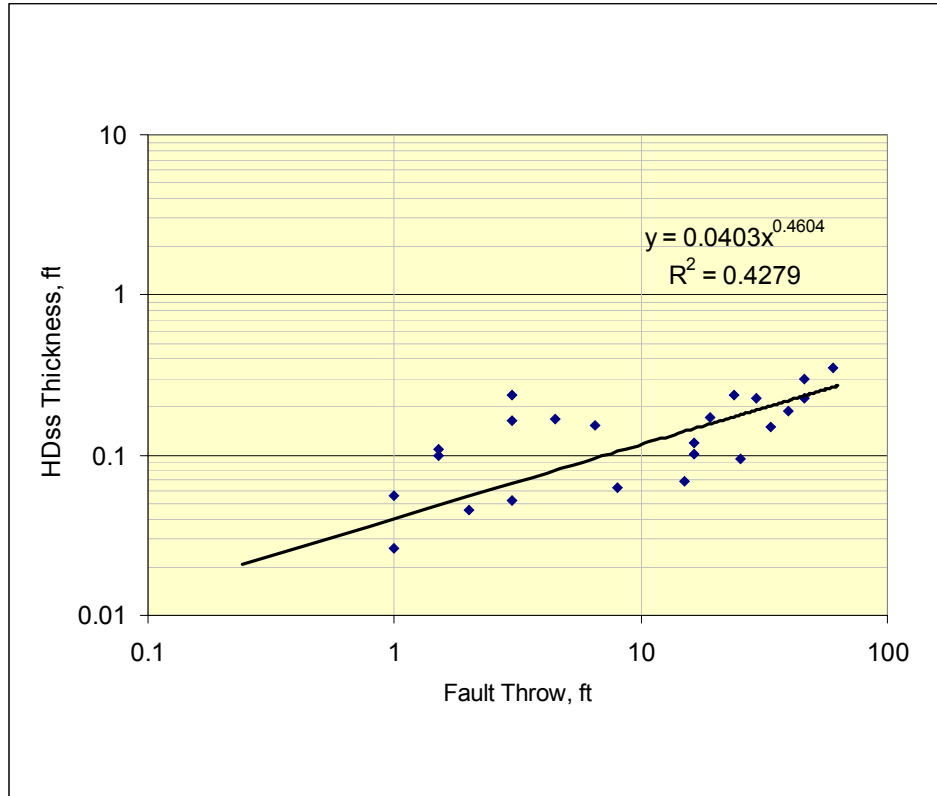


Fig. 3.10 – HD element Thickness –Fault Throw Correlation. Data integrated from Ibañez and Wilson^{19,20}

The main output from tomography is a series of images representing CT attenuation data in an internationally standardized scale called Hounsfield units or CT number.³¹ In general, each Hounsfield unit represents a 0.1% change in density. A change in density is reflected by a change in CT number. Our study did not use the quantitative density prediction because of the difficulty of determining an exact calibration for various non-homogeneous samples.

Comparison of the permeability measurements and CT number for the four cores showed a general inverse relationship between these two variables (**Fig 3.11**). If we

assume a constant original matrix density, we also observe a general decrease in porosity and permeability with increasing degrees of deformation (**Fig. 3.11**). Highly deformed elements do not follow the same general trend however, as observed for moderate and relatively undeformed elements. This suggests that, after a moderate degree of deformation experienced by a specific part of the shear zone which decreases porosity and permeability, additional deformation may transform this zone to a highly deformed feature and cause significant permeability deterioration although porosity may not be affected in the same intensity.

This behavior identifies deformation bands as independent flow units and rock types with a specific porosity/permeability relationship. In other words, porosity is not a unique permeability predictor. For this reason, the geometry and distribution of deformation bands are necessary for addressing the prediction of detailed permeability configuration.

The CT images of the four cores show internal layering created by shear forces within the fault zone in the high throw zones (**Fig. 3.12**). At the top of this figure is shown the calibration between probe permeameter measurements, deformation elements and CT number in one section of core NNR4_404, and the 3D integration of all available scanned images, getting a tangential cut through the oriented section. The lower most section shows a vertical slice through the core showing the internal shear zone layering (**Fig. 3.12**). From such internal visualization, it is possible to assume the continuity of individual deformation elements, information that will be incorporated in the tridimensional modeling of the cores for considering the permeability anisotropy physically related.

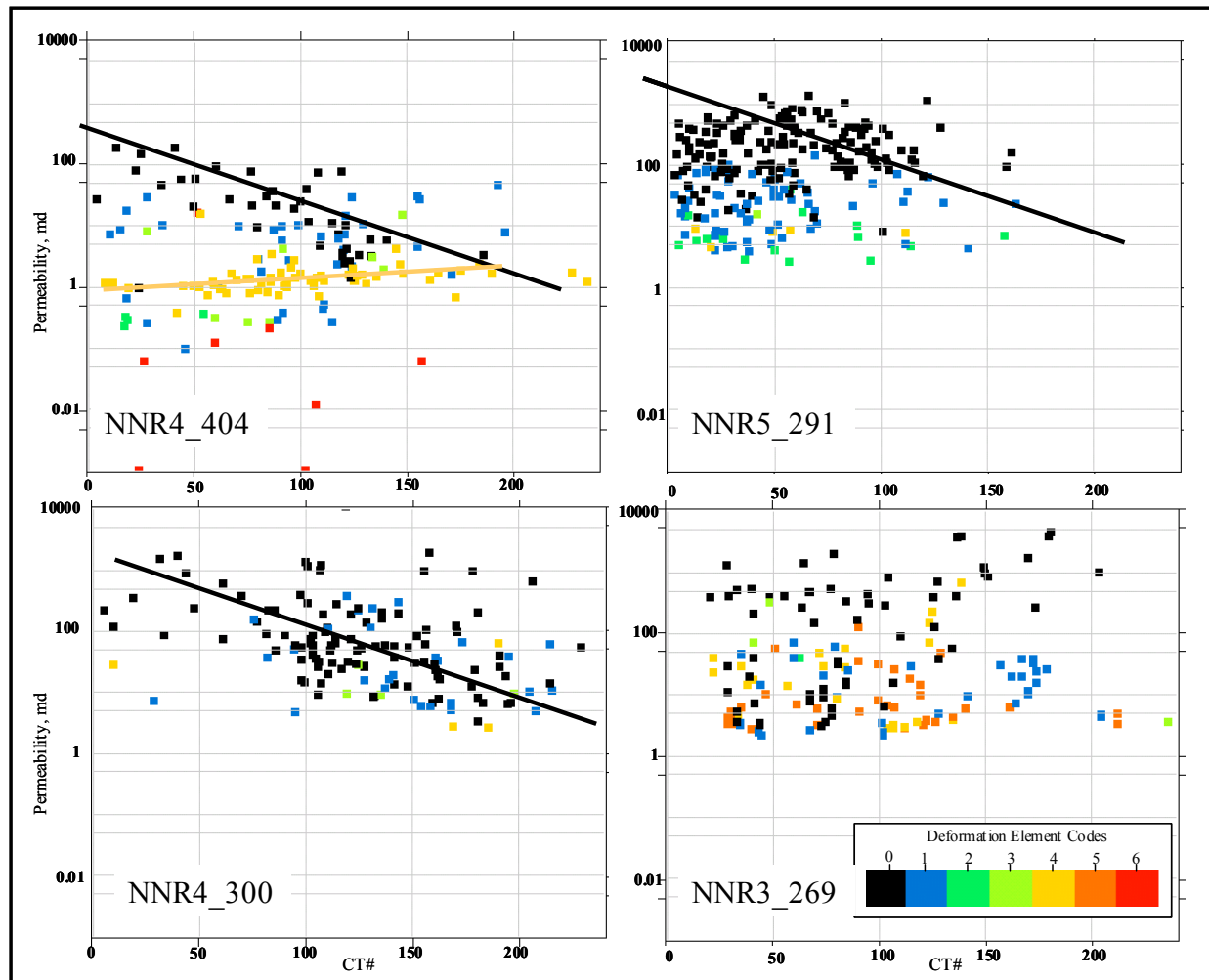


Fig. 3.11 – Permeability, CT #, and deformation elements (color scale, 0 Undeformed – 6 Highly deformed clay) for the four shear zones in the Hickory. Highly deformed features, HDss (4) and HDcl (6), have distinctively low permeability with a characteristic permeability/CT number relationship. Fair to good degree of correlation in RUD facies (black line)

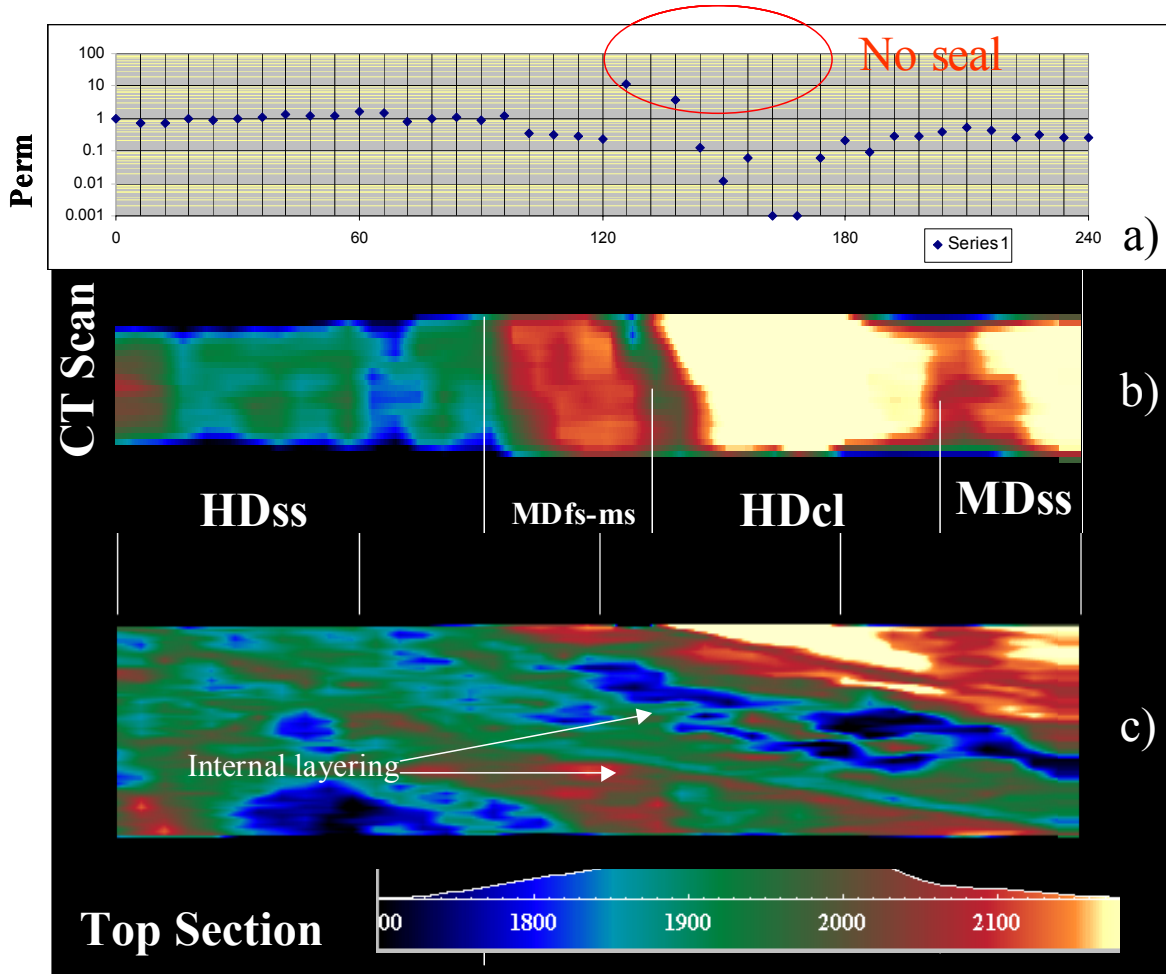


Fig. 3.12 – NNR4_404 top section. a) permeability profile, b) tangential cut at the top of the core, c) vertical cut through the core showing shear layering.

3.6 Whole Core Permeability Measurements

Whole-core permeability measurements were performed in the laboratory following fluid removal by oven drying at 220° F. Porosity was determined by direct pore volume estimation using Boyle's law helium expansion while bulk volume was measured by Archimedes' principle.^{39,40} The analyzed samples did not show significant variability in either porosity or grain density (**Table 3.3**)

Table 3.3 – Laboratory estimations of porosity, permeability and grain density for whole-core

CORE	Fault Throw ft	Lab. Whole-core Porosities, Grain Density and directional permeability. ^{33,34}				
		Helium Porosity %	Grain Density Gr/cc	Vertical md	Along SZ md	Across SZ md
		NNR3_269	4.5	12.2	2.66	12.2
NNR4_300	6.5	12.6	2.65	12.6	91.036	31.4
NNR5_291	29.5	14.6	2.65	55.1	142.7	100.5
NNR4_404	60	12.2	2.63	6.165	12.43	7.67

The whole-core permeability was measured in the horizontal and vertical directions while the core was confined in a Hassler rubber sleeve at 400 psi net confining stress. Horizontal permeability measurements were taken in directions parallel and perpendicular to the azimuth of the main shear plane. Therefore, parallel-horizontal permeability corresponds to the along-fault flow direction while the perpendicular-horizontal permeability is equivalent to the across-fault flow direction. **Fig. 3.13** shows the configuration for horizontal injection of air along a 90-degree surface and production at the opposite side through a similar angular opening.

Along and across-fault permeabilities were calculated in the laboratory using the following expression:

$$K = G \frac{Q_2 \mu}{L} \frac{2P_2}{P_1^2 - P_2^2} \quad (3.5)$$

where K is the average permeability, G the geometrical factor according to Collins⁴¹ estimations depending of angular opening on one side of the core (**Fig. 3.13**), Q the volumetric rate at downstream pressure P₂, L the length of the core, P₁ the pressure at the inlet, and μ the fluid viscosity.

For estimation of vertical permeability, the most common form of Darcy's law is defined as:

$$K = \frac{Q_b \mu L}{A} \frac{2P_b}{P_1^2 - P_2^2} \quad (3.6)$$

where K is the sample permeability in darcys, Q_b and P_b the volumetric rate (ml/sec) and pressure (atm) at point of measurement, L the length of the core (cm), A the cross sectional area(cm^2), μ the fluid viscosity in cp, P_1 the pressure (atm) at the inlet and P_2 the pressure at the outlet. For both cases and as part of the numerical simulation procedure, horizontal and vertical estimations, were developed using laboratory units, K in darcys, Q in scc/hour; μ in cp; L in cm, A in cm^2 ; and pressure in atmospheres.

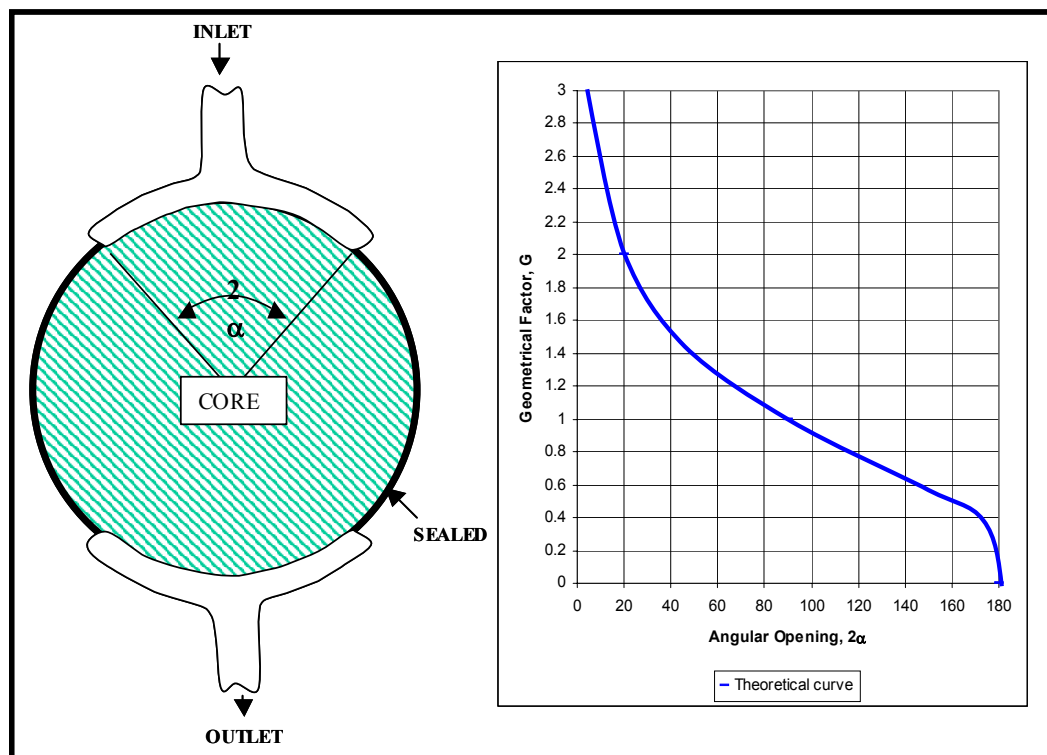


Fig. 3.13 – Design for laboratory measurement of horizontal permeability and theoretical curve for the determination of geometrical factor. From Ref. 41.

3.7 Hassler Permeameter Measurements

Six plugs extracted from selected locations in shear zones and protolith from the available cores were the input for analyzing single (as possible) and commingled deformation element permeability and compare with probe permeability values and analytical results at plug scale. All the plug samples had a diameter between 2.384 and 2.437 cm with lengths ranging from 2.256 up to 5.125 cm (**Table 3.4**). This variability in length is a product of the difficulty in extracting continuous plug samples using the rotary extraction tool without breaking them. Additionally, samples have to be edge-trimmed to ensure square, flat ends and absence of sharp-edge depressions that could give erroneous measurements and/or damage the sleeve.

The Hassler-sleeve permeameter is composed by a core-holding section, a section where the pressure of gas introduced to the sample is regulated and measured, and a downstream section where the flow rate is measured. According to the upstream pressure applied, the gas pressure may be adjusted by either a high or low range regulator and measured using a downstream gauge. All this procedure can be performed while diverse conditions of overburden pressure are set for the core holder. Permeability of the samples is calculated using Darcy's equation according to the upstream and downstream pressures, flow rate at atmospheric pressure, nitrogen viscosity, and the physical dimensions of the sample. This equation is same as given in Eq. 3.6 but considering that Q_b and P_b , the volumetric rate and pressure are at standard conditions.

In addition to the extracted core plugs, two calibration plugs (same used for probe calibration) of 1000 md and 25 md were used to control the repeatability of measurements and compare with probe permeability measurements under known conditions.

Table 3.4 – Hassler permeameter plug data for various deformation element arrangements and according to different net overburden pressure (NOBP). Included here, probe permeameter data and averaging results (discussed in Chapter IV)

PLUGS	Sample	Probe Perm	Facies	Harm	Geo	Mean	Hassler Perm	Dimensions	NOBP
		md		Av	Mean		md		psig
NNR4_300_loc1	Top1	58.7	RuD & HDss	30.55	34.16	37.93	68.999	Length(cm) 5.125 Area(cm ²) 4.665	380.7
	Top2	18.6	RuD & HDss				67.262		370.1
	Top3	36.5	RuD & HDss						
NNR3_269_loc2	Top1	4550	Protolith	2166.20	2573.80	3057.50	1481.953	Length(cm) 4.169 Area(cm ²) 4.536	169.0
	Top2	4860	Protolith				1564.608		169.0
	Base1	1350	Protolith				1545.889		230.6
	Base2	1470	Protolith				1515.144		330.0
							1580.867		320.2
			1549.847	496.2					
NNR3_269_loc3	Top1	5.55	HDss	8.15	9.05	10.05	8.484	Length(cm) 2.310 Area(cm ²) 4.666	377.6
	Top2	5.86	HDss				6.615		377.5
	Base1	13.3	HDss+cl				8.999		389.1
	Base2	15.5	HDss+cl						
NNR5_291_loc4	Top1	110	RUDms	9.79	17.08	51.50	23.170	Length(cm) 4.685 Area(cm ²) 4.464	403.8
	Top2	133	RUDms				23.767		400.4
	Base1	4.05	MDms						
	Base2	6.89	MDms						
	Base3	3.56	MDms						
NNR4_404_loc5	Top1	3.89	HDss	4.12	4.16	4.19	5.837	Length(cm) 2.382 Area(cm ²) 4.663	506.0
	Top2	4.39	HDss				5.590		497.1
	Base1	4.96	HDss						
	Base2	3.52	HDss						
NNR4_404_loc6	Top1	1.71	HDss	3.79	12.76	31.36	3.063	Length(cm) 2.257 Area(cm ²) 4.583	498.6
	Top2	1.48	HDss				3.285		499.3
	Base1	47.5	MDms						
	Base2	51.3	MDms						
	Base3	54.8	MDms						
Cal @ 25 md	Top1	24.6	SS	21.12	21.26	21.40	45.965	Length(cm) 3.876 Area(cm ²) 5.007	98.0
	Top2	22.9	SS				27.247		146.4
	Base1	18.4	SS				26.633		202.3
							23.251		200.2
	Base2	19.7	SS				23.049		327.5
							22.419		326.3
							20.781		459.6
							20.801		538.6
Cal @ 1000 md	Top1	734	SS	748.65	748.70	748.75	1271.965	Length(cm) 3.899 Area(cm ²) 4.980	47.4
	Top2	753	SS				1097.997		104.4
	Base1	756	SS				1045.523		147.9
							1019.709		247.6
	Base2	752	SS				1019.709		321.0
							1012.035		362.8
							1007.897		455.3

As demonstrated with the use of the two very homogeneous calibration-samples (**Table 3.4**), probe permeameter is measuring between 15 and 25% lower permeability than the calibrated (true) value. This effect could be explained due to surface conditions of the sample or the necessity of an accurate geometrical calibration for the estimation of permeability according to the probe tip used. Although this effect has to be carefully evaluated when getting probe permeabilities with the purpose of field scale calibration and integration, our target here is to have a consistent evaluation, and for that reason, each tool was evaluated satisfactorily to guarantee consistency and repeatability, giving plenty confidence in the results achieved.

Another very important step and objective for plug evaluation is the analysis of permeability under variable net stress conditions to evaluate the effects of compressibility. This effect is obviously important when having and integrating diverse source of permeability data under conditions ranging from atmospheric to reservoir. The use of variable confining pressure to calculate permeability using the Hassler-sleeve permeameter allows also to identify minimum conditions to guarantee a complete seal between the rubber sleeve and the walls of the sample. Working with calibrated samples under atmospheric conditions assurance to differentiate compressibility effects from leaking problems. From data obtained at overburden pressure from approximately 50 psig up to 550 psig for the two calibrated samples and the plug extracted in the protolith at location NNR3_269 loc2, we can evaluate the minimum overburden pressure above the upstream pressure that should be applied to the samples to guarantee sealing capacities of the sleeve.

With the Hassler-sleeve permeameter available for this study, we need to have at least 200 psi above the upstream pressure in the overburden pressure to have reliable results of permeability (**Fig. 3.14**). Unfortunately this high threshold does not permit to examine the effects of compressibility under low confining pressure, but, if we analyze the results from protolith at NNR3_269, the very small change in permeability (less than 1.9% for the maximum difference in permeability, from 230 to 500 psig of confining pressure, **Table 3.4**) suggests the weak effect of compressibility in these rocks.

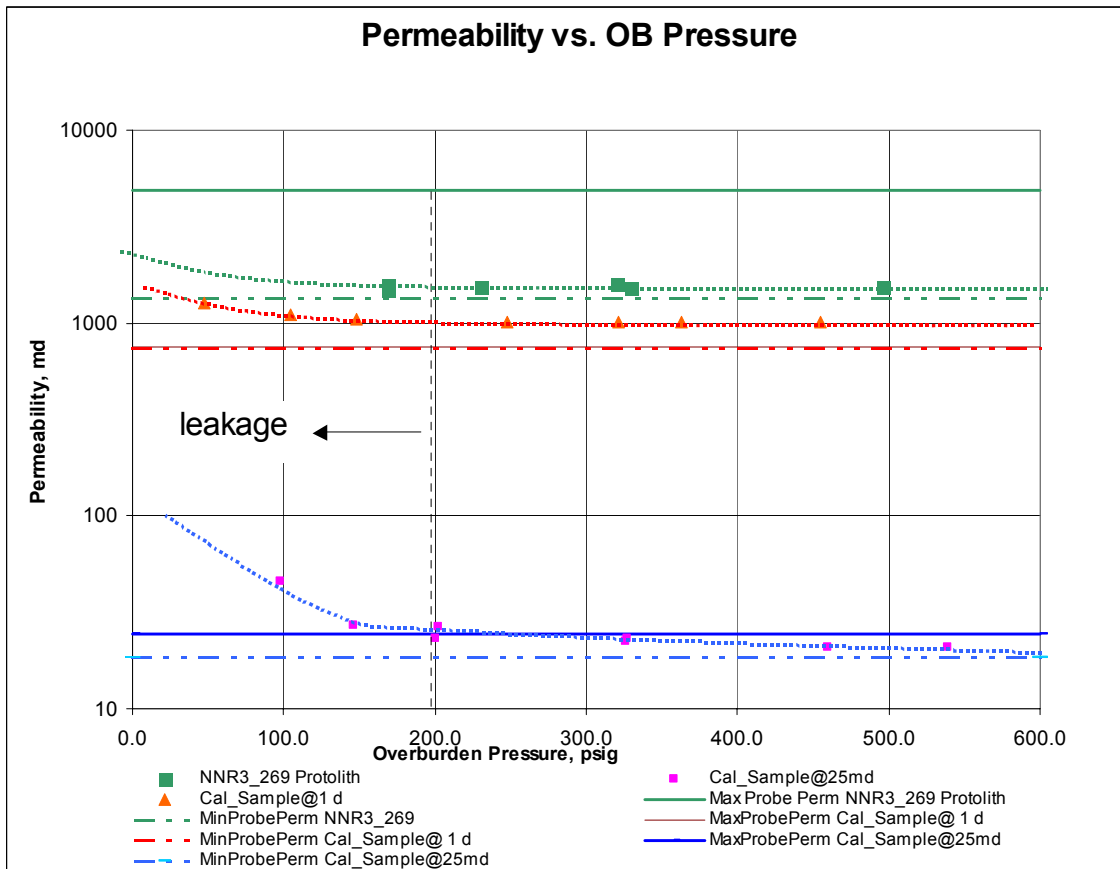


Fig. 3.14 – Plug permeability (Hassler-sleeve Permeameter) versus overburden pressure for protolith at NNR3_269 and two calibration samples. Minimum and maximum probe permeameter is also referenced.

The mixed or commingled deformation element plugs are represented by a sample of a very heterogeneous arrangement of facies of relatively undeformed and highly deformed sandstone elements in location NNR4_300 loc1 (2 cm below the base of core in transect 3, Fig. 3.5), with total permeability of around 69 md (Table 3.4). Probe permeability data identified specific points in the sample where permeability was as low as 18.6 md, and it should be interpreted as the effect of the tiny HDss elements in the core. This sample showed some vugs or holes of up to 1 cm in their longest axis.

These anomalous pore structure could have been generated during fault movement, gouge generation and with the possibility of being exposed to water washout.

The sample at NNR5_291 loc4 (**Fig. 3.4**) represents a very heterogeneous- non organized arrangement of relatively undeformed and moderate deformed medium sandstone elements with total Hassler-sleeve permeability of approximately 23 md while probe permeameter reported high permeability values up to 133 md at top of the plug and low moderate deformed element permeability at base of the order of 4 md (Table 3.4).

At location NNR4_404 loc 6 (**Fig. 3.3**) was sampled a layered arrangement of HD elements at top and moderate deformed facies at bottom. Hassler-sleeve permeameter data calculated a total vertical (according to layer dip) permeability of around 3 md (Table 3.4). Probe permeameter data showed consistent results for this arrangement of facies and according to former measurements on the surface of the core sample.

Plugs that investigate the permeability of single deformation elements are those located at NNR3_269loc2, NNR3_269loc3, and NNR4_404loc6. The protolith sampled at location NNR3_269loc2 (3.5 cm below the base of core sample NNR3_269 at transect 1, Fig. 3.6) showed Hassler-sleeve permeabilities between 1545 and 1581 md while minimum permeability reported from probe is 1350 md (**Table 3.4, Fig. 3.14**). The maximum values reported from probe permeameter tend to show considerable high values of around 4550 md. These anomalous values higher than expected could be attributed to the unconsolidated nature of the sample, the effect that this characteristic could improve surface permeability by grain loose and the high chance of poor seal during probe permeability measurement.

Sample at NNR3_269loc3 (**Fig. 3.6**) recovered a mixed layered arrangement of highly deformed sandstone at the top and highly deformed sandstone plus clay at bottom, showing from probe permeability measurements the same characteristic from surface measurements, that is the improvement in permeability when clay is part of the

structure of the element (**Table 3.4**). From this plug, Hassler-sleeve permeameter values range from 6.6615 and 8.999 md.

The sample at NNR4_404loc5 sampled the characteristic tabular highly deformed element present in the shear zone in that particular fault location (**Fig. 3.3**). Values from probe and Hassler-sleeve permeameters agree very well (differences of approximately 1 md) although, when comparing with original measurements on core sample using probe (**Fig. 3.3**), the differences are higher, up to 3 md. Considering that probe measurements exhibit differences between those obtained on core and plug surfaces (under same conditions and tips), showing higher values in trimmed (fresh plugs), it is possible to suggest that some reduction in permeability could be produced by alteration (plugging?) of samples while they are maintained at surface conditions.

CHAPTER IV

PERMEABILITY UPSCALING USING AVERAGING TECHNIQUES

Two main methods were evaluated for getting whole-core permeability measurements. The first is the evaluation of analytical techniques using averaging methods and the second, the use of static modeling of permeability and the dynamic evaluation of whole-permeability using numerical simulation (Chapter V). The purpose of doing both ways is to try to understand when simple techniques give a good estimation of permeability in shear zones and when they do not. The more sophisticated techniques will help to understand the effect of small deformation features in the permeability tensor and give ideas of their potentiality as effective barriers along or across shear zones.

4.1 Upscaling Permeability at Core Scale

In order to have a first analysis of possible analytical solutions to solve for the permeability tensor, we have to consider the geometrical configuration of shear zones compared with the cylindrical shape of the sample. Considering this issue, shear zones at NNR5-291, NNR4_300, and NNR3_269 represent valid samples to compare these analytical solutions because flow evaluation can be done perpendicular to main shear zone avoiding having high permeability facies joining inlet and outlet of core.

Contrasting with this, sample NNR4_404 presents a preferential flow at transverse 3 (**Fig. 3.1**) when inlet and outlet are joined by RUD and MD elements causing channeling that avoids an evaluation of the total permeability effect by shear zone at this particular location. In other words, harmonic upscalers will assume total continuity of low permeability elements, model that is not valid for the evaluated whole-core sample. This effect is causing the very low whole-core permeability obtained under analytical solutions for this core. More detailed analysis and considerations will be discussed with the tridimensional modeling of deformation elements for the exact laboratory sample geometries.

The NNR5_291 sample shows satisfactory agreement between harmonic averages and vertical laboratory permeability (**Table 4.1**). Using the mean permeability of deformation elements, harmonic average is 0.91 times the true calculated permeability while if using the median permeability value, the harmonic average is 0.55 times. Considering the continuity of deformation elements in this core, we can conclude that harmonic averages reproduce very close the true perpendicular-to-shear-zone permeability, in this case, represented by the vertical flow.

Sample at NNR4_300 has a reverse effect from that observed in sample NNR4_404; the harmonic average permeability is 6.2 and 2.7 times (using mean and median permeability respectively) greater than laboratory calculations for vertical permeability and two general considerations can be assumed from this result. First, the high degree of heterogeneity observed in this core could infer that the best upscaler should use the median permeability from particular elements, and second, that the tiny high-deformed elements could have lower permeability values compared to those reported from probe permeameter data. This anomaly is possible if our permeability determination is below areal resolution of the probe tip. These effects will be re evaluated in our modeling and numerical simulation step with the effective match procedure with laboratory data, using detailed sampling with 1” plugging and with focused sampling in strike oriented exhumed surfaces.

Sample at NNR3_269 also shows a fair to good agreement between calculated analytical values and laboratory results for vertical flow.

Along shear-zone permeability is closely reproduced using arithmetic averages of mean permeability of deformation elements, exhibiting analytical to lab permeability ratio between 2.45 and 0.95. Using median permeability values, this ratio falls between 0.78 and 0.6.

Table 4.1 - Comparison between arithmetic, geometric, and harmonic averaging with laboratory whole-core permeability measurements.

CORE	Fault Throw	Mean K (md)			Median K (md)			Lab. Whole-core Perm.		
		Arith.	Geom.	Harm.	Arith.	Geom.	Harm.	Vertical	Along SZ	Across SZ
	ft	md	md	md	md	md	md	md	md	md
NNR3_269	4.5	265.502	99.302	33.185	113.609	41.387	12.26	12.2	145.23	8.1
NNR4_300	6.5	223.014	108.968	77.634	54.658	40.168	33.892	12.6	91.036	31.4
NNR5_291	29.5	191.043	119.15	50.084	121.812	74.926	30.571	55.1	142.7	100.5
NNR4_404	60	11.864	3.902	0.768	7.011	2.764	0.662	6.165	12.43	7.67

Arithmetic average: $\Sigma(\text{Pi} * \text{Ki})$; Geometric $\text{EXP}\{\Sigma(\text{Pi} * \ln\text{Ki})\}$; Harmonic: $\{\Sigma(\text{Pi} / \text{Ki})\}^{-1}$

If we incorporate a power law function as also used by Myers¹⁹ to investigate the optimal upscaler to match laboratory data, an exponent value of $w = -1$ is representing geometries of deformation elements perpendicular to flow direction, in other words, the equivalence to harmonic upscalers. For this calculation, the equation used by Myers can be expressed in function of proportion of deformation elements and the equivalent permeability, as follows:

$$K_{av} = (V_{RUD}K_{RUD}^w + V_{MD}K_{MD}^w + V_{HD}K_{HD}^w)^{1/w} \quad (4.1)$$

where K_{av} is the average permeability, V the volume or proportion of deformation elements (RUD, MD, and HD), and K the mean or median permeability for each element.

Using this approach for matching the laboratory results, vertical permeabilities are more closely reproduced using power exponents with a certain deviation around -1 (**Table 4.2**). Values found in well NNR4-404 correspond in some extent to quasi-parallel flow because facies are not strictly perpendicular according to the core geometry modeled and tested. From a practical point of view, this vertical estimation has a high

component of across-shear-zone permeability, represented by power exponents quite similar between vertical and across directions (**Table 4.2**).

The other anomalous estimation in this direction is obtained when using mean permeability of deformation elements to match laboratory data for well NNR3_269. The high exponent included in **Table 4.2** is an output from a not feasible numerical solution. This means that at least more barriers or lower permeability values should be present in the core for getting the solution. This effect tends to be compensated if the median of permeability by deformation elements is considered. The same analysis and conclusion can be interpreted from results for core NNR4_300.

Along flow power exponents are totally characterized by positive numbers with a mean of 1.4, value that is comparable with the use of arithmetic averaging where the power exponent is 1.

Out of detailed consideration of specific geometry configuration compared to the directional permeability to be calculated, across shear zone permeabilities for these samples exhibit power exponents between these two end members (-1 and 1, for vertical and along shear-zone respectively). This suggests that the best simple upscaler to be used to account for this component in the permeability tensor (the across shear-zone flow) is the geometric average.

According to core surface description and internal architecture from CT imaging, samples from NNR4_404 (**Fig. 3.12**), NNR5_291 and in minor grade core NNR3_269 present layered distribution of deformed elements within the shear zone, parallel to the orientation of the fault plane. If permeability in the whole core has to be estimated in a direction perpendicular to the orientation of the internal shear zone layering, harmonic upscalers will account for the internal structure of series of deformation bands and give a confident average permeability.

The low continuity seen in the deformation elements of core NNR4_300, the low proportions of highly deformed elements as a main controller in whole-core permeability, everything associated with high-quality protolith and low fault throw give the lesser anisotropy based on the three statistical methods analyzed. Although cores

NNR4_404 and NNR5_291 come from the same interpreted fault zone section, protolith quality is almost 15 times better in the second, suggesting that HD elements can still have considerable permeability for fluid flow (~13 md). This arrangement of permeability will cause a preferential along-fault flow in this part of the reservoir although the possibility of being a sealing feature (at this depth) has low probability. Contrary to this spatial consideration, the same fault at 404 ft depth exhibits a high chance to be originally sealing (locally) with very low shear-zone permeability (0.768 md). Ibañez²⁵ found reductions of about three orders of magnitude of harmonic average permeability when using mudstone permeability values as proposed by Gibson.

4.2 Sensitivity of Power Exponents to Facies Proportions and Permeability

Sensitivity analysis of power exponents was performed in order to demonstrate the effectiveness of using simple methods for characterizing the permeability tensor in shear zone intervals and also, to identify the precision of the probe tool in high and low permeability elements and the effect of errors in volume calculation in the overall permeability estimation. With this analysis, we can solve for the possible causes of abnormal power exponents such as values out of the range from 1 to -1, and the no feasible numerical solutions to match laboratory measurements.

Considering whole-core sample geometry and the directional permeability to be estimated, we can expect power exponents to be concentrated around specific values. Harmonic mean is the case when power exponents (w in Eq. 4.1) is equal to -1; geometric mean when $w=0$, and arithmetic mean when $w=1$.³²

Although we have fairly good confidence in the estimation of permeability using the probe permeameter, this analysis considered a 50% difference (above and below) to check if any effect in probe calibration could be the cause of getting no feasible or abnormal numerical results. As the same manner, a reduction (2.5 and 10%) and increase (5 and 10%) of the volume of the highly deformed elements were considered. Finally, a systematic reduction of 80% of the highly deformed sandstone permeability

was additionally analyzed to consider possible problems related to the probe vertical resolution when these elements are thinner than probe diameter.

Table 4.2 – Solving for power exponents matching laboratory calculations. Shaded cells are values that should be considered to represent that particular direction according to shear zone configuration (dip/azimuth) and core geometry.

Core NNR4_404	Power Exponents			LAB DATA			Power Average			Difference
	Vertical	Along	Across	Vertical	Along	Across	Vertical	Along	Across	
Mean	0.33			6.17			6.17			0.00
Median	0.81			6.17			6.17			0.00
Mean		1.07			12.43			12.43		0.00
Median		2.72			12.43			12.43		0.00
Mean			0.51			7.67			7.67	0.00
Median			1.16			7.67			7.67	0.00

Core NNR5_291	Power Exponents			LAB DATA			Power Average			Difference
	Vertical	Along	Across	Vertical	Along	Across	Vertical	Along	Across	
Mean	-0.89			55.10			55.10			0.00
Median	-0.36			55.10			55.10			0.00
Mean		0.28			142.70			142.70		0.00
Median		1.89			142.70			142.70		0.00
Mean			-0.22			100.50			100.50	0.00
Median			0.48			100.50			100.50	0.00

Core NNR3_269	Power Exponents			LAB DATA			Power Average			Difference
	Vertical	Along	Across	Vertical	Along	Across	Vertical	Along	Across	
Mean	N.D.			12.20			N.D.			N.D.
Median	-1.01			12.20			12.20			0.00
Mean		0.28			145.23			145.23		0.00
Median		1.72			145.23			145.23		0.00
Mean			N.D.			8.10			N.D.	N.D.
Median			-1.85			8.10			8.10	0.00

NNR4_300	Power Exponents			LAB DATA			Power Average			Difference
	Vertical	Along	Across	Vertical	Along	Across	Vertical	Along	Across	
Mean	N.D.			12.60			N.D.			N.D.
Median	-9.66			12.60			12.60			0.00
Mean		0.05			91.04			91.04		0.00
Median		3.27			91.04			91.04		0.00
Mean			-4.73			31.40			31.40	0.00
Median	he results of		-1.34			31.40			31.40	0.00

Analyzing the results of sensibility for core NNR4_404 for all the directional permeability considering that this sample does not represent a perfect perpendicular flow in none of the main directions, and is highly layered, we can interpret that an increase in permeability (about 50% from probe permeameter) or a decrease in the volume of highly deformed elements result in a coherent representation of power exponents under known conditions (**Fig. 4.1**). The fact that this sample has been effectively measured and characterized with low permeability variability in each deformation element and high confidence in the facies proportions suggest that the higher permeability that is reported in laboratory compared with analytical solutions could be the result of small fractures and joints that cross the sample parallel to the shear zone.

For core NNR5_291, the sensitivity analysis (**Fig. 4.2**) shows the effect of errors in volume and permeability estimations from probe exhibiting the good results from the original values considered. Here, as seen in core NNR4_404 and in general, in all the analyzed samples, mean permeability of each deformation element tends to give better analytical results compared to the expected power exponents according to each directional analysis. Thus, along shear zone permeability is satisfactorily represented by the arithmetic permeability, cross shear zone by the geometric and the vertical component by the harmonic average (**Fig. 4.2**)

Core NNR4_300 (Fig. 4.3), a very heterogeneous sample with small highly deformed elements, is a good example to examine the effect of these small features and the common probe of vertical resolution of the probe to effectively characterize these elements. The unique feasible solution agrees with this layering arrangement of perpendicular flow upscalers (harmonic) for the across and vertical direction, and normal arithmetic for the along shear zone direction. For having congruent results according to this configuration, the permeability of the highly deformed elements has to be reduced about 80% to obtain a match between lab data and analytical results under the range expected. This observation suggests and confirms the problems of precise permeability estimation using probe permeameter when highly deformed features are narrow bodies.

This anomaly will be important when characterizing low-fault-throw shear zones because the low thickness and continuity of these elements.

Finally, core NNR3_269 (Fig. 4.4) that represents similar geometry to core NNR4_300 and where we could expect similar results in the upscalers to be used, showed the same behavior and a decrease in highly deformed permeability should be considered in order to match the results. The explanation here is not necessarily due to the thickness of the elements and resolution of the tip but could be the effect of surface conditions under some lithological changes. With the selective measurements from surface we have noticed the higher permeability reported in highly deformed facies when there is an increase in shale content. These phenomena could be merely superficial and not representative at internal conditions. Nevertheless, this is an issue that should be investigated more deeply.

4.3 Upscaling Permeability at Plug Scale

Two plugs, NNR3_269_loc2 sampling the protolith, and NNR4_404_loc5 sampling the highly deformed element, are considered relative homogeneous sample and different averaging techniques are given similar results. Although we do not discriminate the high variability of the sample from the protolith and we consider for practical reasons that this sample comes from a homogeneous rock, the absence of a notorious layering structure makes us suppose that this sample could be more heterogeneous than expected and more data should be obtained to fully characterize this element. In this case, none of the averaging techniques gave a satisfactory match suggesting that permeabilities as those found at the top of the plug are not characteristic for this rock at this position and some lower values (lower even than those already measured with the probe) should be present along the plug.

CORE NNR4_404

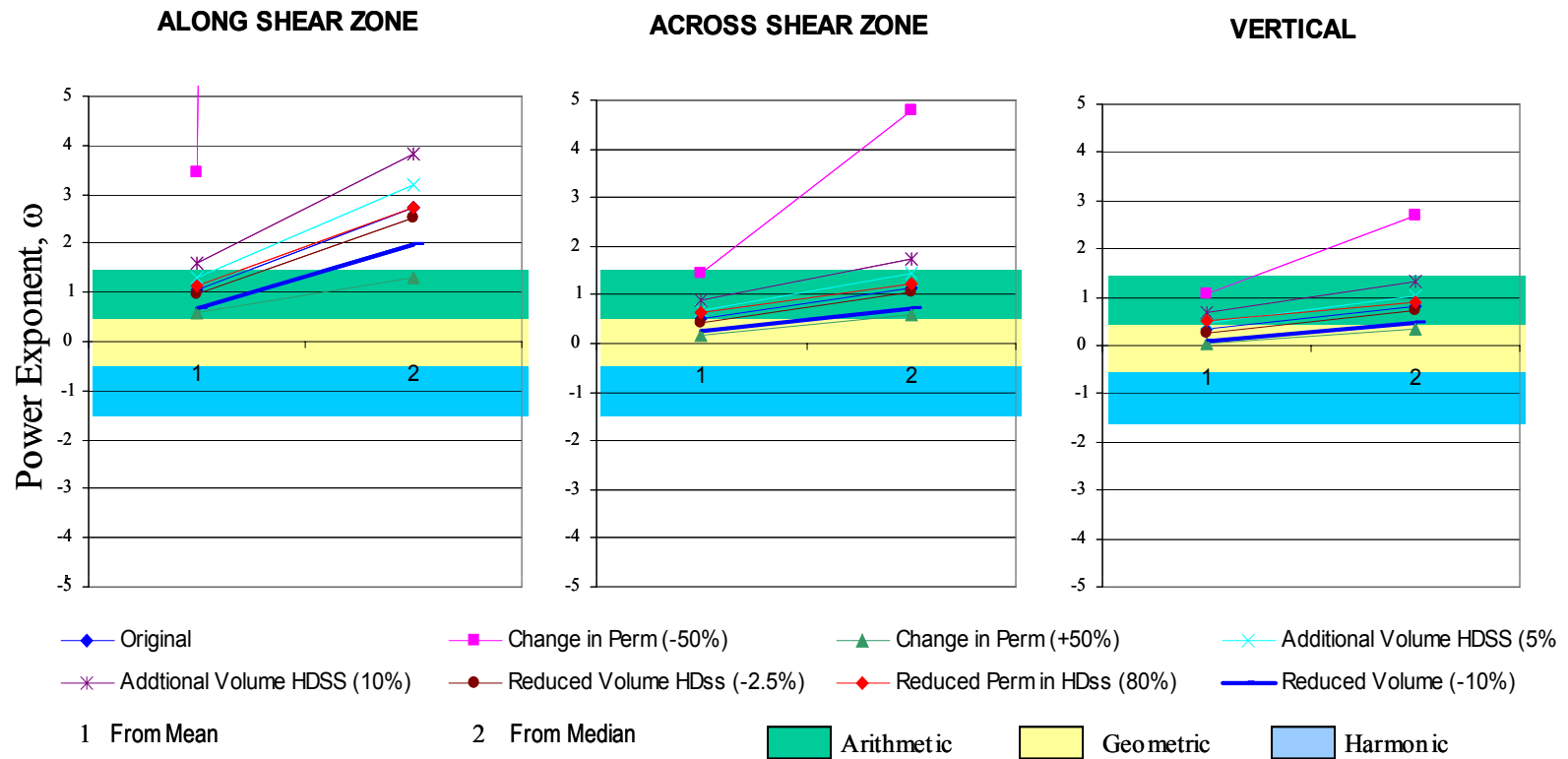


Fig. 4.1– Sensitivity of power exponents to errors in facies proportions and permeability – Core NNR4_404.

CORE NNR5_291

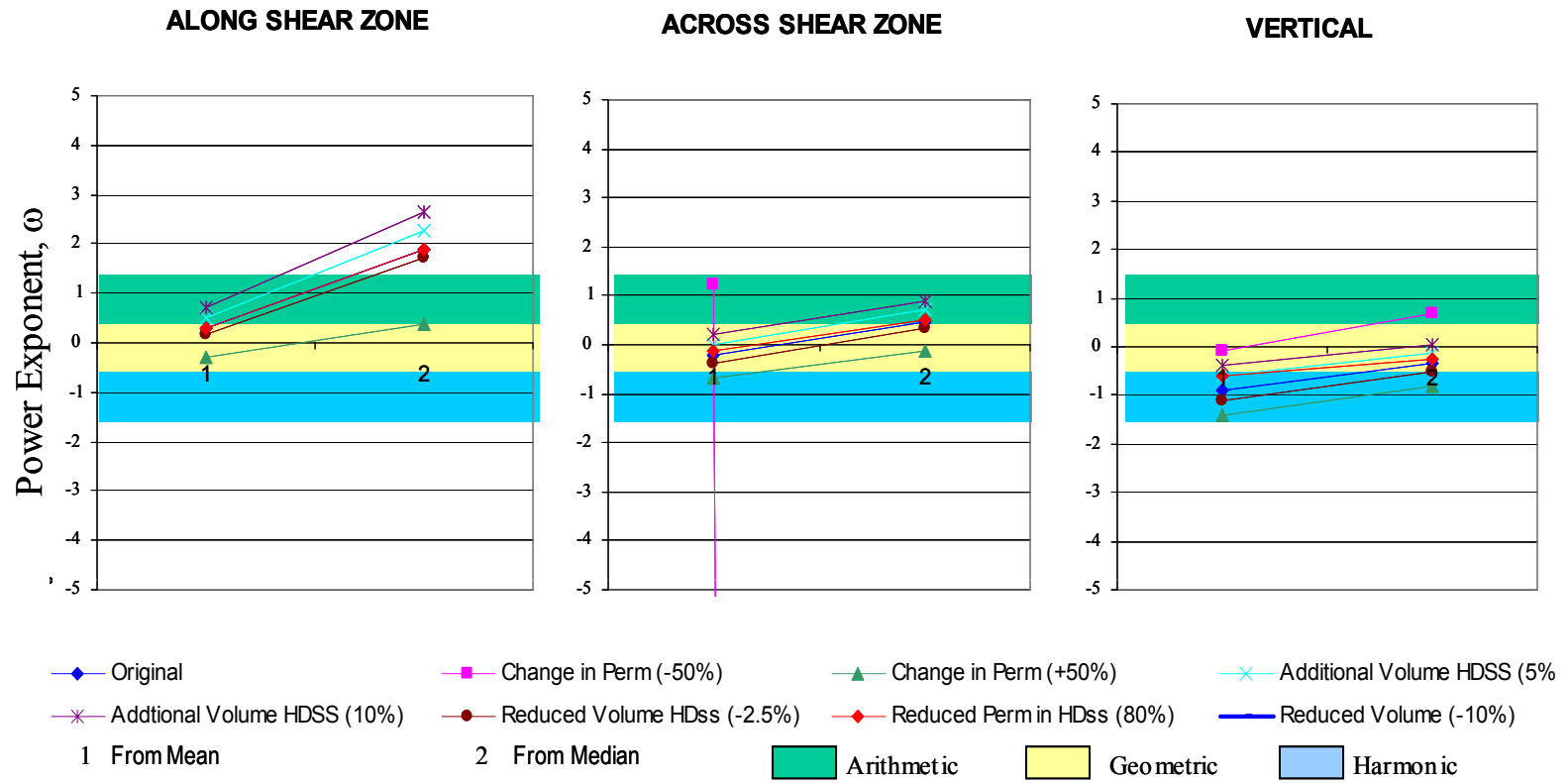


Fig. 4.2– Sensitivity of power exponents to errors in facies proportions and permeability – Core NNR5_291.

CORE NNR4_300

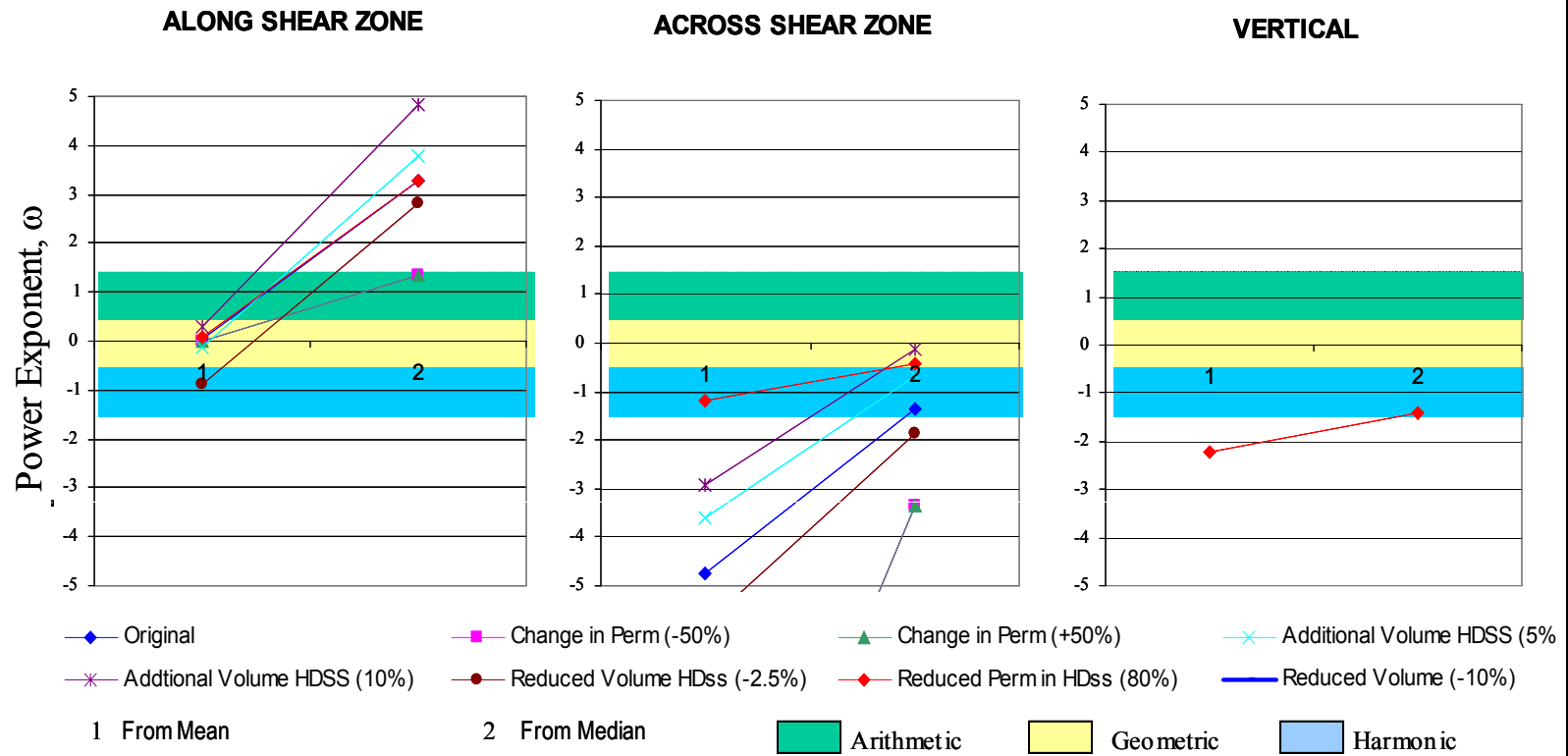


Fig. 4.3– Sensitivity of power exponents to errors in facies proportions and permeability – Core NNR4_300.

CORE NNR3_269

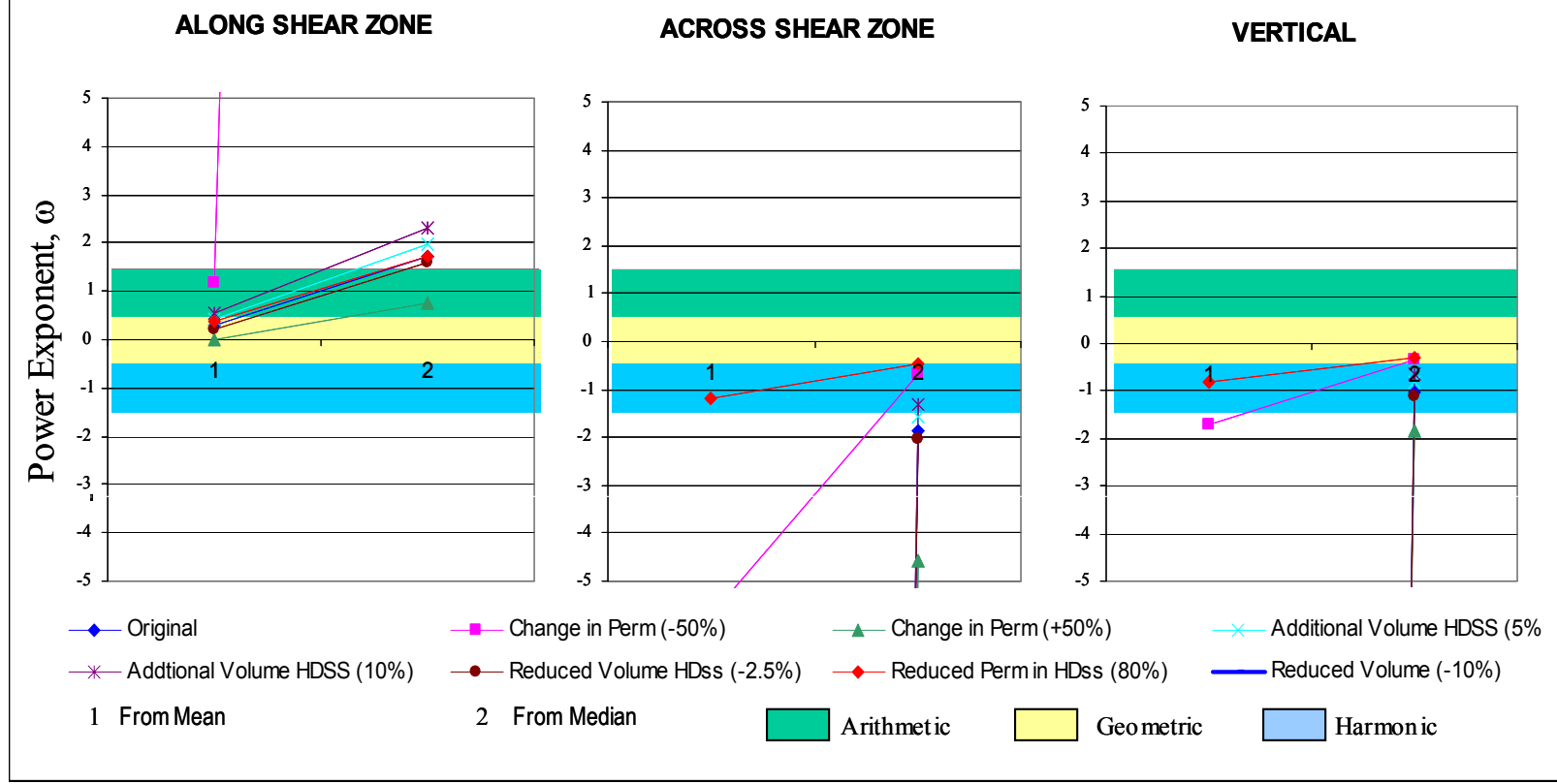


Fig. 4.4– Sensitivity of power exponents to errors in facies proportions and permeability – Core NNR3_269

The second sample at NNR4_404_loc5 is clearly characterizing the highly deformed sandstone element and shows a very good agreement between Hassler permeameter measurements and any of the averaging techniques (Fig. 4.5).

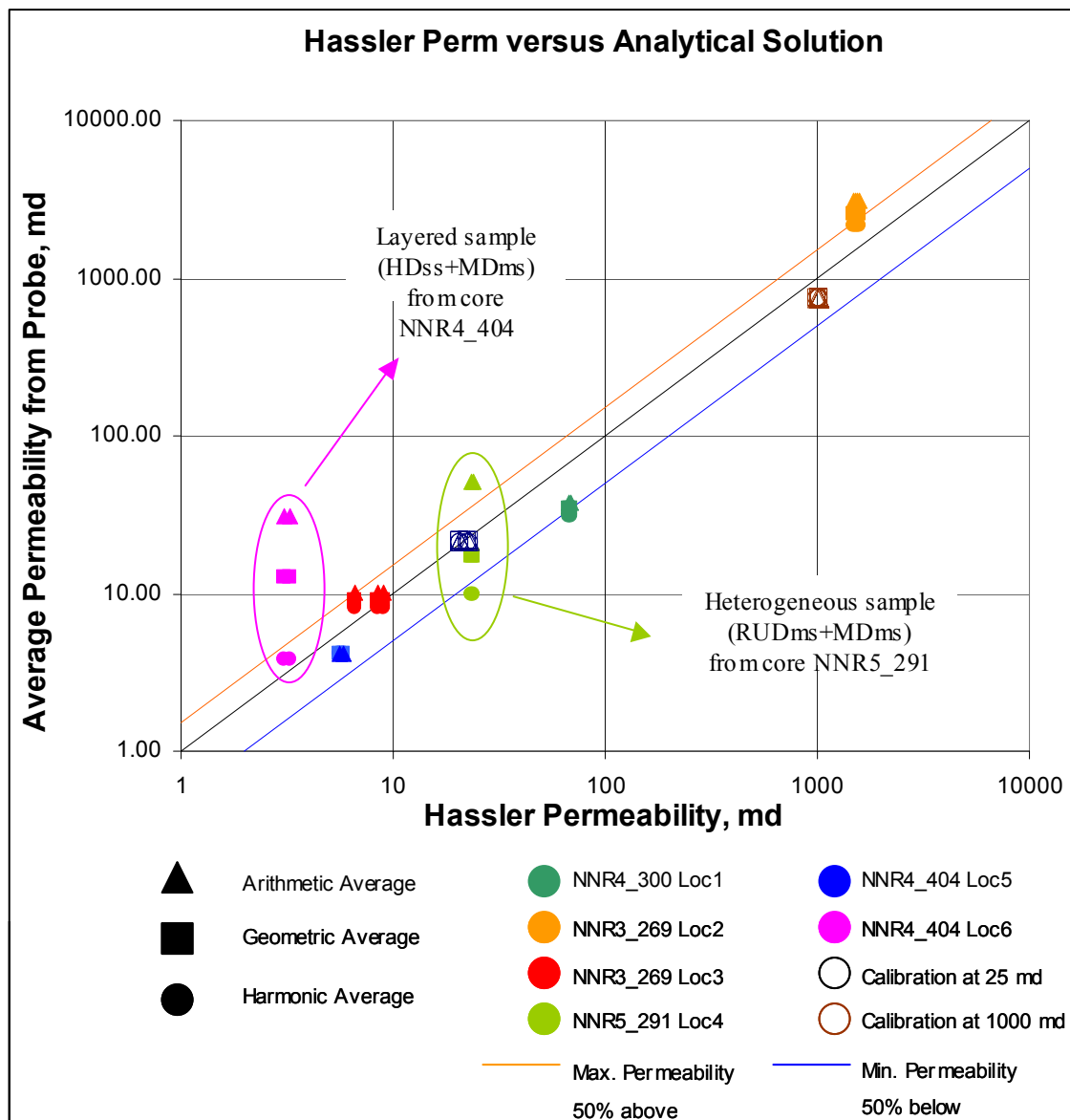


Fig. 4.5– Probe Average permeability versus Hassler permeability for selected plugs.

Two additional samples, at NNR3_269_loc3 composed by highly deformed sandstone and highly deformed shaly sandstone, and NNR4_404_loc6 representing a sucesion of highly deformed sandstone and moderate deformed sandstone, showed results of the upscaled permeability in presence of a clear layered structure. Although the first one presents a small permeability variation between the top and bottom, harmonic permeabilities agree satisfactorily with Hassler permeameter results (**Fig. 4.5**). The same degree of agreement was observed in the sample at NNR4_404_loc6 demonstrating the effectiveness of harmonic averaging techniques for layered systems.

In the other hand, two samples (NNR4_300loc1 and NNR5_291_loc4) exhibited a characteristic un-organized or heterogeneous arrangement. There is a clear disagreement between values reported from Hassler permeameter and those coming from averaging techniques from probe permeameter, showing higher values those coming from the first method. As mentioned before, this plug showed a very important characteristic that was the presence of vugs or secondary porosity produced during or post tectonic movement. The fact that Hassler permeameter has reported an important increase of permeability compared to surface measurements (probe) makes suggest that vugular or any kind of enhance in porosity and permeability is affecting the overall permeability of the sample.

The second heterogeneous sample at NNR5_291_loc4 shows the good agreement between geometric averages and plug permeability from the laboratory, demonstrating that in absence of a layered configuration, and with substantial permeability heterogeneity, geometric upscalers can account for the true overall fluid flow potential of the plug sample.

CHAPTER V

PERMEABILITY UPSCALING USING GEOMETRICAL AND PERMEABILITY MODELING

The tridimensional modeling consisted of several steps: 1) the integration of geometrical characteristics from core surface analysis, 2) the CT imaging loading and volume generation, 3) the modeling and representation of the most important bounding surfaces controlling major facies changes, 4) the reproduction of the internal stratigraphic framework (azimuth and dip), 5) the incorporation of the detailed petrophysical data coming from probe permeameter and surface mapping of deformation facies, 6) the population of the core volume using diverse geostatistical techniques, and 7) the upscale process to a regular grid for simulation purposes.

5.1 Data Loading and Core Stratigraphic Grid Building

The first four steps mentioned above represent the required tasks to reproduce as closely as possible the internal layering and continuity of deformation sequences in the sample with the incorporation of all the valuable information for subsequent data analysis and population. From core surface mapping, a practical determination of major control geometries and boundaries were recognized, their spatial position carefully calculated and exported as control points to the modeling software (GOCAD[®]). At the same time, all the available voxet images from CT scanning were digitally converted from a progressive gray color scale defined in the original captured images. Then, these images were translated in the tridimensional space defined in GOCAD, oriented and correctly positioned according to the correspondent vertical slice where it was captured (**Fig. 5.1a**).

[®] GOCAD Registered Modeling software – Earth Decision Sciences

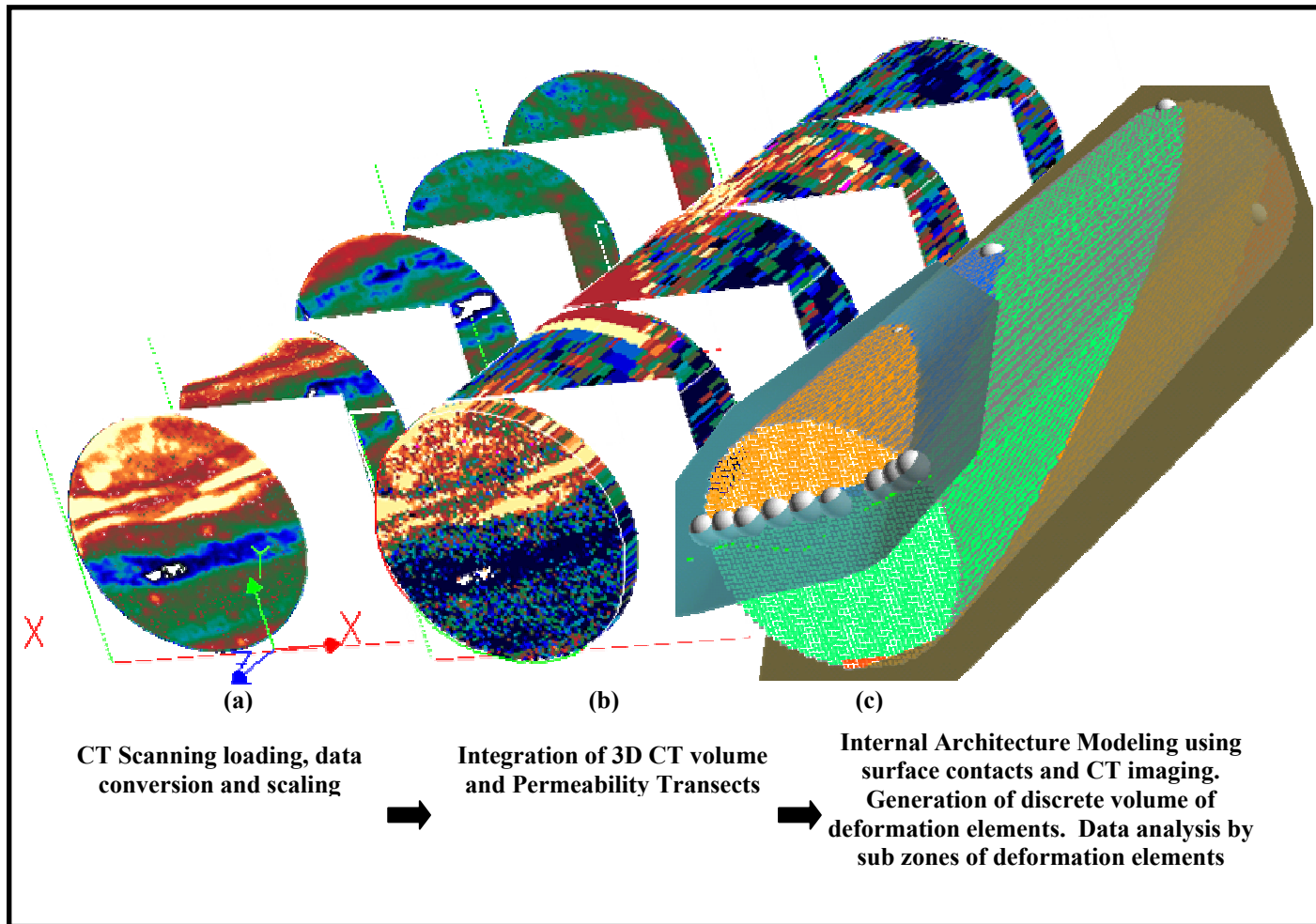


Fig. 5.1 – Modeling steps for shear zone 3-D characterization. (a) The first steps involve the CT scaling, conversion to ASCII format and loading. (b) Creation of the 3D Ct volume and integration with probe permeameter data. (c) Identification of bounding surfaces and contacts modeling a discrete volume of deformation elements for data analysis and population.

In order to have a complete tridimensional coverage of the CT value in the grid of interest, an additional low-resolution, regular grid was built. This grid consists of a core-long series of layers of 6 mm thick each one, and a 80 x 80 areal mesh. Each digital image was transported to the specific vertical location finally generating a tridimensional grid containing all the CT information for the sample. This CT volume was downscaled to our stratigraphic grid by direct property transportation to the nearest active cell (**Fig.5.1b**). The term downscaled is used here because the higher cell density in the stratigraphic model although the vertical resolution is kept similar, limited to the originally determined 6 mm window from CT scanning. The incorporation of this density information has allowed to analyze the continuity and distribution of deformation elements, identify the presence of joints or fractures, and visualize some density anomalies caused by heavy minerals, shale grains, and holes produced by diagenetic processes, etc.

All the control points from surface mapping joined to the information from CT volume were used to model the visible and totally extended throughout the core surfaces in each sample (**Fig. 5.1c**). According to the structural complexity, the stratigraphic grid volumes were modeled using cylindrical or prism shapes; prism geometries were used when truncated and non-parallel surfaces were present (i.e. NNR4_300 and NNR3_269 shear zones). With the information of internal layering from surface analysis and CT, each subgrid, the portion of the grid limited by well-defined bounding surfaces, was subdivided in a series of proportional (between top and bottom) layers of individual thickness of 4 mm approximately. After this definition, the stratigraphic grid is fully generated and ready for petrophysical and tomography data loading.

Fig. 5.1 shows the final integration of CT images for core NNR4_404 after data conversion to geo referenced values x, y, and z. Note the high areal resolution of this data compared with the fixed vertical resolution of 6mm (determined by the number of cuts and the width of the window of radiological imaging).

Next, the permeability values from probe tool are loaded as a continuous variable in a series of wells located in the correspondent transect position. Deformation property

is loaded as a discrete parameter in the stratigraphic grid. After loading the CT volume, discrete values of deformation elements, and probe permeability measurements, an exhaustive data analysis by facies was executed (see Chapter III) determining the degree of correlation between variables (permeability-CT#) to estimate internal distribution of properties. As it was stated before, the correlation between CT and permeability is fair to good in the undeformed rock facies, but it is null when cataclasis is present. This means that density (and porosity) is not a variable that helps in predicting permeability in the shear zone core but can be quite useful to predict permeability in the protolith. Nevertheless, CT imaging is important in determining the internal continuity of deformation elements, their degree of heterogeneity, and the control of facies contacts in a tridimensional fashion.

5.2 Permeability Modeling

A first step in the petrophysical modeling procedure after grid generation and data loading consists in the determination of the degree of dissimilarity of permeability with distance, using the variogram estimation. Unfortunately the areal or strike anisotropy of the shear zone cannot be measured with the data and sample available although we could expect higher range of correlation than the distance from opposite sides of the core sample. The variability observed in the vertical direction and modeled with the variogram in such direction was also considered for the areal component although their magnitude for the range was increased to guarantee correlation beyond the size of the sample (**Fig.5.2**). In general, the variogram was modeled using the internal structure and the transformation of the input permeability data using logarithmic and normal score transformations. The ellipsoid of anisotropy was modeled using same values for the range in the X and Y directions, generally between 5.5 and 12.8 cms, and range values in the Z direction clearly depending on the thickness of the deformation elements. These values ranged between 1.5 and 4.7 cm.

Regardless of this general assumption in the lateral range of correlation, considered based on the lateral continuity of deformation elements in the dip direction

and the layered structure of the shear zone, the vertical variogram has very important information near the origin that will have highest influence in the results for kriging and simulation runs.

In the case where samples could be totally or partially modeled with a discrete population of deformation elements, variogram estimation and modeling was executed independently by facies. Although no difference was noticed in the range of correlation between facies in the areal direction due to reasons already explained, the degree of correlation in the vertical direction tends to increase with an increase in the degree of deformation when the deformation elements are quite thick to give enough information about their permeability field not being totally influenced by thickness. This suggests that we could expect a general trend in correlation according to deformation. As the rock suffers moderate degree of deformation (to moderate deformed facies) petrophysical anisotropy can rise showing low correlation lengths, but with additional deformation and transforming those rocks to a highly deformed elements, those elements are petrophysically homogenized exhibiting low heterogeneity. This observation clearly agrees with the low standard deviation observed in the permeability density functions of the highly deformed elements.

Petrophysical properties were populated using: 1) Ordinary kriging, 2) kriging with external drift, and 3) Sequential Gaussian Simulation. Kriging, a basic and most widely used statistical technique, estimate a value at a point of a region for which the variogram is known, without prior knowledge about the mean. Additionally, ordinary kriging implicitly evaluates the mean in a moving region. In those locations where points, both known and to be estimated, are farther than the modeled variogram range, they are uncorrelated. In these particular locations kriging estimator becomes the arithmetic average, consistent with the notion that the arithmetic average is the best estimator of the mean for an uncorrelated data set.³² Ordinary Kriging algorithm provides a minimum error-variance estimate at any unsampled location giving smooth changes and concentrating the results around the expected value of the total measured locations.

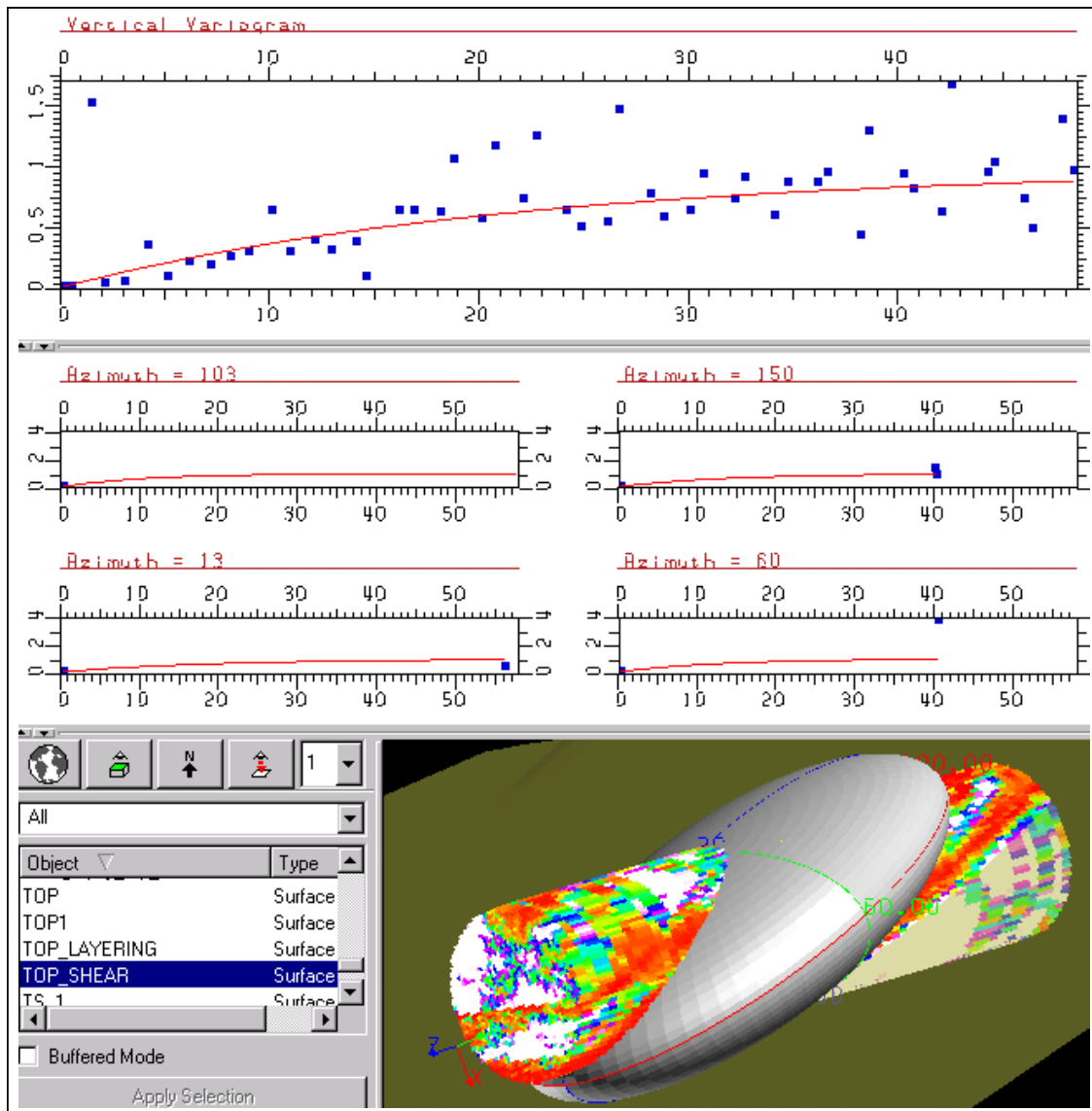


Fig. 5.2 – Variogram model showing the ellipsoid of anisotropy for core NNR3-269. Units in millimeters.

Bivariate geostatistical techniques considering an external variable (CT#) was used when the correlation between both variables was statistically significant and density derived from CT was giving some information about the areal distribution of the permeability field. This modeling technique is of particular importance when it is desirable to avoid the use of cokriging due to its additional complexity in modeling the cross-variograms. That is the case considered in cores NNR3_269 and NNR4_300 (**Fig. 3.11**) where Kriging with External Drift was additionally used. This kind of kriging estimate uses a trend that is a linear function of a secondary property (drift) that needs not be in the units of the data (CT#). That means that the dependence of the primary variable (permeability) on the secondary variable (CT#) is merely deterministic.

Additionally, multiple realizations of conditional simulations were run using a sequential gaussian simulation procedure that uses the kriging mean variance for generating a gaussian field.³² Each variable is simulated sequentially according to its normal CCDF (locally conditioned cumulative distribution function). The conditioning data consists of all original data and all earlier simulated values found within a vicinity of the location to be simulated. The locations to be simulated are randomly picked and the generated output value is influenced by neighboring, original data values (obtained by direct sampling) and by neighboring, already-generated values. The simulation process is constrained by the probability distribution function (PDF) describing the original data values in such a way that each simulation will match to the original distribution function. This technique assumes the original distribution function to be unbiased and representative of the total field being modeled. Due to the fact that the CDF and PDF at all unsampled locations are influenced by its neighboring simulated values, the final simulation incorporates spatial continuity patterns inferred from the original data, defined with the variogram model.

For all this step of population, permeability modeling was executed under the logarithmic data transformation because this guarantees that the permeability field can be characterized by a gaussian field allowing to keep a simple model when single and

bivariate analysis is performed, and give us symmetrical probability density functions for kriging and simulation processes.

The final step comprises a scaling procedure that will transport the modeled and simulated values from the complex stratigraphic grids to a regular, orthogonal-cell simulation grid. This final, regular grid geometry (50x50 areal cell arrangement, and 4 mm thick layers) keeps internal structure geometrically simple avoiding irregular cell geometries and stratigraphic pinch outs (**Fig. 5.3**) and maintains orthogonality as an essential characteristic for solving differential flow equations with the greatest accuracy.

According to sample geometry, facies proportions and distribution, and original petrophysical characteristics measured with the probe permeameter, each model was independently evaluated comparing the input and output probability and cumulative distribution functions of the logarithmic transformation of the permeability field. Each model is also independently modeled and some important features that were considered in each specific case will be described next.

5.3 NNR4-404 Shear Zone

During modeling procedures kriging estimation and conditional simulations were executed for core NNR4-404 to be evaluated with numerical simulation. Shear zone at NNR4-404 and the sample selected for the present analysis shows a very distinctive geometrical and petrophysical contrast between the highly deformed elements and the protolith. The sample at this level exhibits a very consistent organization and layering produced by the high degree of cataclasis from relatively high displacement, creating very continuous bands of highly deformed elements. The limits of the tabular band of highly deformed elements and the lithologic contact of the shaly material were the control surfaces modeled determining layering orientation and dip (**Fig. 5.1c**).

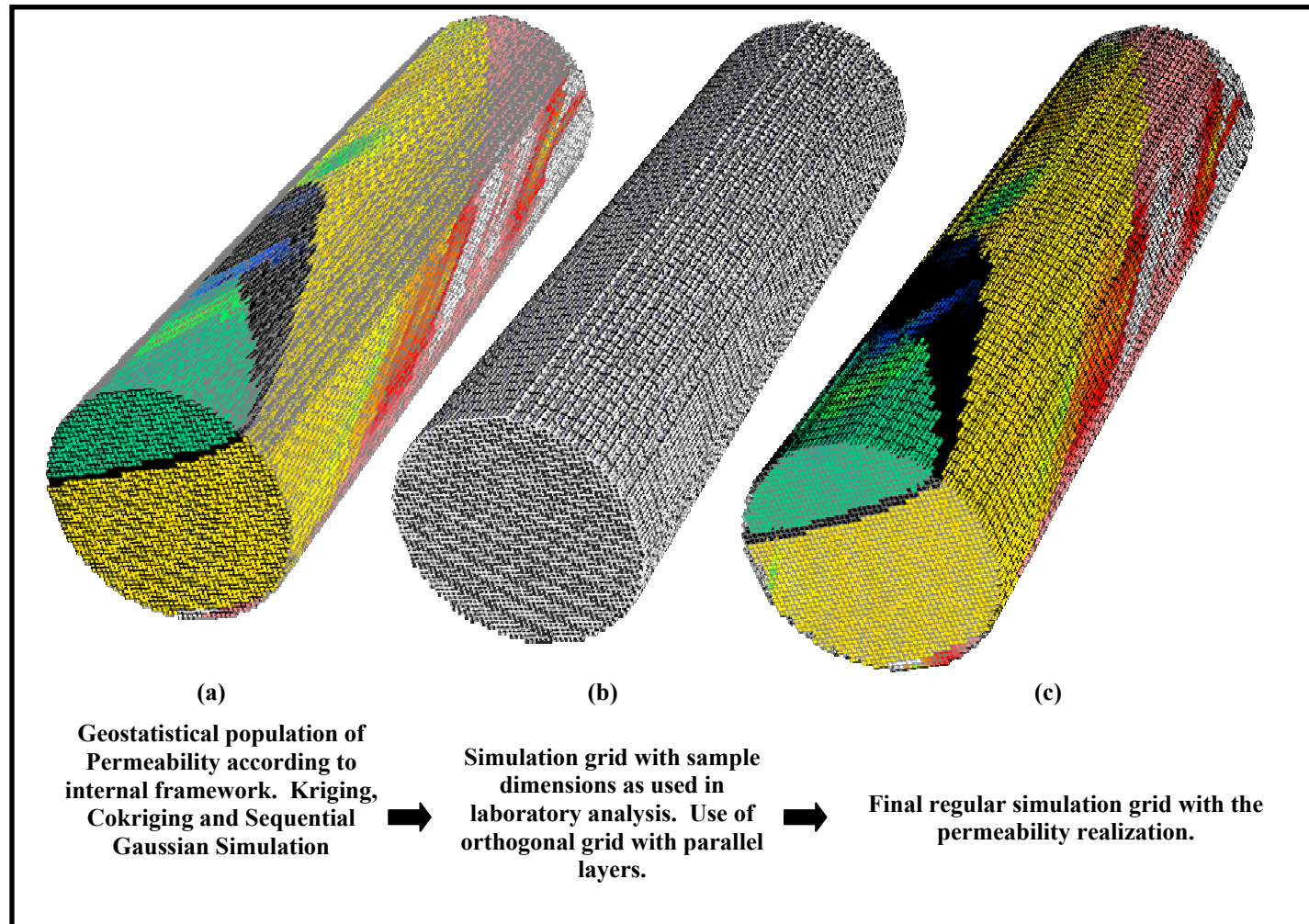


Fig. 5.3 – Scaling of geostatistical models for reproducing laboratory samples. (a) Geostatistical model of permeability. (b) Regular grid with parallel layers for simulation purposes. (c) Final volume of permeability for numerical simulation (kriging estimate for core NNR4-404).

This sample does not exhibit a clear layering pattern in the protolith above the highly deformed facies (**Fig. 3.3**), therefore for simplicity, and taking into account the low variability in permeability in this element, layering was maintained sub parallel to these control surfaces.

In general, log permeability data sampled at NNR4-404 exhibits a mean permeability of 0.41 with a standard deviation of 0.8438 for the whole population (**Fig. 5.4**). The output modeled grid using kriging estimates and the information about proportion of deformation elements exhibits an expected log-permeability value of 0.5713 and standard deviation of 0.7924. From this plot we can notice the bimodal distribution of the permeability field, the left hand side dominated by the high-deformed elements (sandstones and clay) that represent 49% of the core sample (see **Table 3.1**). The right hand side of the bimodal histogram is composed essentially by the moderate and relatively undeformed elements with permeabilities above 5 md. This sample from the highest throw interval shows a clear organization of facies in tabular bodies that were represented discretely in the model for having a close representation of the permeability assembly.

5.4 NNR5-291 Shear Zone (Upper Section)

The sample at NNR5-291 was modeled using two sub parallel surfaces located at the bottom of the core that represent the azimuth and dip of the main slip surface (see **Fig. 3.3**, highlighted contacts shown with green arrows). These bounding surfaces control the extension and geometry of the two main groups of deformation elements in this section of the shear zone although the discontinuity is more evident upward in the sequence.

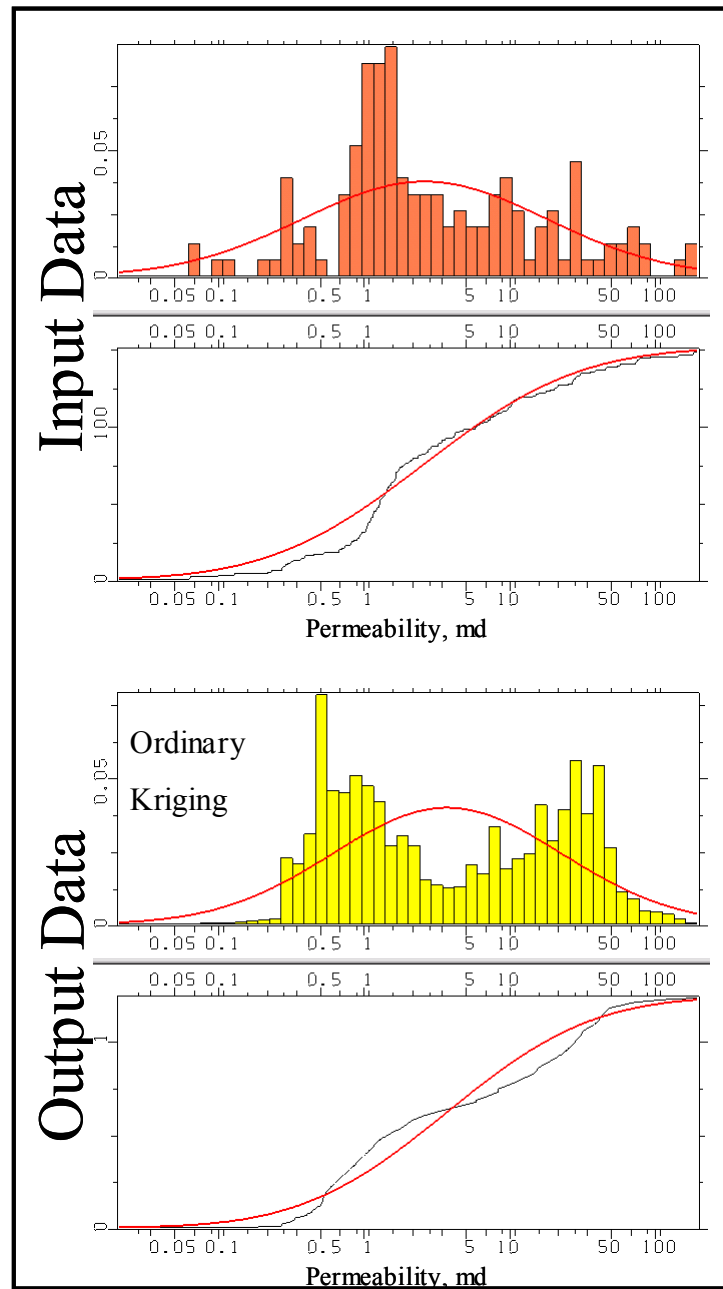


Fig. 5.4 – Comparison of Input and Output data for the kriging estimation of permeability in core NNR4-404

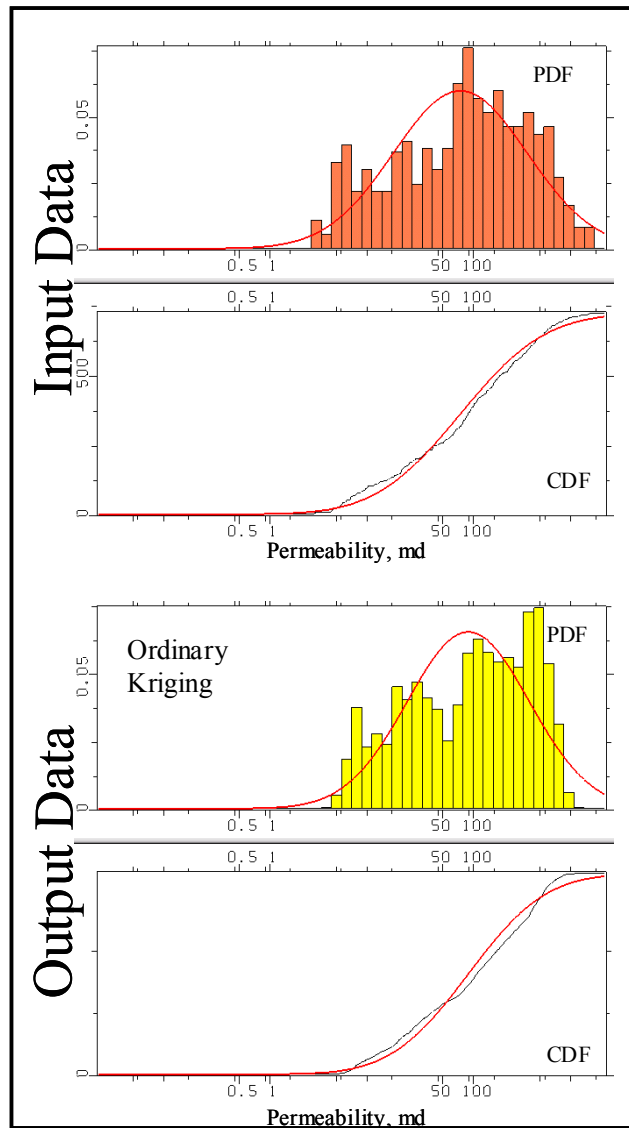


Fig. 5.5 – Comparison between input and output data for the kriging estimation of permeability in core NNR5-291.

The upper most surface is controlling the direction and dip of a series of highly discontinuous HDss elements (**Fig. 3.3**) with thickness between 3 and 5 mm, and the second located at bottom of the sampled section, that determines the correlation of HDss and MDss elements. In this sample, located in the upper section of the whole shear zone in the Hickory sandstone member, approximately 10 cm apart from the core fault zone,

is clearly visualized the change and variability in the degree of continuity of highly and moderate deformed elements depending the distance core shear zone.

Although the overall behavior of the log-permeability shows a more uniform distribution with a fairly acceptable gaussian distribution, detailed analysis of the total probability density function shows the characteristic flow properties of the more than 3% of Highly deformed, relatively highly continuous deformation elements, located in the permeability spectrum around 7 md (left hand side of histogram, **Fig. 5.5**). Analysis of the logarithm of permeability for input data showed an expected value of 1.8768 with a relatively very low standard deviation of 0.6613. A model using Kriging algorithms estimates very close this behavior with mean permeability of 1.9557 and standard deviation of 0.6028.

Typical Sequential Gaussian Simulation realizations exhibited expected (mean) log permeability values of 1.8768 md and standard deviation of 0.73, reproducing more closely the whole variability of the input parameter (**Fig. 5.6**). Nevertheless, the impossibility of creating a prior discrete volume of deformation elements to control the distribution of the thin and highly discontinuous HDss elements at the upper section of sample can result in the sub estimation of the potential of HDss as flow barriers because their continuity has not been adequately considered. For these cases, primary models using indicator kriging or object based modeling could help to integrate and consider the effect of very small features in the overall permeability field.

In general, the two shear zones from high displacement fault intervals exhibited a remarkable degree of layering and internal organization due to the high degree of cataclasis experienced. This observation agrees well with Ibañez analysis for the continuity of deformation elements of the 28 samples from the same fault zone.²⁵

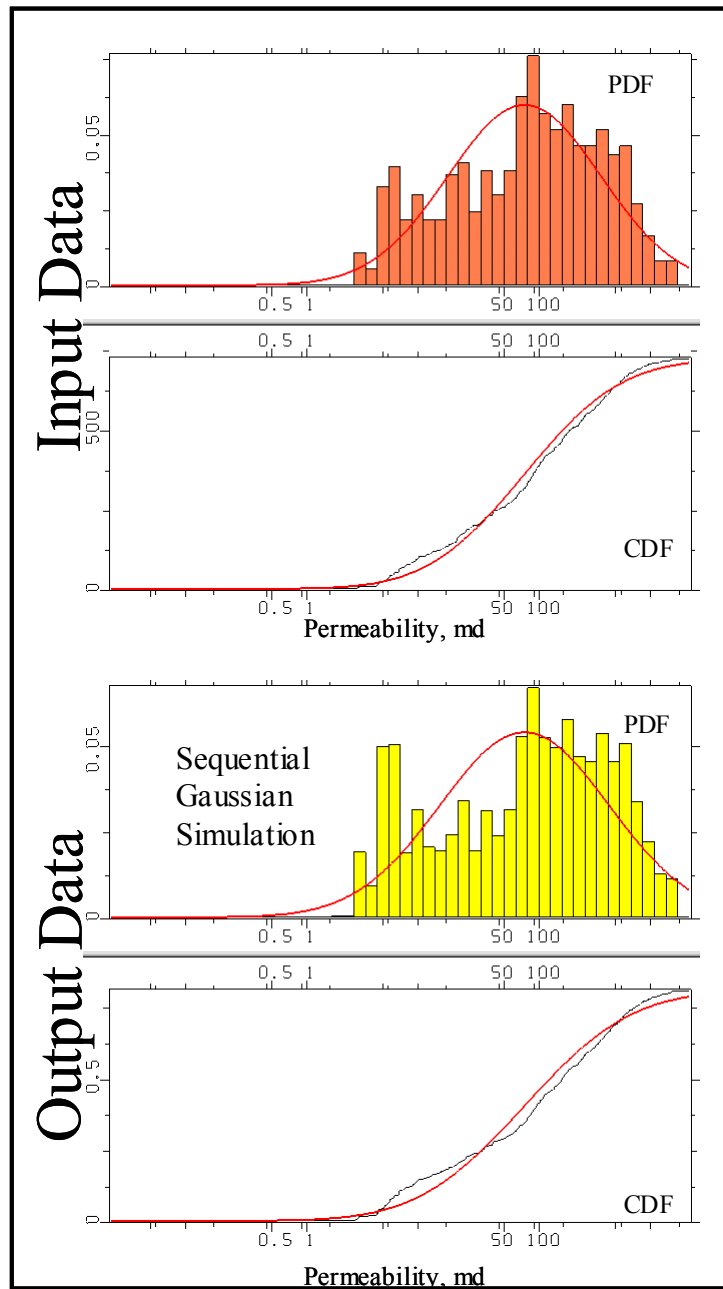


Fig. 5.6 – Comparison between input and output data for one Sequential Gaussian Simulation realization of permeability in core NNR5-291.

5.5 NNR4-300 Shear Zone

The low throw fault shear zone samples exhibited thinner and more discontinuous bands of deformation elements. This caused some difficulties in modeling because we were unable to strictly reproduce the presence and discontinuity of certain deformation elements. Despite the high heterogeneity shown, this sample was modeled using a near parallel layering to conform to the thin, discontinuous bands of highly deformed elements present in the middle part of the sequence (**Fig. 3.5**). Although the sample exhibits high heterogeneity, a higher correlation length can be expected in that direction of extension of the deformation elements, corresponding to a dip azimuth of 67° SE.^{25,26}

From histogram analysis of the obtained data, the whole NNR4-300 sample exhibits an expected log-permeability of 1.6986 and a standard deviation of 0.6622 (**Fig. 5.7**). When applying an ordinary kriging estimate, average (mean) logarithmic permeability was 1.763 and standard deviation of 0.4315. Information from CT imaging was incorporated in the geostatistical population using kriging with external drift, considering a trend as a linear function of this secondary property (drift) and supported by the acceptable correlation exhibited in the analysis for the low fault-throw samples. This algorithm and procedure will allow to evaluate the practical aggregated value of tomography in the characterization of the shear zones. Kriging with external drift estimated a mean log-permeability of 1.8096 with a standard deviation of 0.4728. From sequential gaussian simulation techniques, at right hand side of **Fig. 5.7**, without discrete (facies) conditioning, the output statistics were satisfactorily accomplished with a mean permeability of 1.69103 and a standard deviation of 0.6282.

Kriging estimates and Conditional simulation realizations were executed in the modeling step with the objective to match the laboratory measurements and additionally have an idea about the petrophysical continuity of deformation elements based on overall agreement with subsequent laboratory matching. **Fig. 5.8** presents the display the two different kriging models (with and without drift) and three selected conditional simulations with the correspondent permeability histogram. Kriging models show more

petrophysical continuity inclusive when considering the external variable CT. Variogram ranges considered for these models in the areal (layering strike and perpendicular) direction are greater than core size, assumption that suggests that permeability is in correlation at core scale. In the direction perpendicular to this plane, the range of correlation will be obviously controlled by the thickness of each deformation element.

5.6 NNR3-269 Shear Zone

The lowest throw sample, represented by the shear zone NNR3-269, presents a relatively continuous band of highly deformed elements with a high percentage of clay (18%).²⁵ This core was modeled with the bounding surfaces of the highly deformed facies (using surface mapping and CT scanning) as control of internal architecture in the well-defined and totally sampled, shear zone. The contact between protolith and the shear zone is unconformable with a very distinctive change in dip and azimuth. This feature required individual control surfaces to build the modeling grid for geostatistical population. For the shear zone, internal layering is created proportional to the top and bottom limits represented by the slip surfaces with an approximate dip of 69° (dip azimuth to the SE) whereas layering in the protolith was controlled by nearly horizontal surfaces. Similar to the steps developed during the modeling procedure for core NNR4_300, the CT# volume was also incorporated for analyzing the degree of correlation between density and permeability. Input data from probe measurements have a mean log-permeability of 1.4536 with a standard deviation of 0.8180 while the Kriging estimation concentrates the mean log-permeability value in 1.58065 and SD of 0.5523. If CT volume is considered using the kriging with external drift estimator, the mean log-permeability is concentrated around 1.6798 and SD of 0.6203. Although there is a small change in the mean estimation, kriging with external drift shows an improvement in the reproduction of the heterogeneity of the phenomena (histogram of log-permeability, **Fig. 5.9**). Using one of the randomly selected sequential gaussian simulations, the mean log-

permeability increase to around 1.7776 with a higher standard deviation of about 0.9776, but reproducing very closely the overall heterogeneity observed from input data.

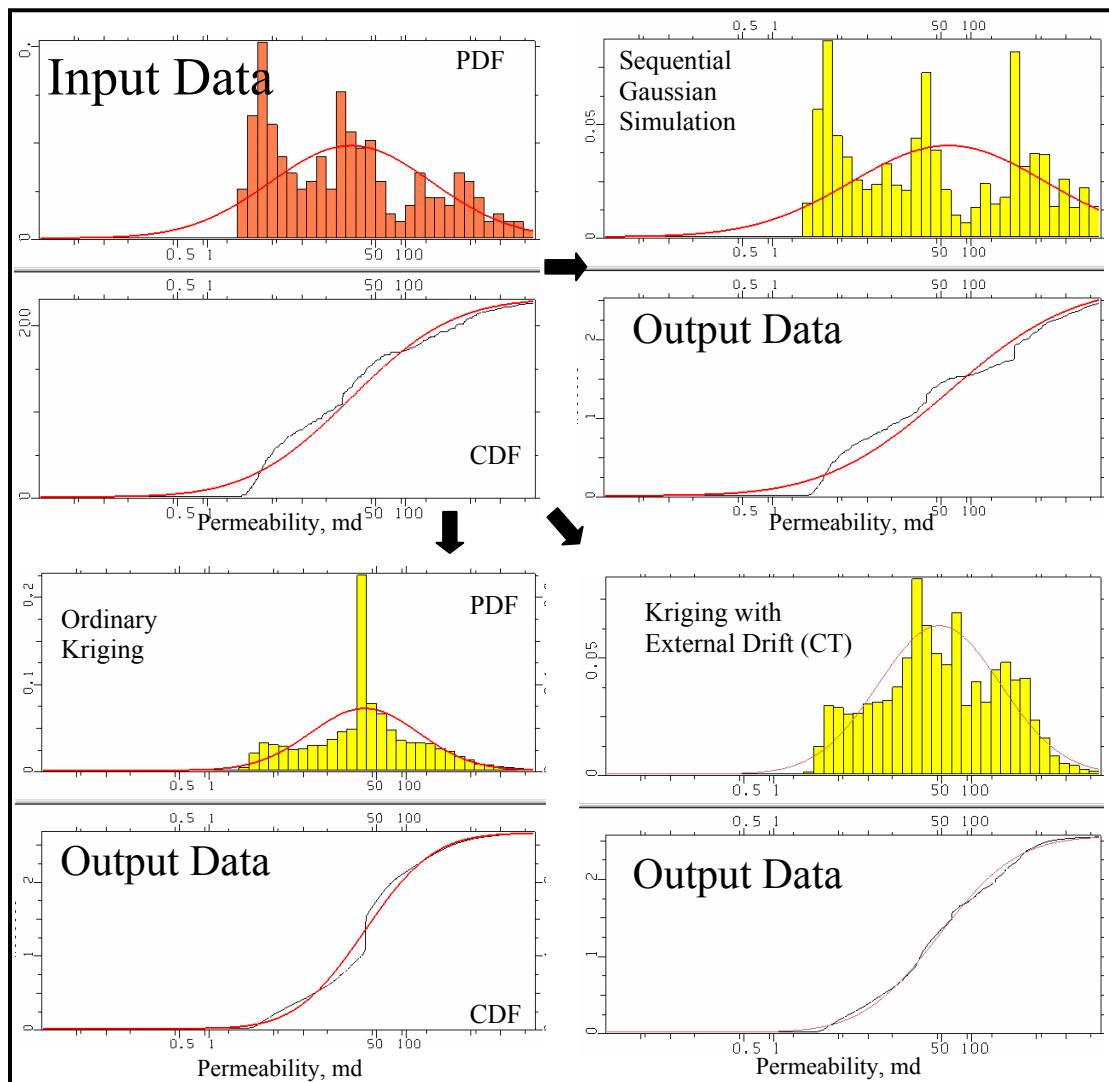


Fig. 5.7 – Comparison between input and output data for the kriging estimate, kriging with external drift and one realization of sequential gaussian simulation of permeability in core NNR4-300.

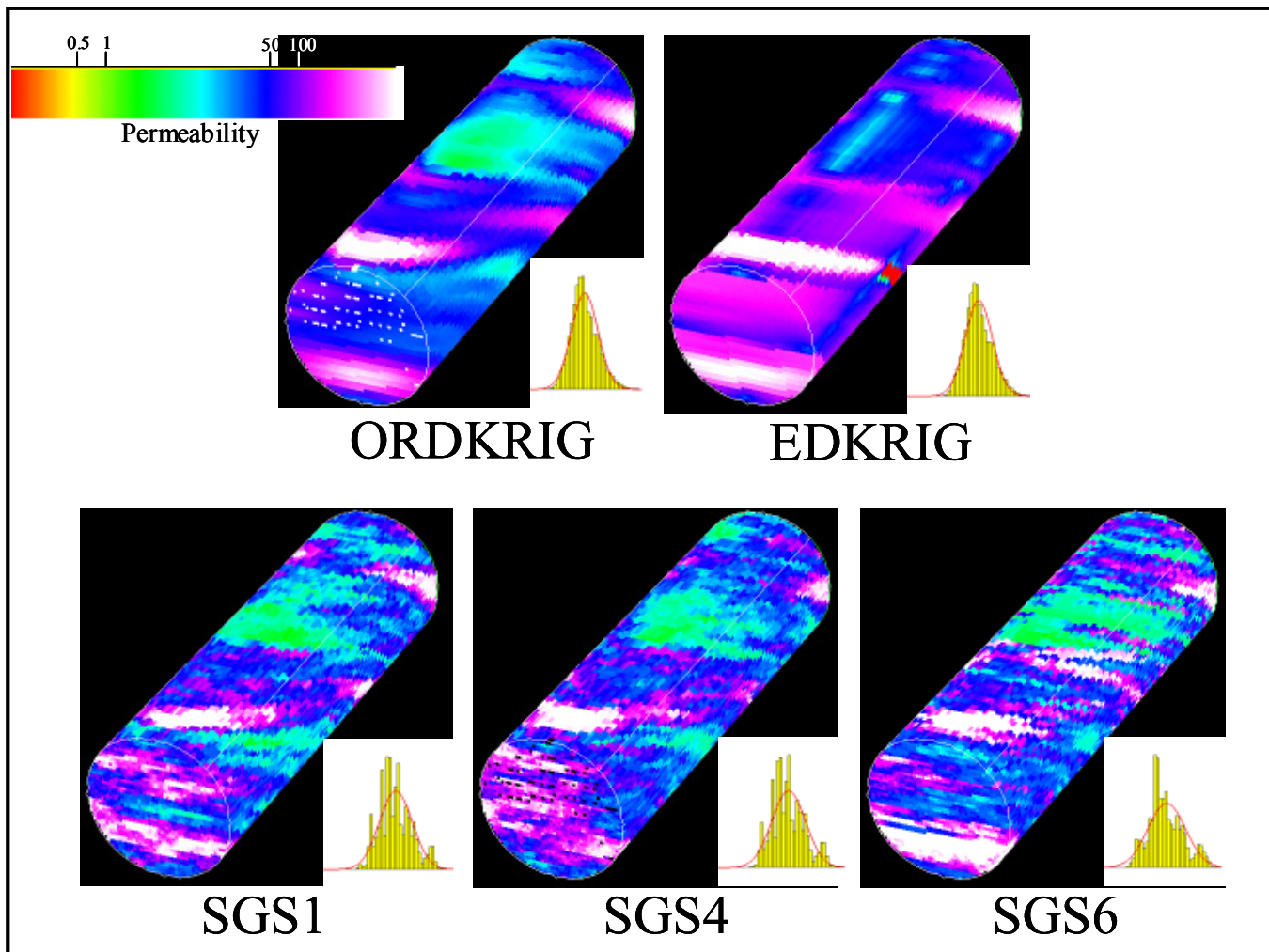


Fig. 5.8 - Kriging , Kriging with external drift, and three selected conditional simulation realizations for core NNR4-300.

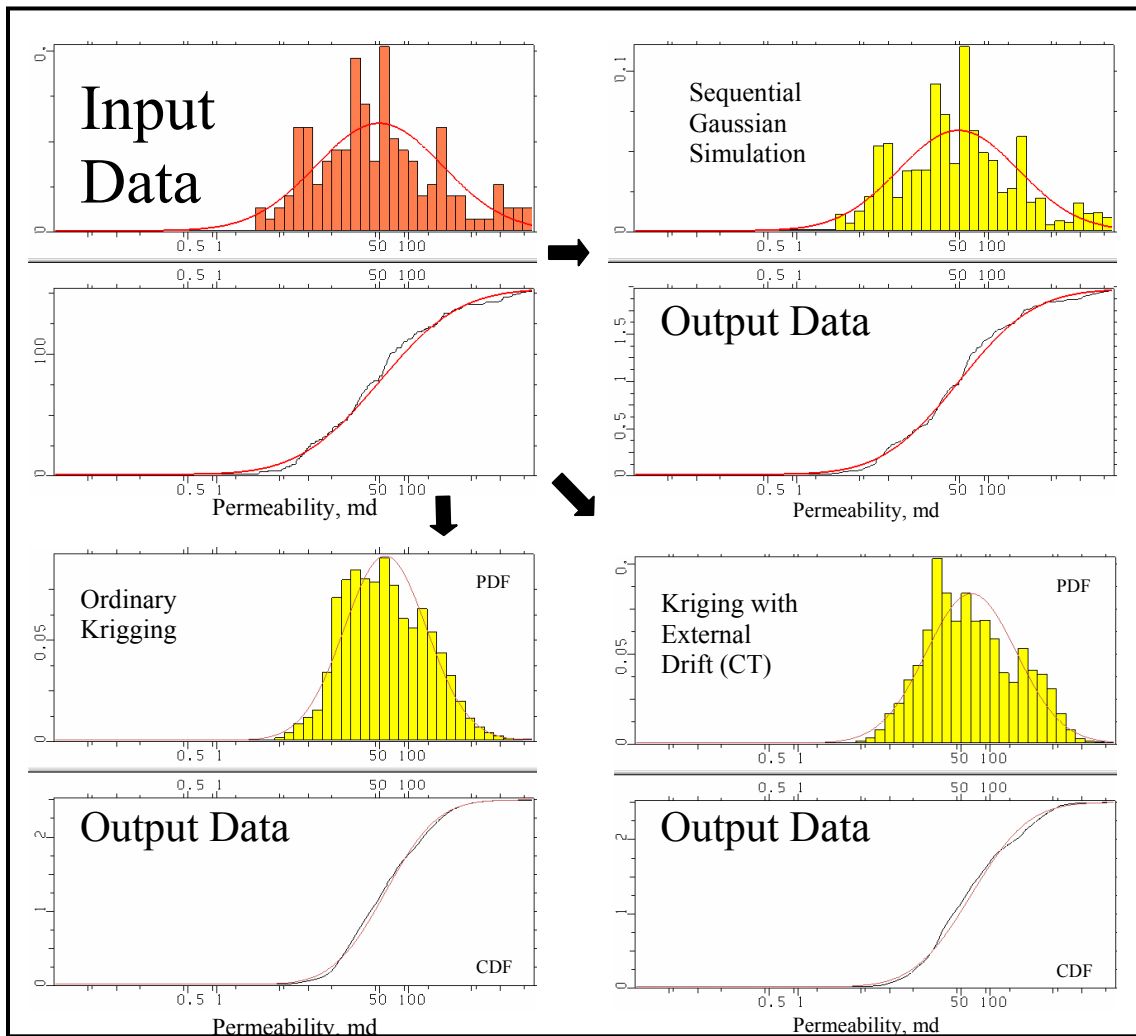


Fig. 5.9– Comparison between input and output data for the kriging estimate, kriging with external drift and one realization of sequential gaussian simulation of permeability in core NNR3-269.

Fig. 5.10 illustrates the main visual characteristics between the different algorithms used to model this core. As seen in core NNR4_300, kriging estimates enforce the lateral continuity of the low and high permeability elements producing a more homogeneous shear zone throughout the sample.

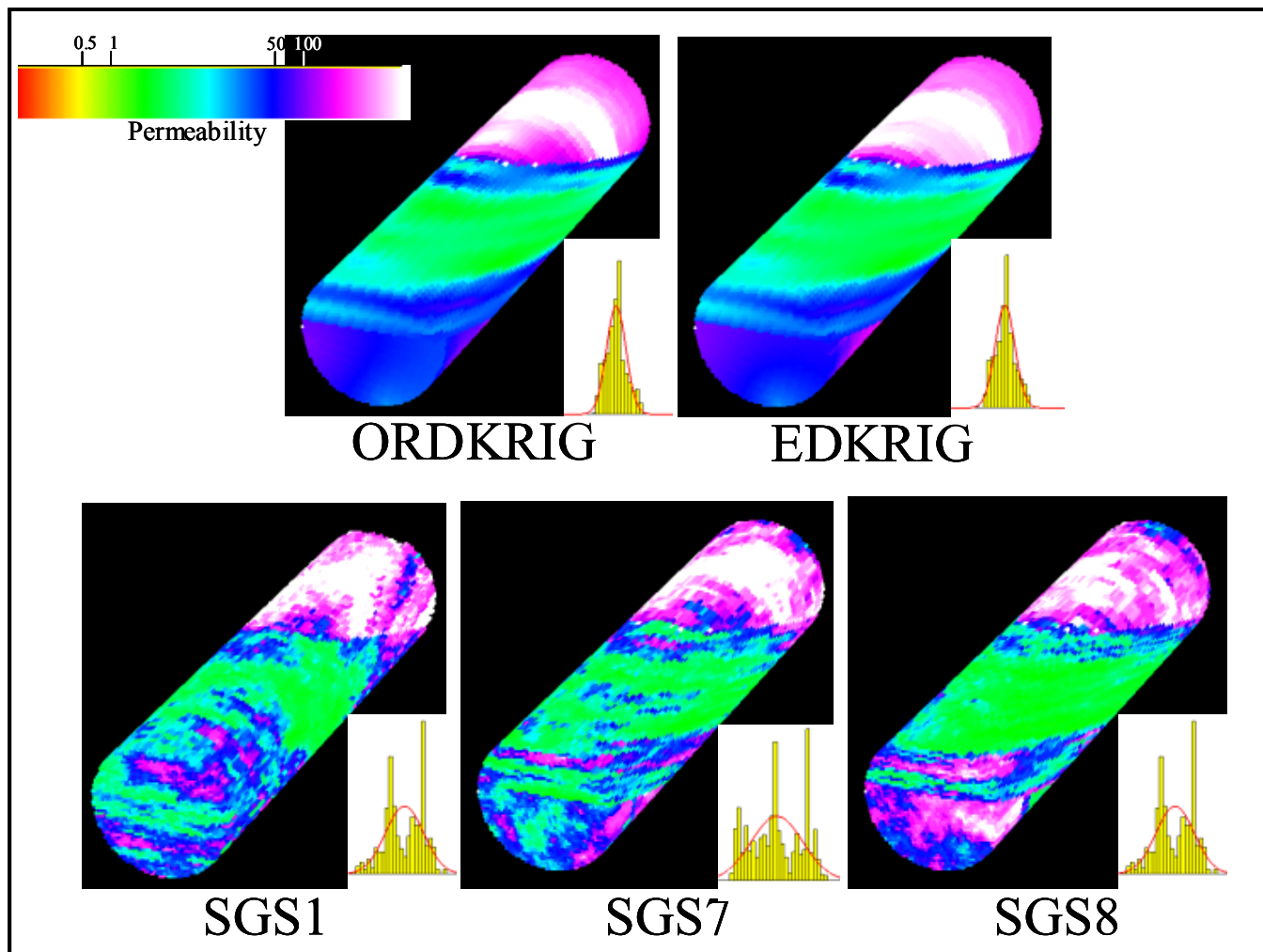


Fig. 5.10 - Kriging , Kriging with external drift, and three selected conditional simulation realizations for core NNR3-269.

CHAPTER VI

NUMERICAL SIMULATION AND LABORATORY MATCHING

6.1 Testing of the Numerical Model

Prior to estimating of the whole-core samples using flow simulation, several tests under known conditions were run to ensure the reliability of the numerical model.

6.1.1 Vertical Flow Test

For vertical permeability calculations, the grid configuration corresponds to an areal model of 50x50 cells with a detailed external cell inactivation to represent core geometry, and a parallel horizontal arrangement of 4 mm thick layers (60 layers), for a total cell count of 150000, 96000 activated to flow (**Fig. 6.1**). Cell size, approximately equals to 1.2 mm-side square in the areal direction and 4 mm in the vertical direction was chosen in order to incorporate practical resolution from CT scanning (already included in the modeling step) and vertical resolution from probe measurements, keeping cells as uniform as possible to improve accuracy. All models were injected in the first (top) layer in all the cells at a bottom hole pressure (BHP) of 14 atm. In the same manner, the last (bottom) layer was opened to production in each cell with the BHP set at 13 atm. The flow simulation at time steps of 0.01 hours was run until steady-state conditions were reached.

We began with homogeneous models of either 100 or 500 md permeability. The “isotropic” cases in **Table 6.1** show the results of calculated permeability from numerical simulation compared with the equivalent analytical solution using arithmetic and harmonic averages. The simulation results are within 1% of the known permeability. Heterogeneous, simple layered systems were also evaluated (**Fig. 6.1**), using layers of low permeability (1 md, and 10 md), vertically and horizontally distributed at middle part of the hypothetical core sample.

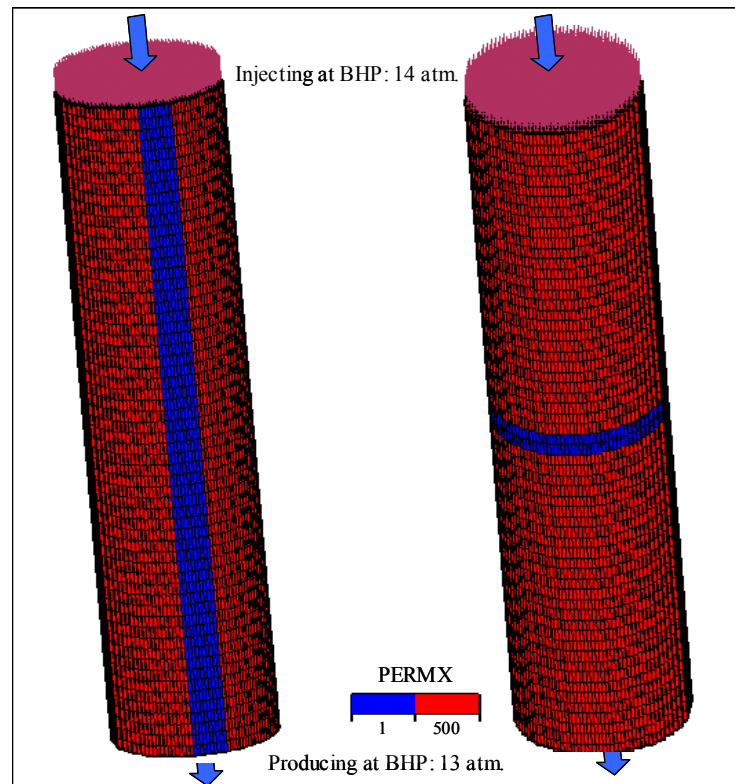


Fig. 6.1 - Vertical simulation models for numerical testing.

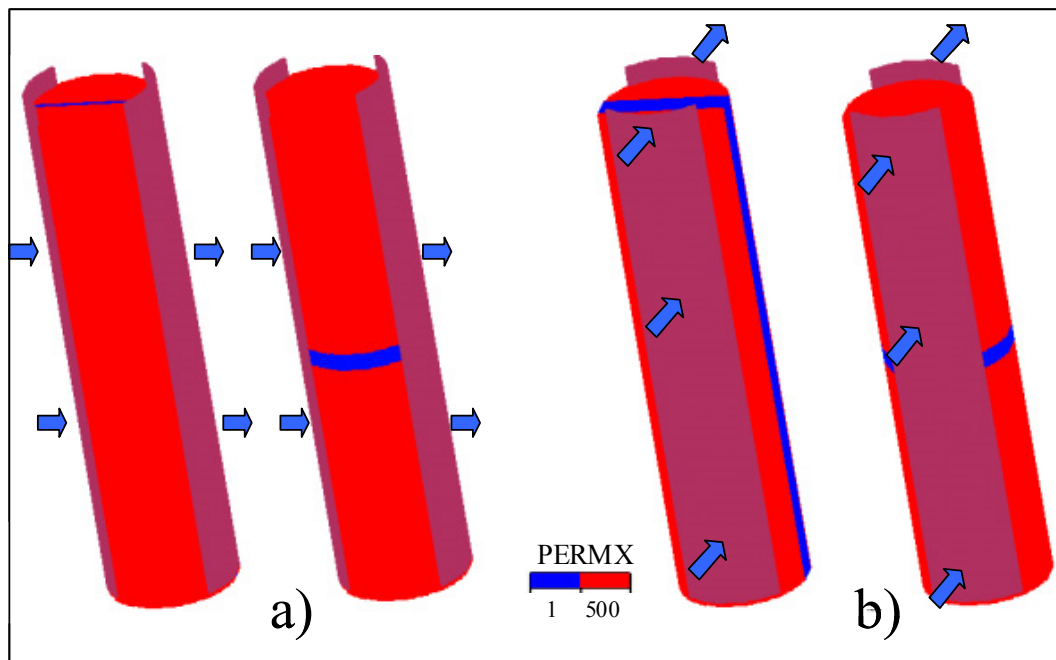


Fig. 6.2 - Along (a) and across (b) flow models for numerical testing.

6.1.2 Horizontal Flow Test

Along and across flow simulation performed over same grid configuration explained above for vertical flow test, was developed using injectors and producers located along the core where they were opened to flow in cells from the first to the last layer in each model (**Fig. 6.2**). The exact geometric configuration was used in the laboratory where whole-core permeability was estimated under air injection (see Whole-core Permeability measurements, in Chapter III).

According to that procedure and configuration used in the laboratory, the cores were flowed using the same angular opening of 90° . From experimental data available,⁴¹ this angular opening exhibits a geometric factor of 1 (**Fig. 3.13**), value that was used in the estimation of average permeability for all the cores (**Eq. 3.5**).

The same quality control developed for vertical flow simulation was done to check the error associated with grid geometry and any other problem besides permeability assignation. Simulation results in across and along directions are within 2% of the known permeability, showing a slight increase in error in this direction compared with vertical calculation (**Table 6.1**). The component of error associated to well index⁴² was found to be minimum as the bottom hole flowing pressure and the wellblock pressure were numerically equal.

Calibration tests were useful to determine the degree of confidence in posteriori estimations. The low difference between analytical estimations and simulation results gave plenty validity to the numerical technique to be evaluated. Nevertheless, the possible source of discrepancies can be explained by numerical precision in the permeability field during simulation, in the calculation of effective length and area for estimating average permeability, and the fact that we are not considering the complex geometry arrangement for the analytical technique estimation.

6.2 Numerical Simulation of Detailed Models

Each deterministic (Kriging estimations) and stochastic realization was evaluated using the ECLIPSE[®] simulator for a monophasic (water) system in laboratory units under injection and production conditions identical to those used for testing.

Comparing the lab whole core tests with simulation, the kriging estimates tend to give better agreement (**Fig. 6.3**). Although the number of stochastic realizations was limited, numerous realizations should reproduce the variability of plausible or equiprobable models in a range spreading from the kriging estimation. However, the fact that kriging estimates are satisfactorily reproducing laboratory measurements could be an indication of the low degree of heterogeneity in permeability of each deformation element.

It is important to analyze the simulation results depending on the flow direction. When considering the flow in the vertical direction, the samples with the highest fault throw and well-represented deformed elements exhibit a reasonable match with laboratory measurements (see samples at NNR4-404 and NNR5-291 in **Fig. 6.4**). In the highest throw sample (NNR4_404), errors are as low as 2.5% while in sample NNR5_291 the degree of disagreement is up to 56% for kriging estimates and up to 128% for one of the selected conditional simulations evaluated.

Error values tend to keep increasing with higher throw, varying from 109% up to 400%, with a slight improvement of matching using conditional simulation realizations. Compared to the laboratory values, higher permeability from numerical estimates is attributed to the low resolution of the probe permeameter. The permeability of the highly deformed elements in the samples with limited exposure and thickness was substantially over estimated and its effect in reducing permeability is greater compared to the results from probe permeability modeling. This observation agrees well with the results of the sensitivity analysis carried out with the evaluation of analytical solutions using power exponents, where a clear reduction of permeability of the highly deformed elements should be considered in order to match laboratory results (see section 4.2).

Table 6.1 – Test results for a cylindrical grid (50x50x60) before simulation runs.

FLOW	Real	Numerical Simulation					Analytical Solution		
	K	RUN	K, md	Qo(scc/hour)	Model	Grid Configuration	Arithmetic	Harmonic	Error Analy.-Num.
direction	md						$k_{av} = \sum(kih) / \sum hi$	$k_{av} = \sum hi / \sum(hi / ki)$	%
Across	100	Isotropic 1	100.704	8555.8	Isotropic	150000	100	100	0.70%
	500	Isotropic 10	503.520	42779.0	Isotropic	150000	500	500	0.70%
	100 & 1	Horizontally Layered	84.088	7144.1	10 hor. layers of 1md at center	62500*100 25000*1 62500*100	83.514		0.69%
	100&10	Horizontally Layered	85.598	7272.4	10 hor. layers of 10 md at center	62500*100 25000*10 62500*100	85.013		0.69%
	100 & 1	Vertically Layered*	4.698	399.2	10 ver. layers of 1 md at center	60(1000*100 500*1 1000*100)		4.616	1.79%
	100 & 1	Vertically Layered*	19.792	1681.6	2 ver. layers of 1 md at center	60(1200*100 100*1 1200*100)		19.483	1.59%
Along	100	Isotropic 11	100.704	8555.8	Isotropic 100 md	150000	100		0.70%
	500	Isotropic 12	503.519	42779.0	Isotropic 500 md	150000	500		0.70%
	100 & 1	Horizontally Layered	84.088	7144.1	10 hor. layers of 1md at center	62500*100 25000*1 62500*100	83.514		0.69%
	100&10	Horizontally Layered	85.598	7272.4	10 hor. layers of 10 md at center	62500*100 25000*10 62500*100	85.013		0.69%
	100 & 1	Vertically Layered*	79.020	6713.5	10 ver. layers of 1 md at center	60(1000*100 500*1 1000*100)	79.336		0.40%
	100 & 1	Vertically Layered*	96.403	8190.4	2 ver. layers of 1 md at center	60(1200*100 100*1 1200*100)	95.867		0.56%
Vertical	100	Isotropic	100.951	428.2	Isotropic 100 md	150000	100		0.95%
	500	Isotropic	504.757	2140.8	Isotropic 500 md	150000	500		0.95%
	100&1	Hor. Layered	5.679	24.1	10 hor. layers of 1md at center	62500*100 25000*1 62500*100		5.719	0.70%
	100&10	Hor. Layered	39.979	169.6	10 hor. layers of 10 md at center	62500*100 25000*10 62500*100		40.020	0.10%
	100&1	Hor. Layered	23.179	98.3	2 hor. layers of 1md at center	72500*100 5000*1 72500*100		23.257	0.34%

Time Step in simulation of 0.01 hours

$\Delta P = 1$ atm.

Area = 27.8 cm²

Length = 23.6 cm

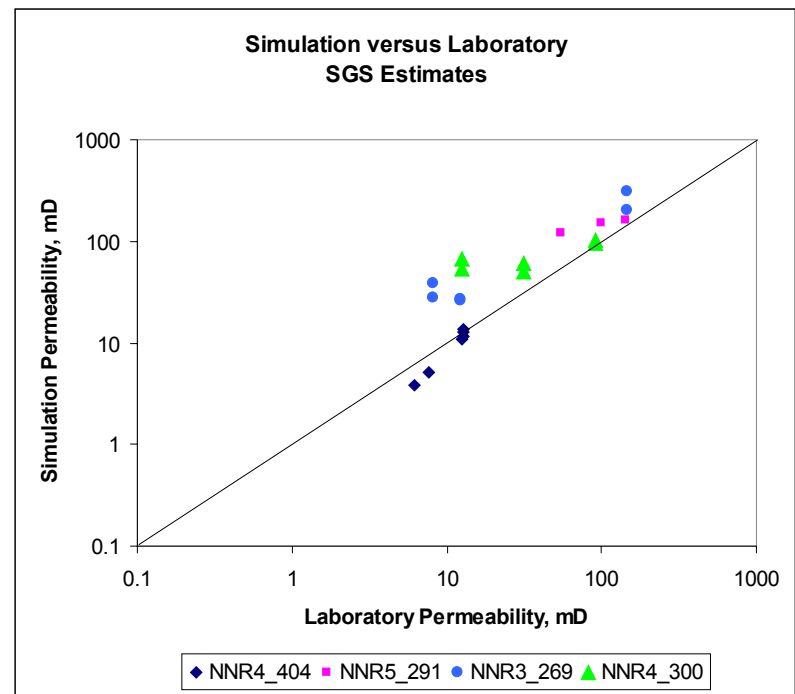
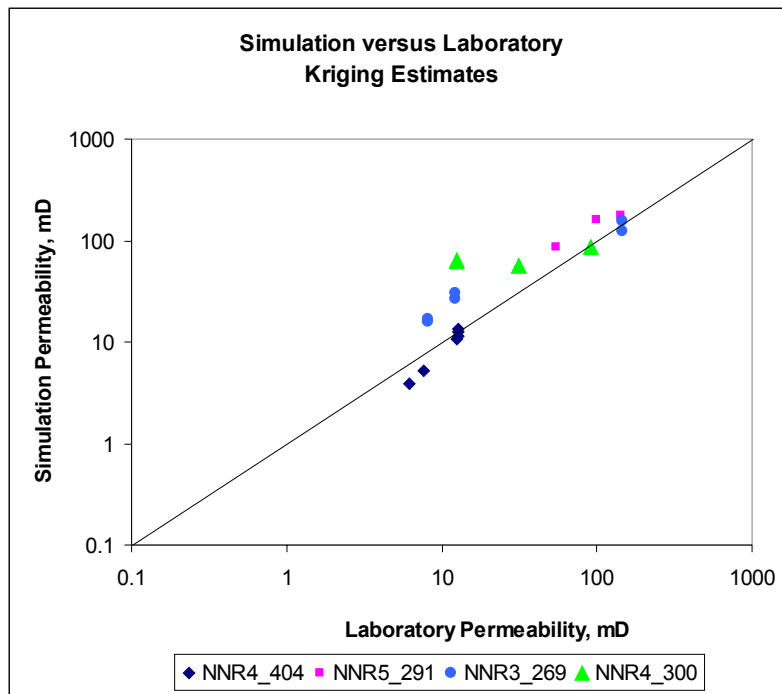


Fig. 6.3 – Numerical simulation results for deterministic (kriging and kriging with external drift) and two randomly selected conditional simulation models.

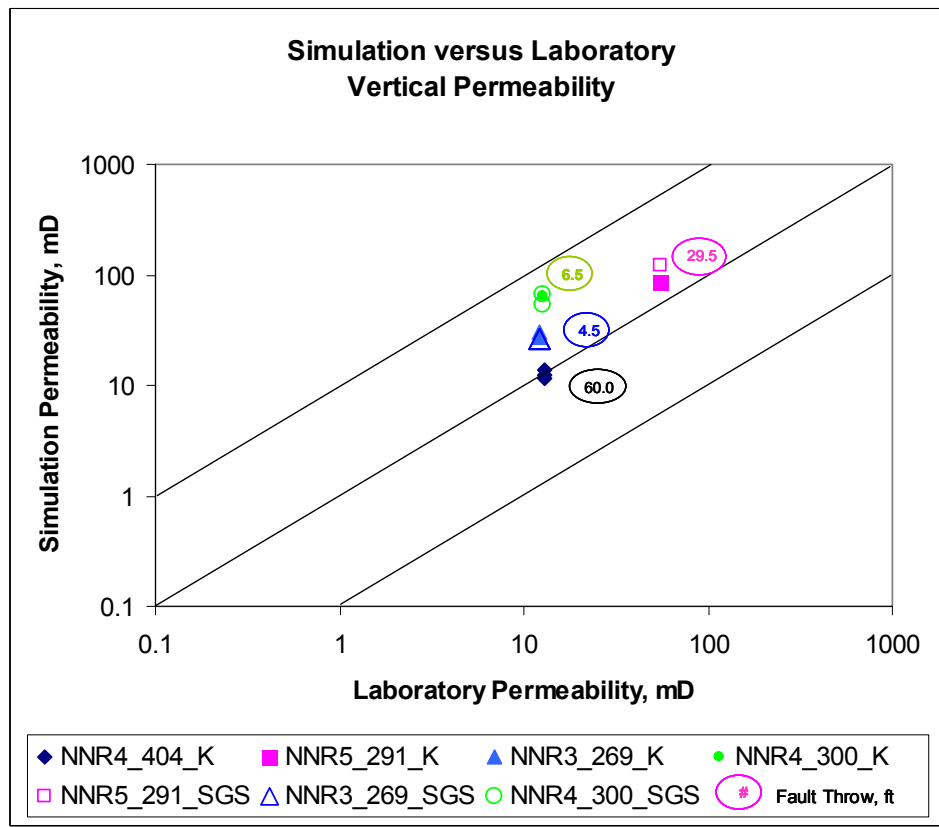


Fig. 6.4 – Simulation and laboratory measurements for vertical flow.

The across flow permeability estimates (**Fig. 6.5**) show a general agreement with laboratory measurements. There is a moderate over estimation of permeability that is also consistent with the problem in the definition of the flow characteristics of the small, highly deformed elements. The error in the simulated permeability is up to four times the laboratory calculation for selected sequential Gaussian simulations. Here again, kriging estimates have shown better agreement showing errors between 49 and 92%.

Finally, the along flow simulation results (**Fig. 6.6**) point out the low impact that the highly deformed elements have in the overall permeability in the along shear-zone direction, when they are thin and volumetrically insignificant, showing a very good match with the laboratory measurements for the whole-core sample. Errors in the

numerical estimation of permeability in this direction are ranging from 3.8 % and 37.8%, with the higher values for selected sequential gaussian simulation models.

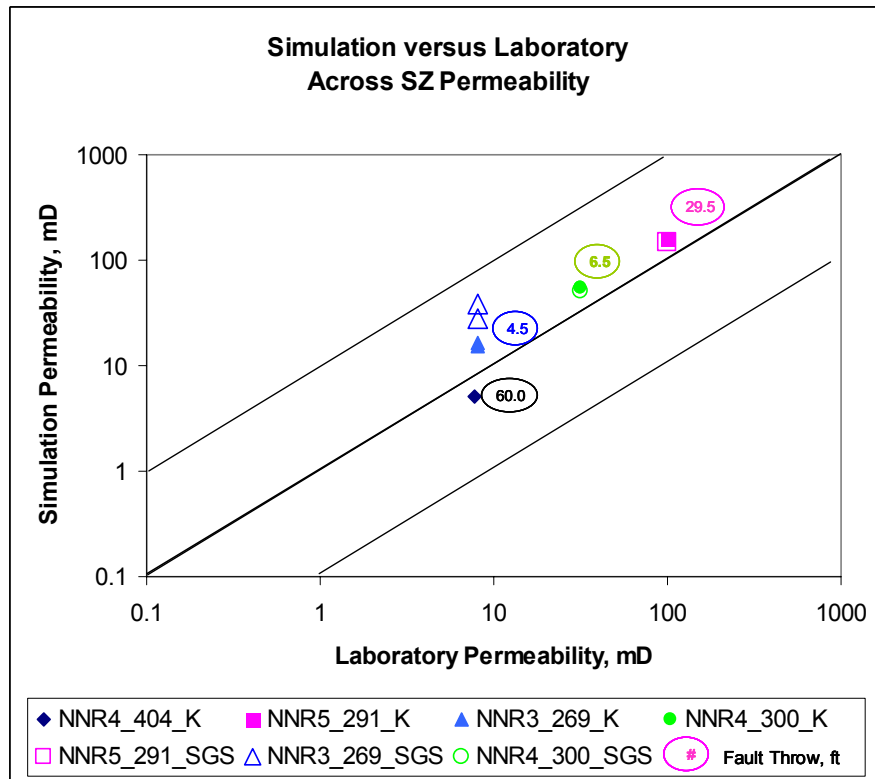


Fig. 6.5 – Simulation and laboratory measurements for across flow for kriging estimates and two conditional simulations.

In general, the agreement between numerical estimations and laboratory measurements is good. The largest mismatch was concentrated where there is insufficient exposure of surfaces of highly deformed elements that allow us to have a precise permeability measurement and characterization, causing in the present evaluation, an overestimation of the flow characteristics in the samples with low displacement and lower degree of cataclasis.

The static models evaluated under numerical simulation have demonstrated the high continuity of individual elements at least at core extension and the variogram used for modeling suggests that the anisotropy in the plane parallel to the internal layering is low. Perpendicular to this plane, the shear zone is highly layered in all the samples in analysis and the thickness of each deformation element and the whole shear zone is clearly controlled by fault displacement.

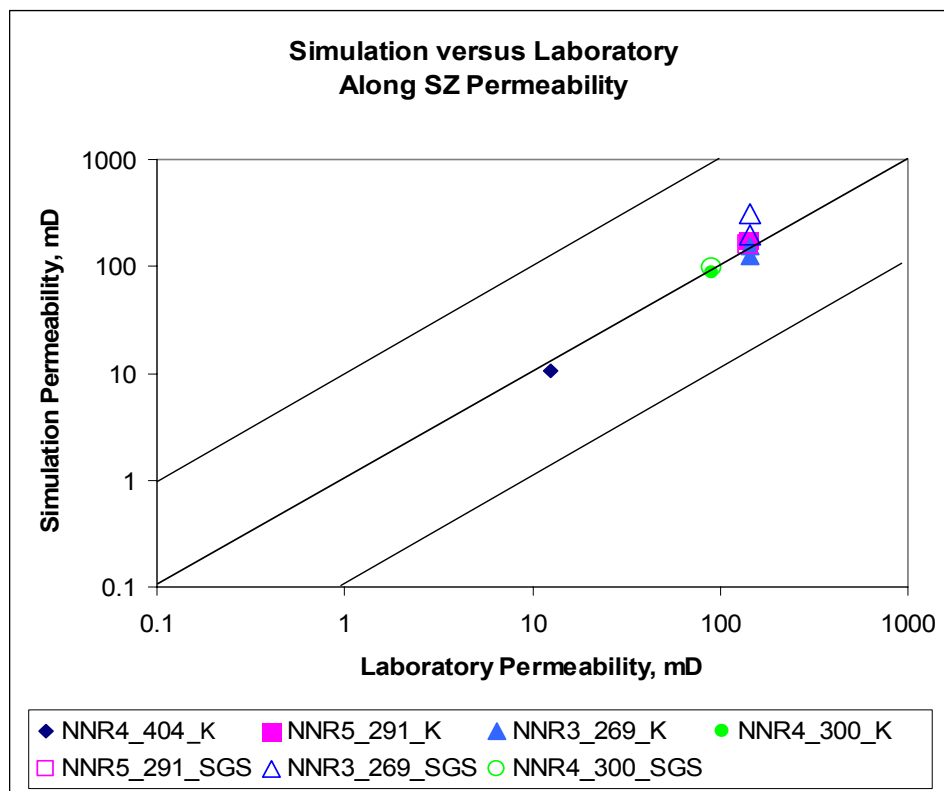


Fig. 6.6 – Simulation and laboratory measurements for along flow.

6.3 Numerical Analysis Incorporating Results from Sensitivity of Power Exponents

From previous analysis according to the use of power exponents it was demonstrated that highly deformed elements were possibly overestimated in permeability by a factor of 5 (section 4.2) in samples where those elements are narrow and below probe tip resolution. In order to test and quantify the effect of these important elements, an updated modeling step was performed, keeping same procedures in former models but reducing the permeability of highly deformed elements by a factor of 5. For sensitivity control, models using a reduction of half the value of permeability were also created. Kriging estimates were newly generated and exported to the simulator for fluid flow evaluation.

Modeling and fluid flow simulation results from core NNR3_269 and NNR5_291 (**Fig. 6.7** and **Fig. 6.8**) show very satisfactory match when the permeability was reduced by a factor of 5. Although in core NNR5_291 the original results were evaluated satisfactorily, this fine permeability tuning of the small volume of HDss facies gave a notorious improvement in the match between simulated and laboratory permeability.

For sample NNR4_300 (**Fig. 6.9**) a dual solution was executed in order to get numerical match between flow simulation and laboratory data. For this particular sample it was necessary to increase the volume of highly deformed elements in about 3.5% additionally with the proposed decrease in permeability for this facies. This effect is suggesting the presence of very thin bands of highly deformed elements that can be easily missed during the surface-mapping step. Many of small narrow features that were originally considered as moderate deformed elements might be highly deformed bands that are creating additional flow restrictions in the sample.

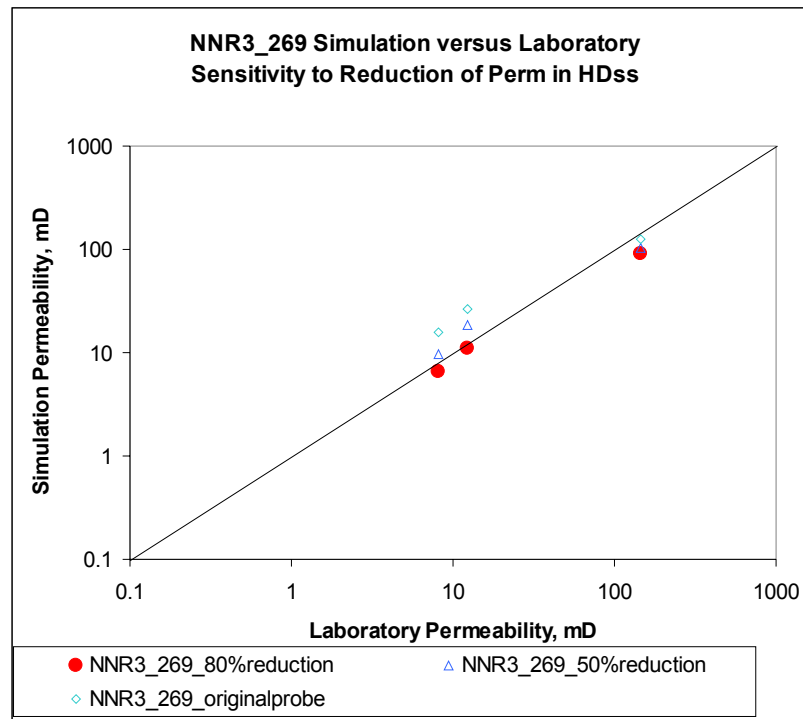


Fig. 6.7 – Results from reduction of permeability of HDss in core NNR3_269.

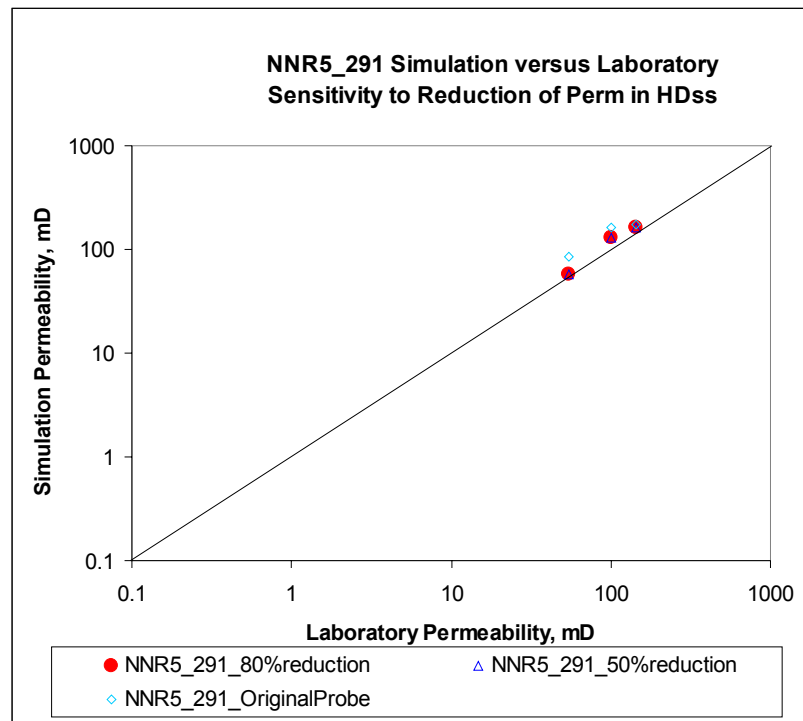


Fig. 6.8 – Results from reduction of permeability of HDss in core NNR5_291.

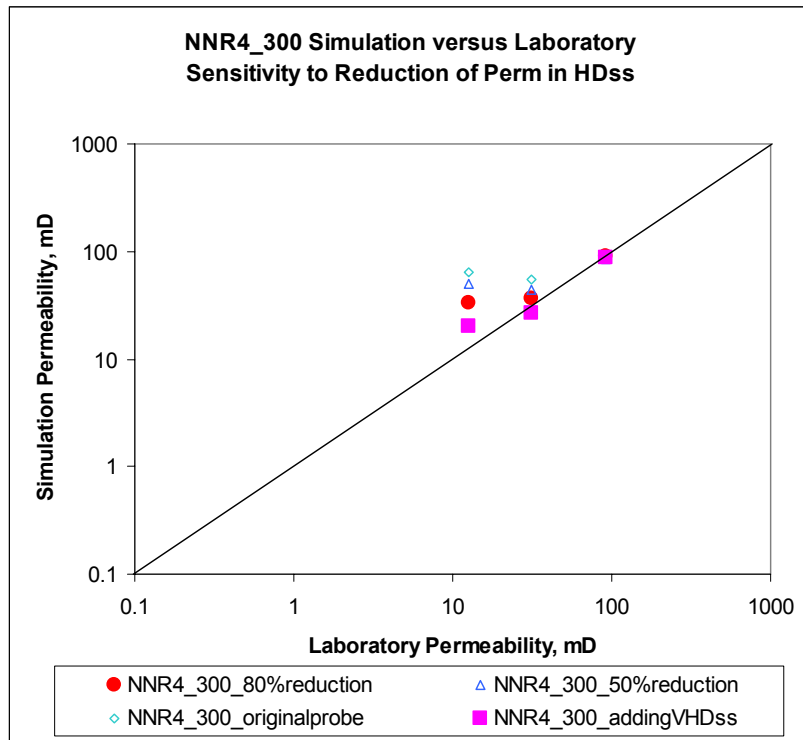


Fig. 6.9 – Results from reduction of permeability and increase in proportions of HDss in core NNR4_300.

6.4 The Internal Permeability Anisotropy of the Shear Zone as an Independent Body

Unfortunately there are not many available samples to evaluate shear zone permeability anisotropy as an independent unit (complete and continuous lithological record from top to bottom of the whole shear zone). Often, continuous core recovery is poor because cores may be broken. Nevertheless, core NNR3-269 contains a continuous and totally exposed shear zone that can be evaluated using numerical simulation and compared with future field test analysis. At the date of this investigation, no field-scale evaluation of this small faulted interval has been made but, Ibañez²⁵ has estimated this interval to have 3.2 md permeability with standard deviation of 0.3 md.

Using a new arrangement of injectors and producers to simulate flow from top of to bottom of the shear zone (along the slip surfaces) (**Fig. 6.10**), the numerical permeability estimate across the shear zone was calculated to be between 3.28 and 4.072 md, from kriging and five sequential gaussian realizations. The agreement with Ibañez's²⁵ estimate is good and particularly better for the model with lower anisotropy within the shear zone (kriging model).

Across shear zone, in this case corresponding to a direction parallel to the dip azimuth, permeability estimations from simulation runs exhibited a similar range of permeability (3.619 – 6.455 md) to those obtained for the vertical direction. Contrasting with these results, along shear zone permeabilities are between 9.24 and 32.14 md, values that represent the effect of the incorporation of moderate deformed elements within the shear zone, facies that is also continuous from inlet to outlet.

These results do not consider the proposed re-assignment of permeability for highly deformed elements as a result of the previously discussed low-resolution effect of probe measurements at front of narrow features. Considering that Ibañez analysis has similar resolution limitations, this comparison is still valid although the true shear zone permeability as an independent body has to consider the proposed reduction of permeability for the HDss facies.

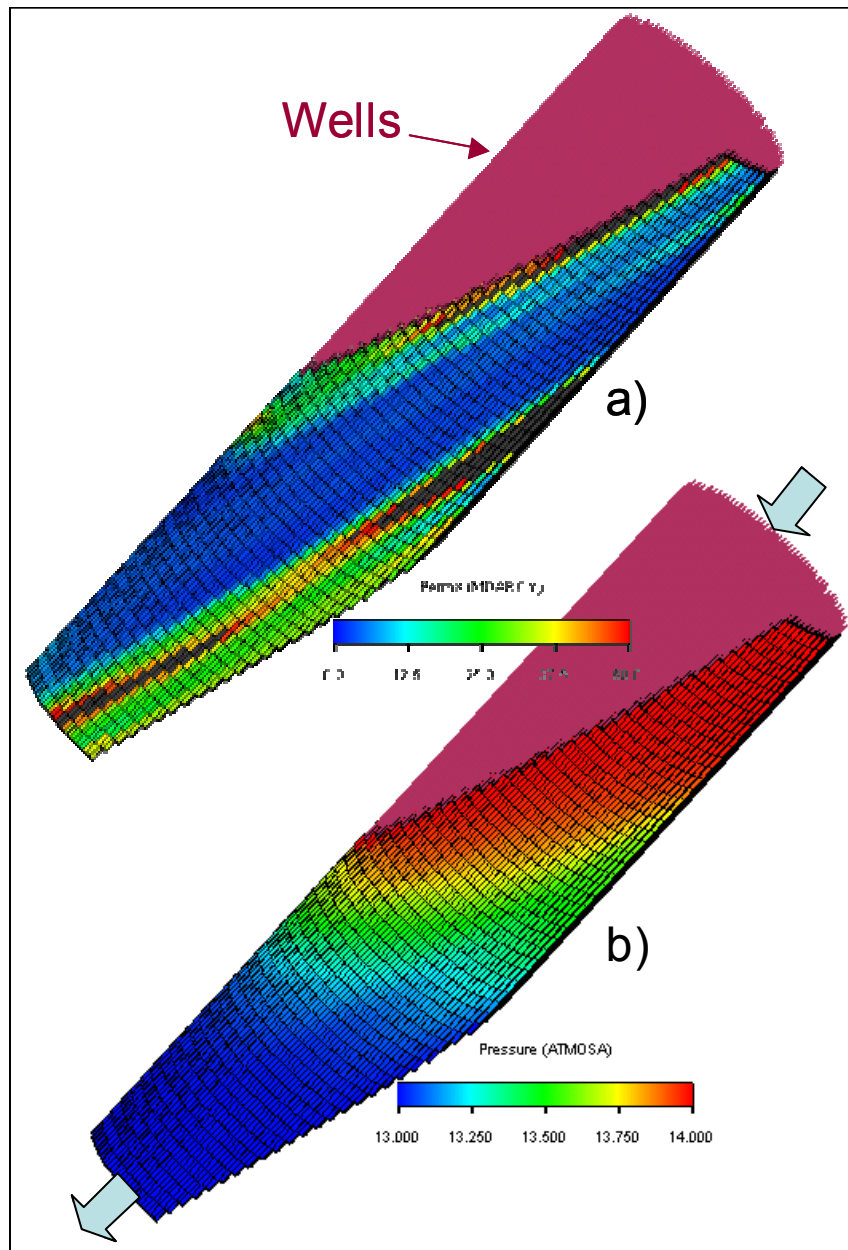


Fig. 6.10– Simulation of the independent shear zone unit in core NNR3-269. a) Permeability model. b) Pressure volume after two time steps for the vertical flow simulation.

From this sensitivity analysis, the whole shear zone exhibited values of vertical permeability between 1.136 and 1.41 md, across shear zone permeability between 1.867 and 3.33 md, and along shear zone permeability ranging from 5.86 to 20.38 md. The overall decrease of average permeability from models coming from original and re-evaluated data for the highly deformed elements is between 1.57 and 2.89 times, demonstrating the importance of an effective permeability characterization of the highly deformed elements as main controllers in shear zone fluid flow.

Core NNR4-300 can be also evaluated as a complete shear zone, although the whole shear interval is not totally recorded by the sample (see **Fig. 2-5**). The permeability estimate for this core sample is overestimating the real shear zone permeability because the presence of an additional part of this deformed material at the bottom of the sample should decrease overall permeability to the orders reported by Ibañez (6.2 md approximately).

Table 6.2 compiles the results from analytical solutions performed by Ibañez²⁵ and the results from this study for the two samples where the shear zone is nearly totally represented.

Combining the analytical estimates of shear zone permeability from Ibañez with the detailed characterization of selected samples from this study, we infer that the highly deformed elements have a large effect on the determination of the permeability across this physical boundary (**Fig. 6.11**). The relationship between HD element permeability for each particular location and the correspondent shear zone permeability has a significant trend or correlation that can be used to predict the flow behavior at different fault locations.

Table 6.2 – Comparison of shear zone permeabilities from Ibañez and results of the evaluation from the two low throw samples. Adapted from Ibañez²⁵.

Shear Zone	Strat. Throw	SZ Thickness	HD Thickness	MD Thickness	Ibanez Analytical Estimation of Permeability		Present Study SZ_Numerical Sim		
Hole-Depth	(ft)	(ft)	(ft)	(ft)	SZ-Perm	SD	Vertical	Across	Along
3-202	46.0	0.659	0.30	0.10	0.15	0.01			
3-231	8.0	0.305	0.06	0.10	2.2	0.4			
3-269	4.5	0.2	0.17	0.02	3.2	0.3	3.28-4.072 ^Φ 1.36-1.41 ^{ΦΦ}	3.619-6.455 ^Φ 1.867-3.33 ^{ΦΦ}	9.24-32.14 ^Φ 5.86-20.38 ^{ΦΦ}
4-201	1.0	0.072	0.00		7.9	0.7			
4-300	6.5	0.184	0.15	98.42	6.2	0.6	12.6**	31.4**	91.036**
4-404	60.0	0.853	0.35	0.14	0.3	0.03			
5-266*	2.0	0.131			2.9	0.03			
5-274*	3.0	0.24	0.24	0.00	1.2	0.02			
5-279*	1.0	0.089	0.06	0.03	4.5	0.13			
5-291*	29.5	0.696	0.23	0.19	1.7	0.11			
5-308*	24.0	0.42	0.24	0.14	1.8	0.08			
5-327*	1.0	0.154	0.03	0.13	2.6	0.1			
6-250*	5.0	0.325			2.2	0.03			
6-254*	46.0	0.518	0.23	0.15	1.6	0.1			
6-281*	1.5	0.148	0.10	0.04	2.8	0.17			
6-287*	1.5	0.203	0.11	0.06	1.9	0.19			
7-202	39.5	0.22	0.19	0.00	0.9				
7-237	15.0	0.285	0.07	0.03	1.2	0.17			
8-252	33.5	0.823	0.15	0.58	1.6	0.08			
8-287	16.5	0.456	0.12	0.15	2.3	0.15			
9-277	2.0	0.21	0.05	0.07	2.3	0.18			
9-315	16.5	0.262	0.10	0.07	5.2	0.85			
9-321	25.5	0.745	0.10	0.63	1.9	0.13			
10-283	3.0	0.364	0.05	0.22	2.2	0.31			
10-287	3.0	0.24	0.16	0.12	1.8	0.2			
10-339	19.0	0.768	0.17	0.52	2.1	0.16			
10-358	32.0	0.043	0.04	0.00	1.2	0.08			
10-360		0.315	0.17	0.11	1.9	0.09			
10-363		0.236	0.04	0.18	1.6	0.06			

* denotes faults with strike and dip measurements made directly on core, assuming a north-south strike of bedding.

** values from laboratory measurements

Φ permeability from numerical simulation of models from original data

ΦΦ proposed "true" permeability from sensitivity analysis

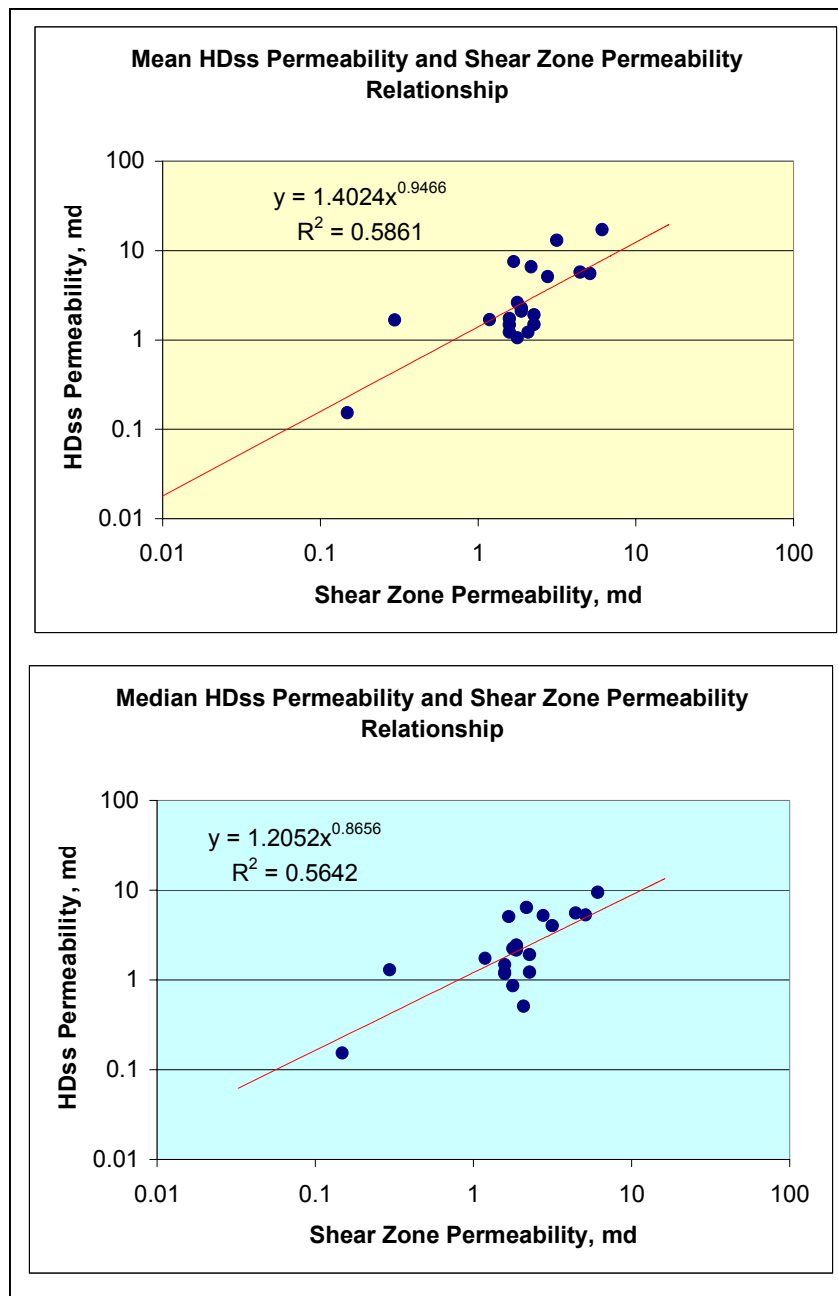


Fig. 6.11– Correlation between Mean and Median HDss permeability and total shear zone permeability. Input data from Ibañez²⁵, and present study.

It is interesting that the best linear fit is obtained at almost 45 degrees for both cases supporting the expected effect from these highly continuous elements throughout the core sample. Statistically, the use of mean or median permeability, as suggested by similar correlation functions and coefficients of determination, is irrelevant since the permeability of the highly deformed elements tend to be gaussian distributed. Besides highly deformed elements, shaliness and clay layers in the system also reduce the permeability and cause an overestimation of the total permeability if only the HD facies element permeability is used to predict overall behavior. This effect makes that the majority of control points fall above the 45° line.

We have demonstrated the importance of the petrophysical characteristics of highly deformed elements, their variability according to protolith characteristics and degree of cataclasis. These elements are geographically variable in terms of flow behavior and should be characterized in detail to be able to have estimations of total shear zone permeability for the determination of potential transmissibility between blocks in contact.

Next chapter will describe the proposed methodology based on the current findings and explains how the incorporation of probability functions according to specific correlations can help in creating models that accounts for variable petrophysical properties of shear zones. This procedure is the start point to develop systematic approaches for the incorporation of the inherent shear zone permeability anisotropy in full field models that allows explaining common drainage anomalies in sand-shale sequences at initial conditions and after dynamic changes in the reservoir.

CHAPTER VII

INTEGRATION OF HIGH DETAIL CHARACTERISTICS OF SUBSEISMIC FAULT SHEAR ZONES AT FIELD SCALE

7.1 The Permeability Scale Issue and Proposed Method

When dealing with impermeable or semi-permeable bundles or baffles, the permeability scale becomes critical if a detailed quantification of flow potential has to be addressed. For instance, if an infinite, continuous low permeability band (*i.e.* shear zone) is required to be incorporated in a detailed simulation model, many modeling techniques will group this narrow belt of deformed facies in a major volume of mixed lithologies with variable permeability quality. Traditional static modeling approaches consist in the representation of the fault geometry (strike, dip, throw) using very sophisticated grid assembly to represent the most closely possible the fault plane geometry and the calculated throw. Specific effort is typically done to accurately represent the connectivity along the fault plane but the consideration of the presence of deformed material along this plane is commonly not considered.

Many studies have been focused in the determination of the sealing character of large faults with enough throw and mixing lithologies to guarantee the presence of sufficient and well-continuous shale in the shear zone. As stated in Chapter I, sealing predictors based on shale content and fault displacements have been effectively tested in many areas, but the quantitative effect is still an issue of continuous research. It is also important this quantification when dealing with low throw (subseismic) faulting and in presence of shale-free formations, such the data set for the present investigation. Low throw faulting in single lithology formations is a common scenario in reservoir development and the effects of shear zone in flow behavior are always under investigation. The findings in this research about the degree of correlation between shear zone permeability and thickness and the characteristics of the host rock and the degree of displacement should be used to understand and predict the effects of these small barriers especially at mature production stages.

Faults represent specific locations where these small, continuous, and low permeability elements are present and their representation in simulation grids are being incorporated using transmissibility multipliers between adjacent cells. This approach suggests and clearly implies that the storage capacity of this narrow zone is minimal and all its importance is focused in the flow characteristics.

Simulation engineers do not commonly have additional studies that connect geological and petrophysical features and characteristics to find a tridirectional arrangement of permeability associated to fault corridors. For this reason, the faults sometimes are treated as discrete baffles that are used to adjust historic production or specific drainage anomalies, increasing or decreasing the conductivity through the blocks in order to improve the matching procedure. This task is subjectively done generally and it is not a result of detailed interpretation of the deformed elements within the shear zone.

We need to use geological information to guide the matching step in faulted blocks and be able to consider future drainage anomalies such as full or partial leaking or isolation with the dynamic changes of the reservoir. To obtain this understanding of flow behavior, transmissibility multipliers have to be geologically defined and be consistent with full field reservoir modeling.

There are currently two commercially available approaches (with software), Havana* and TransGen[™], that are focused in the sensitivity analysis of fault effects, based essentially in empirical functions of the throw of related faults and the shale gouge ratio^{43,44}. According to Manzocchi *et al.*⁴⁵, fine-scale numerical modeling indicates that variability in the fault zone permeability and thickness should be considered together, and that the best measure of flow through a fault is the arithmetic average of the permeability to thickness ratio. The TransGen⁴³ and Havana⁴⁴ software use the empirical prediction of median shear zone permeability and thickness from geometrical and petrophysical details of the reservoir model, as generally proposed by this current investigation. We propose with this research that the relationship between the host rock

* Norwegian Computer Centre. [™] trademark of Badley Technology Ltd.

and the degree of deformation, controlled by fault displacement, be considered as the main predictor of shear zone permeability when the reservoir has low shale content. Relationships found with the analysis of the Hickory Sandstone core intervals have given numerical estimates of shear zone permeability and thickness that will reduce the uncertainty in the determination of fault transmissibility and it could be used as analogous in similar areas under similar stratigraphic and structural setting.

The software tools available to calculate the transmissibility multipliers consider the input of a very detailed permeability and shale model to recalculate internally the shale-gouge-ratio and the incorporation of the fault throw and shear zone thickness to solve for the fault-zone permeability. The final step consists in the determination of transmissibility multipliers that will be exported for final simulation purposes (**Fig. 7.1**). The application of this method would require strict refinements of the methodology to account for some important geological factors such as: ⁴⁶

- the variability of rock permeability (in the shear zone and host rock) and thickness over short distances along the fault trace,
- the effect of errors in the definition of displacements
- the complexity of fault zone structure that sometimes increases the flow across faults are effects that vary from area to area and require detailed analysis of scaling of segmented faults and about the geometry of damaged zones³⁶
- the analysis of diagenetic effects, particularly those which are depth dependent.

This research proposes individual characterization of reservoir properties and geological attributes by reservoir, finding useful trends and correlations to reduce the uncertainty in the determination of shear zone permeability and thickness. As it was stated before, SGR is not an important variable in low shale-content formations and for this reason a more systematic approach considering the process of deformation should be incorporated. The rest of the process in modeling and final determination of transmissibility multipliers are kept as proposed by the commercially available tools, but the input of shear zone permeability has to be derived from structural-petrophysical correlations.

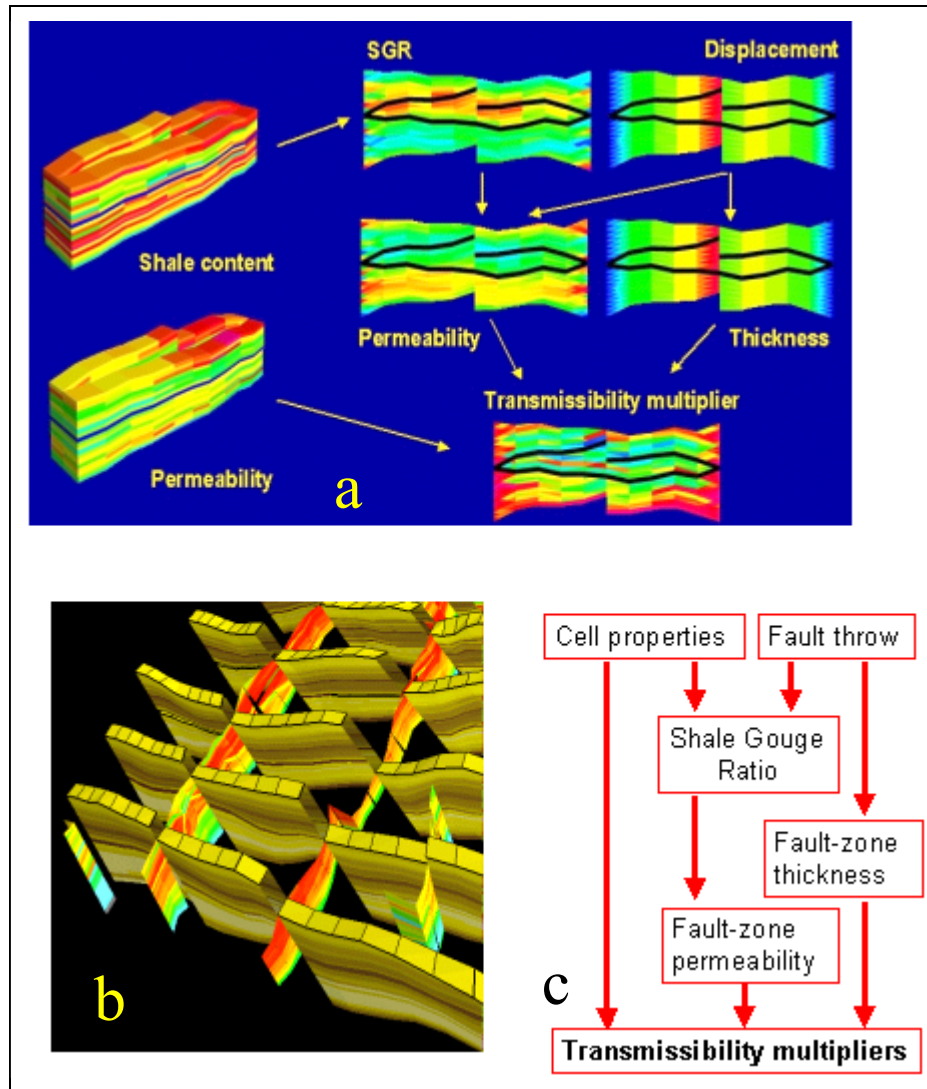


Fig. 7.1– TransGen method for calculation of transmissibility multipliers. a) Schematic procedure, b) areal analysis of shear zone permeability, c) modeling steps.. From Reference 43.

In this way, the detailed methodology proposed in this research starts with a systematic shear zone characterization based on the identification of deformation facies

and the analysis of geometries and petrophysical properties (**Fig. 7.2**). For primary analysis and characterization, the mandatory set of information should be extracted from core samples, well logs, and wellbore images with the correspondent integration with laboratory measurements and probe permeameter. From this step the variables that will be evaluated are: permeability, shale content, lithologic description, identification of diagenetic effects, facies analysis and geometrical characteristics. Shear zones should be sampled from many locations in a single fault plane and from different faults in order to have a representative rock profile to obtain high density permeability measurements and facies identification to quantify the degree of permeability reduction due to cataclasis.

The second step consists (**Fig. 7.2**) of a statistical analysis of deformation elements, the investigation of shear zone thickness and the characterization of faults according to throw, dip, azimuth, and degree of diagenesis. A correlation matrix should be then used to find valuable information, translated into trends, that allows to reduce the uncertainty. As seen in the findings in the Hickory Sandstone Member, each reservoir could exhibit a distinctive dependency of geological, geometrical and petrophysical variables.

In the case analyzed in the Lower Hickory as in many examples around the world, a useful correlation between fault throw and shear zone thickness can be incorporated to solve for our first unknown for the calculation of shear zone permeability. For this particular case in the Hickory sandstone, a probability function can be developed from information from the statistical relationship between fault throw and shear zone thickness (**Fig. 3.13**).

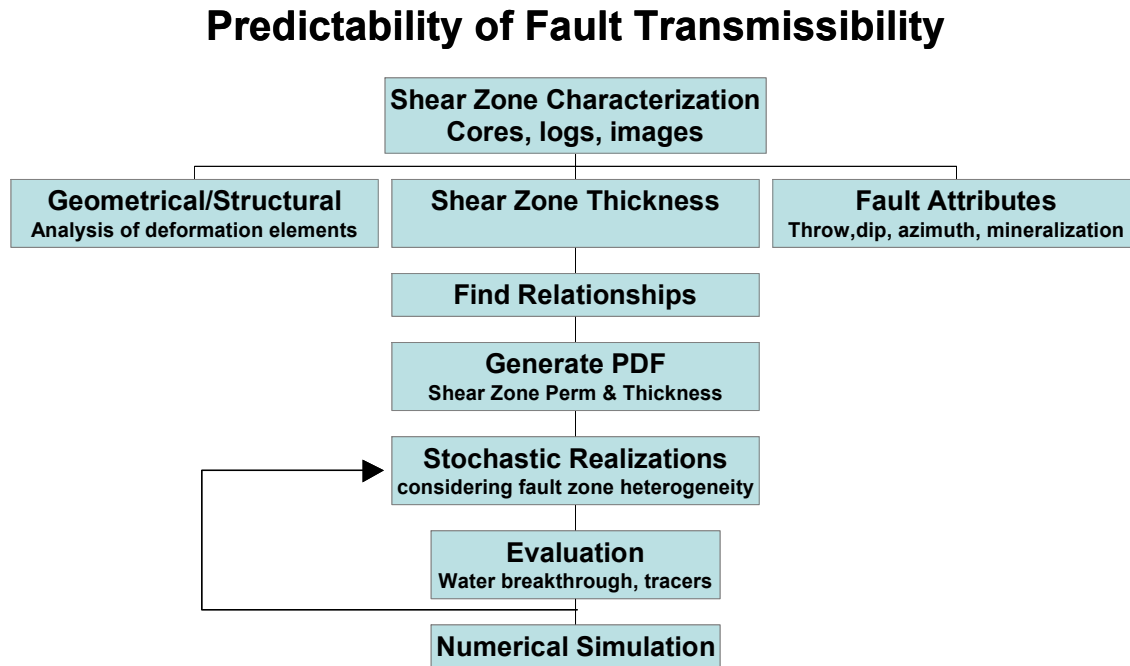


Fig. 7.2 - Method for the characterization of Shear zones and Integration to full field model simulation.

Then, demonstrated with the analysis of host rock properties versus the degree of displacement, we could reduce the uncertainty and have a probability function for the presence of specific shear zone permeability. Prior analysis suggested that the highly deformed elements are the key facies controlling the permeability field in the vertical and across fault plane. This foundation also can help in creating diverse model realizations of shear zone permeability based on the determination of the degree of cataclasis created by displacement and properties of host rock involved.

Having permeability and thickness fields as function of geological and petrophysical variables, multiple realizations of transmissibility multipliers can be

generated consistent with the modeling of the undeformed framework. These realizations might be evaluated using sector models for ranking purposes or for specific match with detailed or selective production. A spectrum of models with assigned probability could be then incorporated in simulation grids for final analysis under numerical solutions.

The advantage of considering the analysis of deformation and additional geological and petrophysical information over methodologies that pretend to predict fault sealing character using combination of shale smear and shale gouge ratio is that this proposed model can be effectively calibrated even for shale-free formations. We have measured the big impact that deformation causes in diverse lithologies reducing their flow capacities dramatically. Although shale indicators have been effectively tested in some fields, their quantification in terms of transmissibility is quite general and discrete.

Using the proposed methodology, transmissibility multipliers will be represented by a variable spectrum of values dependent on the prediction of shear zone permeability and thickness, and hopefully with a detailed match and evaluation with some dynamic field parameters, will reproduce the drainage anomalies that can be normally seen in diverse fields. In other words, the sealing character of the fault is a tridimensional attribute that is variable with time according to field dynamics.

7.2 Future Work

The lower Hickory sandstone member exhibits low shale content and the highly deformed sandstone elements were found to be most important features in the shear zone controlling overall permeability. It could be very important to investigate the effect of deformation in formations with higher shale content and how this material is incorporated in the shear zone.

The integration of results in a very detailed full field model for this Hickory aquifer should be the next step in order to match field tests and identify drainage anomalies in the area. This step should include tridimensional static reservoir modeling

with the integration of current investigations about the inherent heterogeneity of the Riley Formation and the incorporation of current findings.

We strongly recommend to investigate and incorporate the study of deformation elements and relationships between geological, structural and petrophysical attributes in diverse mature fields with enough information over the faulted region with the purpose to understand and predict drainage anomalies and extrapolate such results for the identification of untapped, isolated or effectively swept compartments in oil and gas reservoirs.

The continuous incorporation and study of detailed shear zone information by regions will help in building a more robust set of predictors useful for exploration evaluations in the determination of trap capacity, and in development stages, developing more precise understanding of the effects of many sub-seismic and small faults.

CHAPTER VIII

CONCLUSIONS

Hickory sandstone shear zones exhibit changes in permeability of two orders of magnitude between relative undeformed elements or protolith and highly deformed sandstones. Host rock characteristics clearly influence the permeability of highly deformed elements. Faults with throw greater than 10 feet generate highly deformed elements with permeability less than 8 md and directly correlated with host rock permeability.

Sensitivity analyses of the accuracy of permeability measurements and estimation of proportions for particular elements in fluid flow models demonstrate the importance of an accurate characterization of the low permeability elements because the elements exert primary control of overall fluid flow in the shear zone. From analytical and numerical techniques, the effect of overestimating permeability of the narrow, highly deformed elements as a result of low resolution in probe permeameter measurements is demonstrated. According to numerical and analytical analysis, the narrow, highly deformed elements should exhibit 5 times lower permeability than the values reported from probe measurements. These elements are frequently continuous throughout the core and represent the main features controlling fluid flow in the shear zone.

Density information derived from tomography indicates poor correlation between CT# and permeability in the highly deformed elements. Accordingly, the tridimensional picture from this technique is useful for continuity analysis, lithological discrimination, and control of trend analysis, but the specific recognition of narrow highly deformed elements can not be attempted.

A systematic methodology to incorporate the variable effect of faulting in a full field study should follow the steps: 1) analysis of core, images, and logs from the shear zone; 2) the identification of structural element geometry; 3) the analysis of correlations of shear zone thickness and individual elements and fault attributes; 4) the generation of

probability functions to be evaluated under stochastic realizations matching some field dynamic parameters; and finally, 5) the incorporation of shear zone effects under transmissibility multipliers. The complementary nature of conventional seal analysis using lithological considerations with this method, which accounts for the degree of deformation and the correlation with geological and petrophysical variables, will help to understand and predict complex transmissibility arrangements in small, sub-seismic faults.

Numerical simulation of detailed shear zone models clearly demonstrates the high impact of the precise characterization of highly deformed elements according to continuity and petrophysical properties. If a systematic approach is taken to identify and predict these elements, probability functions can be described in order to understand the whole permeability tensor in the shear zone. In this way, the incorporation of correlations found in this and previous work, such as the dependencies of the continuity and thickness of highly deformed elements with fault throw, the thickness of the overall shear zone with fault displacement, and host rock versus highly deformed element permeability, are important to characterize the shear zone as an important barrier for fluid flow.

Arithmetic upscalers can be effectively used to determine the along fault permeability, and then be integrated as a transmissibility multiplier in the direction parallel to the fault plane. Harmonic upscalers represent the permeability in the direction perpendicular to the orientation of the internal shear zone layering (across fault plane).

From a representative shear zone interval at NNR3_269, vertical flow simulation from models using original probe permeameter data predicted permeability between 3.28 to 4.072 md, a range that agrees satisfactorily with former analytical solutions (Ibañez, 2000) using harmonic averaging (3.2 md and standard deviation of 0.3 md). If specific considerations about the permeability of highly deformed elements are incorporated to estimate a more realistic permeability average, NNR3_269 shear zone exhibits a vertical permeability between 1.36 and 1.41 md.

The Harmonic upscaler, or the suggested across-fault permeability for the NNR4_404 shear zone, gives a low permeability estimate of less than 1 md. This very low permeability suggests an important barrier effect for the across-fault fluid flow in this specific fault location.

Although clay content affects shear zone permeability dramatically, the presence of clay material can be variable and not necessarily dependent of fault throw. This effect suggests that the degree of deformation must be incorporated in the fault sealing predictors to account for homogeneous, shale free formations.

From this work, we believe that further research in specific field examples will also show that deformation is the key factor for predicting communication along or across fault zones more than lithological considerations. Although shale content will affect hydraulic conductance of the fault severely, the protolith framework and diagenetic effects determine its presence.

REFERENCES

1. Knipe, R.J.: "Fault Systems and Migration Processes," *AAPG Bull.* (1998) 82, No. 13, Supplement.
2. Shengjie, Z.: "The Experimental Study on the Influence of Fault on Hydrocarbon Migration and Entrapment," *AAPG Bull.* (1999) 83, No. 11, 1881.
3. Wiprut, D.J. and Zoback, M.D.: "Fault Reactivation and Hydrocarbon Leakage Along a Previously Sealing Normal Fault in the Northern North Sea," *AAPG Bull.* (2000) 84, No. 13, Supplement.
4. Knipe, R.J.: "Juxtaposition/Seal Diagrams to Facilitate Fault Seal Analysis of Hydrocarbon Reservoirs," *AAPG Bull.* (1997) 81, 187.
5. Allan, D.F.: "The Use of 3-D Fault Visualization and Reservoir Juxtaposition Analysis in an Exploration Setting, U.S. Gulf of Mexico," *AAPG Bull.* (1997) 81, 30.
6. Naruk, S.J.: "Fault Seal Evaluation and Prediction," *AAPG Bull.* (2000) 84, No. 13, Supplement.
7. Kastning, E.: "Faults as Positive and Negative Influences on Groundwater Flow and Conduit Enlargement," *Hydrologic Problems in Karst Regions*, S.C. Csallany (ed.), West Kentucky University, Bowling Green, Kentucky, (1977), 193-201.
8. McCraig, A.: "Fluid Flow Through Fault Zones," *Nature*, (1989) 340, 600.
9. Watts N.: "Theoretical Aspects of Cap-Rock and Fault Seals for Single and Two-Phase Hydrocarbon Columns," *Marine and Petroleum Geology*, (1987) 4, 274.

10. Knipe, R.: "Faulting Processes and Fault Seal," *Proc., Structural and Tectonic Modeling and its Application to Petroleum Geology*, New York (1992) 325.
11. Bouvier, J.D., Kaars-Sijpesteijn, C.H., Kluesner, D.F., Onyejekwe, C.C., and Van Der Pal, R.C.: "Three-Dimensional Seismic Interpretation and Fault Sealing Investigations, Nun River Field, Nigeria," *AAPG Bull.* (1989) 73, No. 11, 1397.
12. Jev, B.I., Kaars-Sijpesteijn, C.H., Peters, M.P.A.M., Watts, N.L., and Wilkie, J.T.: "Akaso Field, Nigeria: Use of Integrated 3-D Seismic, Fault Slicing, Clay Smearing and RFT Pressure Data on Fault Trapping and Dynamic Leakage," *AAPG Bull.* (1993) 77, No. 8, 1389.
13. Lindsey, N., Murphy, F., Walsh, J, and Watterson, J.: "Outcrop Studies of Shale Smears on Fault Surfaces," *The Geological Modeling of Hydrocarbon Reservoirs and Outcrop Analogues*. S.S. Flint and I.D. Bryant (eds.), Blackwell Scientific, Oxford, U. K. (1993), 113-126.
14. Yielding, G., Freeman, B., and Needham, D.T.: "Quantitative Fault Seal Prediction," *AAPG Bull.* (1977) 81, No. 6, 897.
15. Sorkhabi, R., Suzuki, U., and Sato, D. : "Structural Evaluation of Petroleum Sealing Capacity of Faults," paper SPE 59405 presented at the 2000 SPE Asia Pacific Conference on Integrated Modelling for Asset Management, Yakohama, Japan, 25-26 April.
16. Younes, A. I.: "Shale Smear Evaluation Along the Hadahid Fault, Gulf of Suez, Egypt," *Stanford Rock Fracture Project Annual Report* (1998), 9, C1-9.

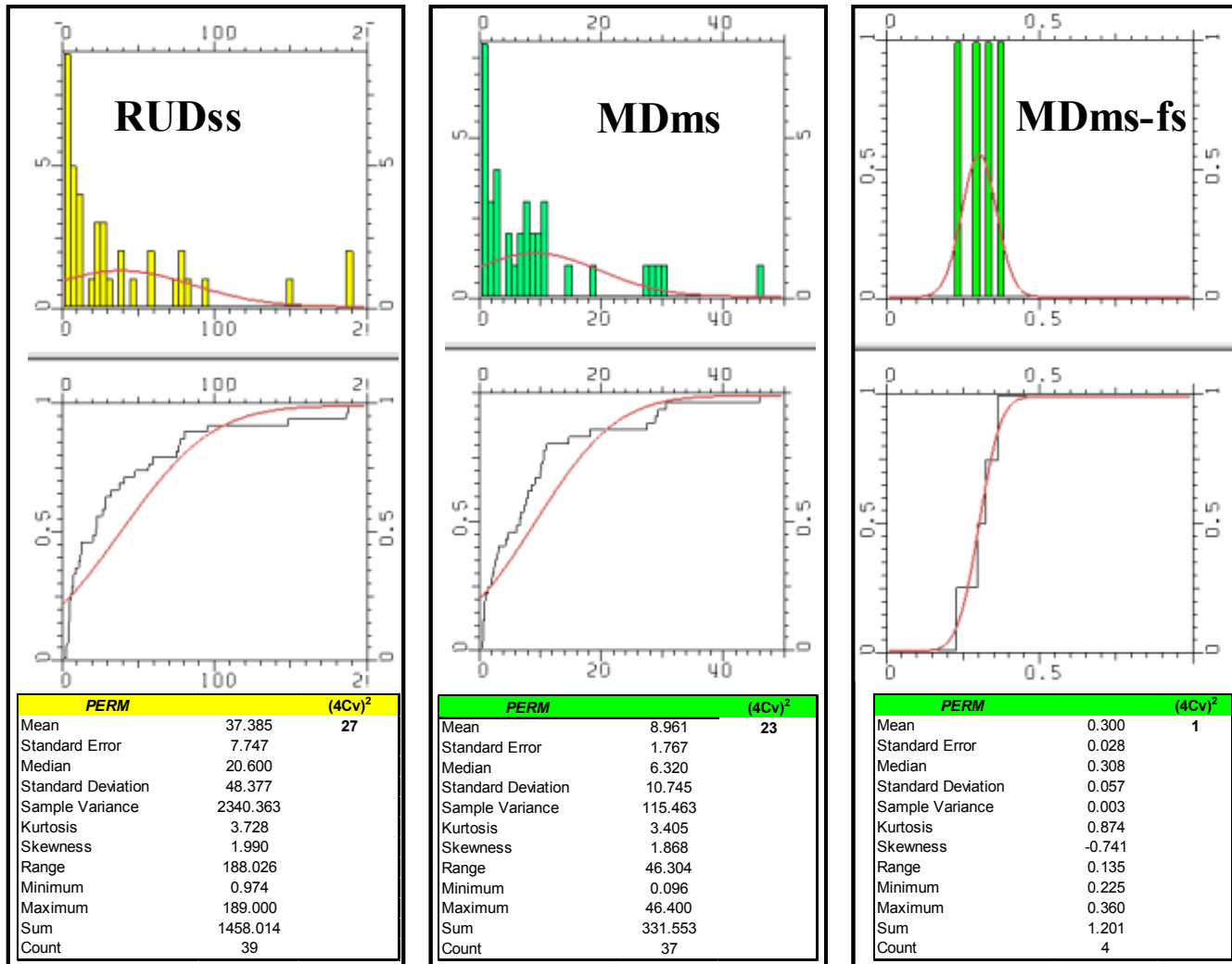
17. Gibson, R. G.: "Fault-zone Seals in Siliciclastic Strata of the Columbus Basin, Offshore Trinidad," *AAPG Bull.* (1994) 78, 1372-1385.
18. Flodin, E.A., Aydin, A., Durlofsky, L.J., and Yeten, B.: "Representation of Fault Zone Permeability in Reservoir Flow Models," paper SPE 71617 presented at the 2001 SPE Annual Technical Conference & Exhibition, New Orleans, 30 September -3 October.
19. Myers, R.: "Structure and Hydraulics of Brittle Faults in Sandstone," PhD dissertation, Stanford University, Palo Alto, California (1999).
20. Davies, R. K. and Handschy, J.W.: "Introduction to AAPG Bulletin Thematic issue on Fault Seals," *AAPG Bull.* (2003) 87, No. 3, 377.
21. Knipe, R.J.: "Juxtaposition/Seal Diagrams to Facilitate Fault Seal Analysis of Hydrocarbon Reservoirs," *AAPG Bull.* (1997) 81, 187.
22. Jourde, H., Flodin, E.A., Aydin A., Durlofsky, L.J., and Wen, X.: "Computing Permeability of Fault Zones in Eolian Sandstone from Outcrop Measurements," *AAPG Bull.* (2002) 86, No. 7, 1187.
23. Shipton, K., Evans, J.P., Robeson, K.R., Forster, C.B., and Snelgrove, S.: "Structural Heterogeneity and Permeability in Faulted Eolian Sandstone: Implications for Subsurface Modeling of Faults," *AAPG Bull.* (2002) 86, No. 5, 863.
24. Antonellini, M and Aydin, A.: "Effect of Faulting on Fluid Flow in Porous Sandstones: Petrophysical Properties," *AAPG Bull.* (1994) 78, No. 3, 355.

25. Ibañez, W. D.: "Characterization of the Structure and Permeability of Shear Zones in a Siliciclastic Aquifer," PhD dissertation, Department of Geology and Geophysics. Texas A&M University. College Station. (2000).
26. Wilson, J. S.: "High-Resolution Stratigraphic and Structural Characterization of the Fault-Partitioned Hickory Sandstone Aquifer, Mason County, Central Texas," M.Sc. thesis, Department of Geology and Geophysics. Texas A&M University. College Station. (2001).
27. Randolph, L.: "The Effects of Faults on the Groundwater System in the Hickory Sandstone Aquifer in Central Texas," M.Sc. thesis, Department of Geology and Geophysics. Texas A&M University. College Station. (1991).
28. Chester, F. and Logan, J.: "Implications for Mechanical Properties of Brittle Faults from Observations of the Punchbowl Fault Zone, California," *Pure and Applied Geophysics*, (1986) 124, 79.
29. Evans, J.: "Thickness-Displacement Relationships for Fault Zones," *J of Structural Geology* (1990) 12.
30. Jones, S. C.: "The Profile Permeameter: A New, Fast, Accurate Minipermeameter," paper SPE 24757 presented at the 1992 SPE Annual Technical Conference & Exhibition, Washington, DC, 4-7 October..
31. Wellington, S.L. and Vinegar, H.J.: "X-Ray Computerized Tomography," *JPT* (August 1987). 885

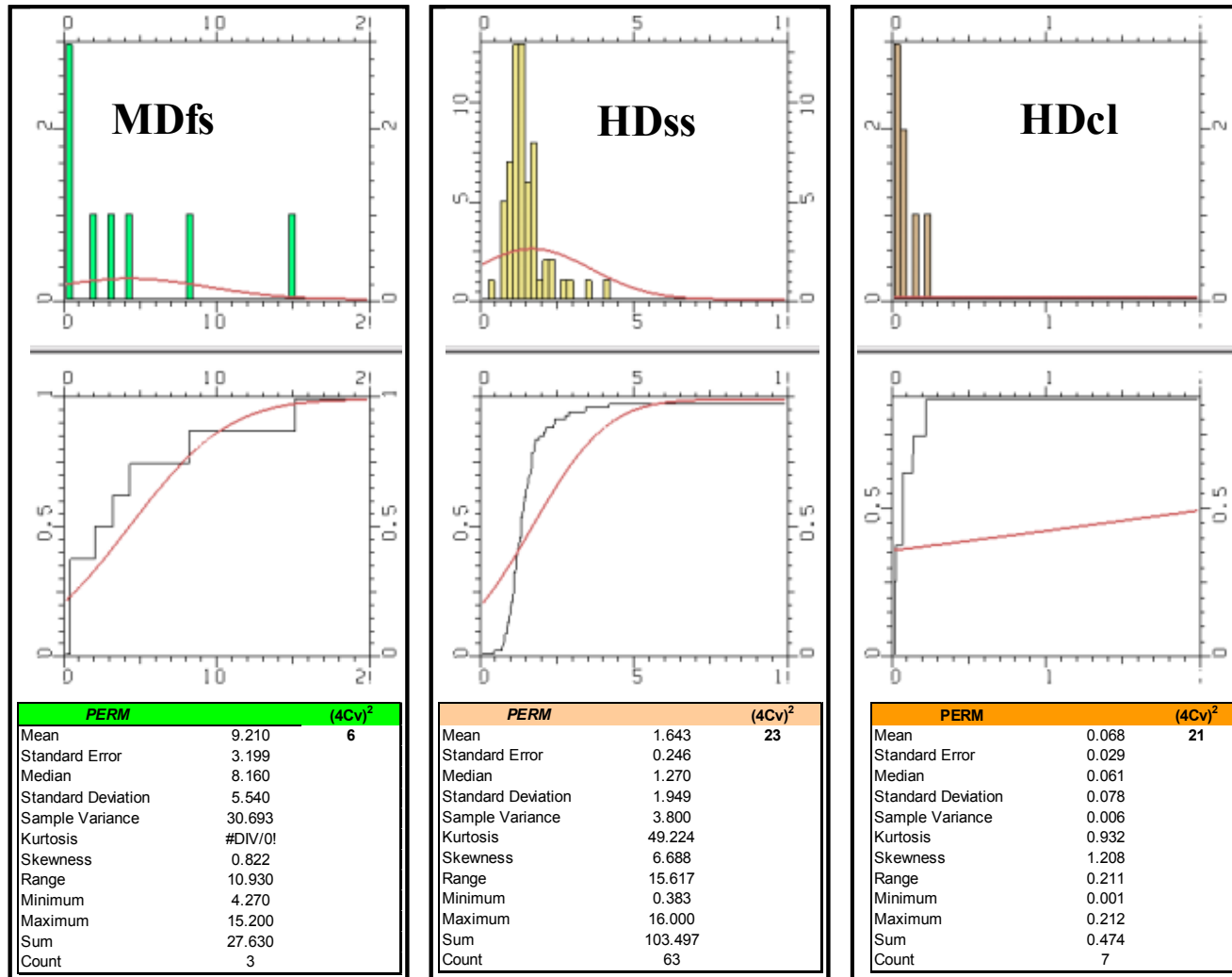
32. Jensen, J.L., Lake L.W., Corbett, P.W., and Goggin, D.J.: "Statistics for Petroleum Engineers and Geoscientists," *Handbook of Petroleum Exploration and Production*, 2, John Cubitt (ed.), Elsevier, New York (2000) Chap. 6, 128-129.
33. Gibson, R.: "Physical Character and Fluid-Flow Properties of Sandstone-Derived Fault Zones," *Structural Geology in Reservoir Characterization*, T. Daltaban and H. Johnson (eds.), Geological Society of London Special Publications, London (1998), 83-97.
34. Childs, C., Walsh, J., and Watterson, J.: "Complexity in Fault Zone Structure and Implications for Fault Seal Prediction," *Hydrocarbon Seals: Importance for Exploration and Production*, P. Moller-Pedersen and A. Koestle (eds.), Special Publication of the Norwegian Petroleum Society, Singapore (1997), No.7, 61-72.
35. Knott, S.: "Fault Seal Analysis in the North Sea," *AAPG Bull.* (1993) 77, No. 5, 778.
36. Robertson, E.: "Relationship of Fault Displacement to Gouge Breccia Thickness," *Mining Engineering*, New York (1983) V. 35, 1426-1432.
37. Randolph, L.: "The Effects of Faults on the Groundwater System in the Hickory Sandstone Aquifer in Central Texas," M.S. thesis, Department of Geology and Geophysics. Texas A&M University. College Station. (1991).
38. Davies, J.: "Statistics and Data Analysis in Geology," John Wiley and Sons, New York (1986). 646.
39. "Core Analysis Report for Texas A&M University NNR4-404 & NNR5-291," Core Laboratories, Midland, Texas (2003).

40. "Core Analysis Report for Texas A&M University Hydrology Samples (NNR3_269 and NNR4_300)," Core Laboratories, Midland, Texas (2003).
41. Collins, R.E.: "Determination of the Transverse Permeabilities of Large Core Samples from Petroleum Reservoirs," *J of Applied Physics* (1952) 23, No.4, 681.
42. Peaceman, D.W.: "A New Method for Calculating Well Indexes for Multiple Wellblocks with Arbitrary Rates in Numerical Reservoir Simulation," paper SPE 79687 presented at the 2003 SPE Reservoir Simulation Symposium, Houston, 3-5 February.
43. "TransGen", Badleys, www.badleys.co.uk/How_it_works.html, 22 July 2004. Accessed: August, 2004
44. Hollund, K: "An Advanced Fault Modeling Tool", www2.nr.no/documents/sand/research_areas/reservoir_characterization/faults/HAVANA_web2/havana.html, 23 July 2004.
45. Manzocchi, T., Walsh, J.J., Heath A., Nell, P.A.R., and Yieling, G.: "Fault Transmissibility Multipliers for Flow Simulation Models," *Petroleum Geoscience* (1999) 5, 53-63.
46. Manzocchi, T., Walsh, J.J., Heath A., Nell, P.A.R., and Yieling, G.: "A New Method for Attaching Fault Transmissibility Multipliers to Flow Simulation Models: Pros and Cons," *Faults, Fractures and Reservoir Flow*. FORCE Seminar, Stavanger (1999).

APPENDIX 1**STATISTICS OF DEFORMATION ELEMENTS**



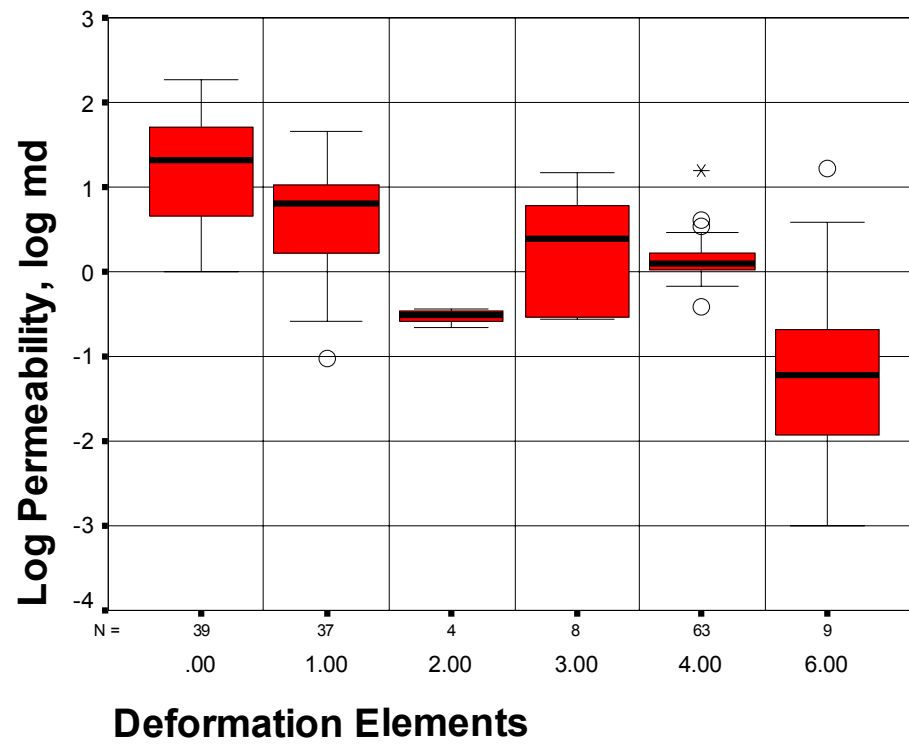
Statistical analysis of individual deformation elements in sample NNR4_404. RUDss: Relatively Undeformed sandstone
 MDms: Moderate Deformed medium sandstone MDms-fs: Moderate Deformed medium to fine sandstone



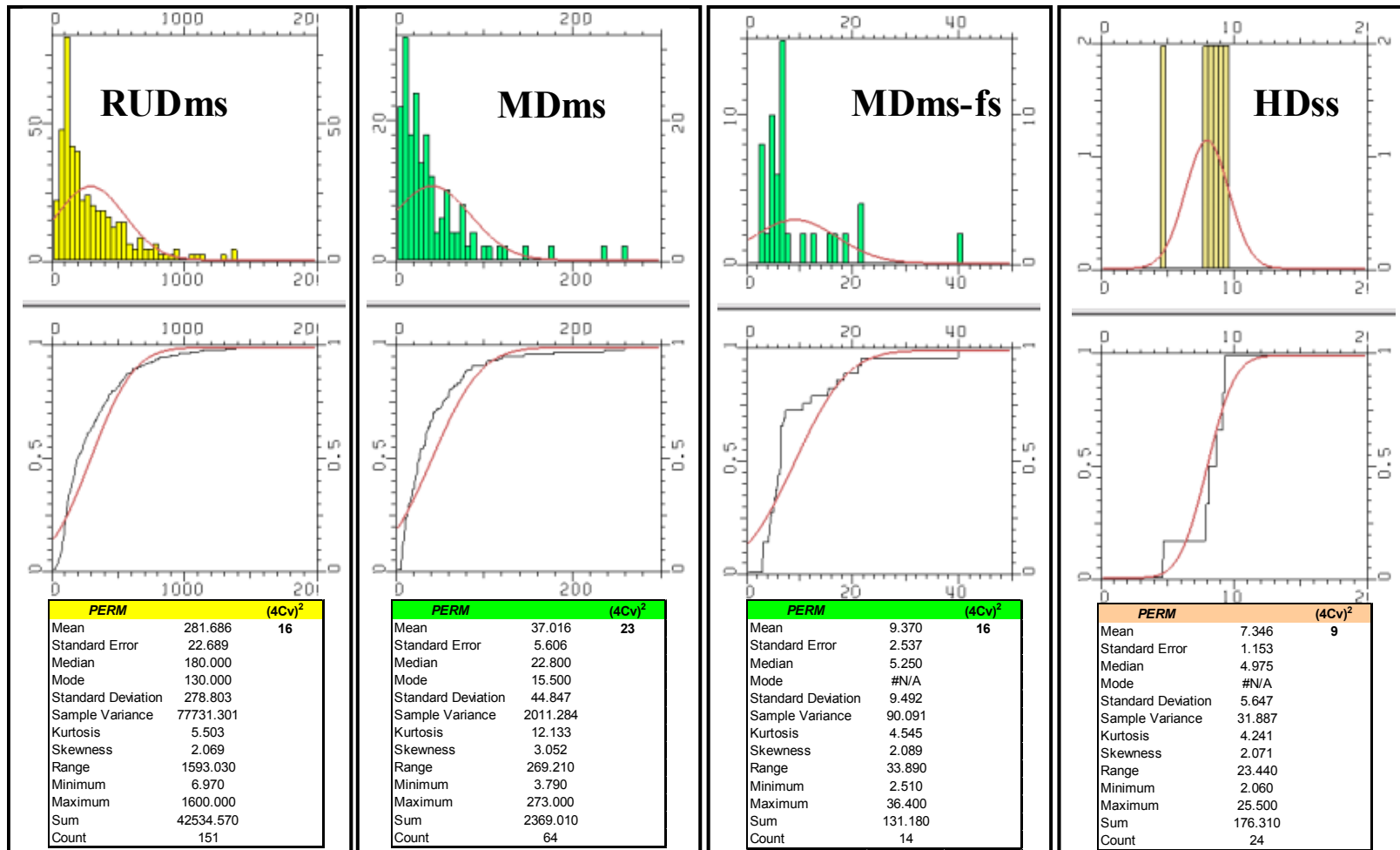
Statistical analysis of individual deformation elements in sample NNR4_404. MDfs: Moderate Deformed fine sandstone
 HDss: Highly Deformed sandstone HDcl: Highly Deformed clay

Descriptives					Descriptives					
	Facies		Statistic	Std. Error		Facies		Statistic	Std. Error	
logNNR4_404	.00	Mean	1.2069	.09885	3.00	Mean		.2305	.24782	
		95% Confidence Interval for Mean	1.0068			95% Confidence Interval for Mean	Lower Bound		-3.555	
			1.4070			Upper Bound		.8165		
			5% Trimmed Mean	1.2108				5% Trimmed Mean	.2222	
			Median	1.3139				Median	.3876	
			Variance	.381				Variance	.491	
			Std. Deviation	.61732				Std. Deviation	.70093	
			Minimum	-.01				Minimum	-.57	
			Maximum	2.28				Maximum	1.18	
			Range	2.29				Range	1.75	
			Interquartile Range	1.1309				Interquartile Range	1.3981	
			Skewness	-.057	.378			Skewness	-.101	.752
			Kurtosis	-1.005	.741			Kurtosis	-1.780	1.481
		1.00	Mean	.5760	.11307	4.00	Mean		.1297	.02813
	95% Confidence Interval for Mean		.3467		95% Confidence Interval for Mean		Lower Bound		.0734	
			.8053		Upper Bound			.1859		
			5% Trimmed Mean	.5975				5% Trimmed Mean	.1148	
			Median	.8007				Median	.1038	
		Variance	.473				Variance	.050		
		Std. Deviation	.68777				Std. Deviation	.22331		
		Minimum	-1.02				Minimum	-.42		
		Maximum	1.67				Maximum	1.20		
		Range	2.68				Range	1.62		
		Interquartile Range	.8901				Interquartile Range	.2073		
		Skewness	-.574	.388			Skewness	1.828	.302	
		Kurtosis	-.522	.759			Kurtosis	8.106	.595	
	2.00	Mean	-.5288	.04345	6.00	Mean		-1.1238	.47649	
95% Confidence Interval for Mean		-.6671		95% Confidence Interval for Mean		Lower Bound		-2.2226		
		-.3905		Upper Bound			-.0250			
		5% Trimmed Mean	-.5269				5% Trimmed Mean	-1.1494		
		Median	-.5118				Median	-1.2076		
		Variance	.008				Variance	2.043		
		Std. Deviation	.08690				Std. Deviation	1.42948		
		Minimum	-.65				Minimum	-3.00		
		Maximum	-.44				Maximum	1.21		
		Range	.20				Range	4.21		
		Interquartile Range	.1623				Interquartile Range	2.4202		
		Skewness	-1.042	1.014			Skewness	.231	.717	
		Kurtosis	1.385	2.619			Kurtosis	-.485	1.400	

Statistical analysis of the logarithm of permeability for individual deformation elements in sample NNR4_404



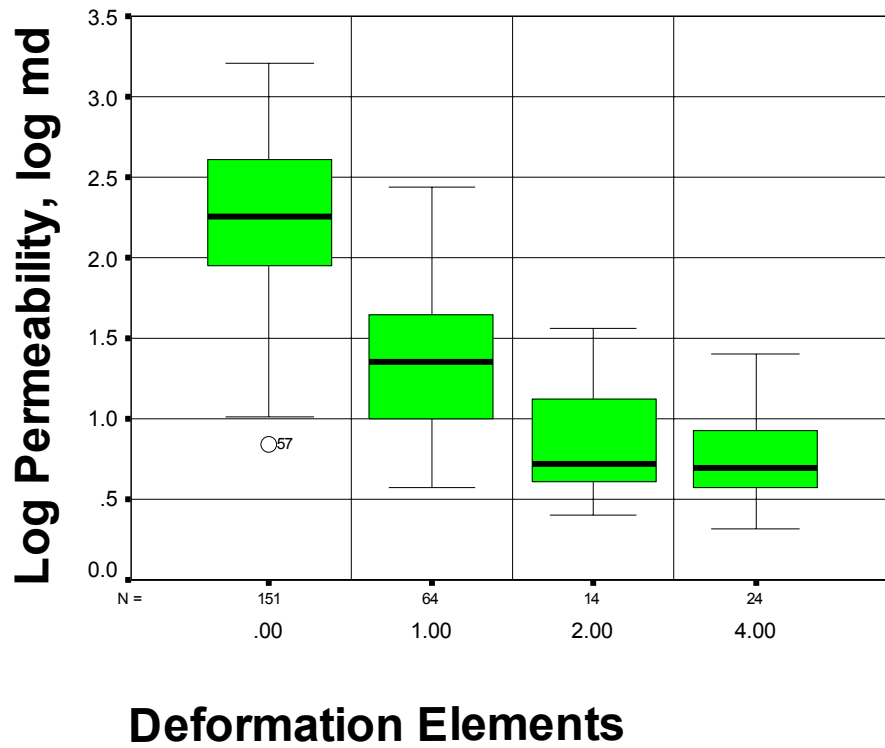
Boxplot of the logarithm of permeability by deformation elements in sample NNR4_404



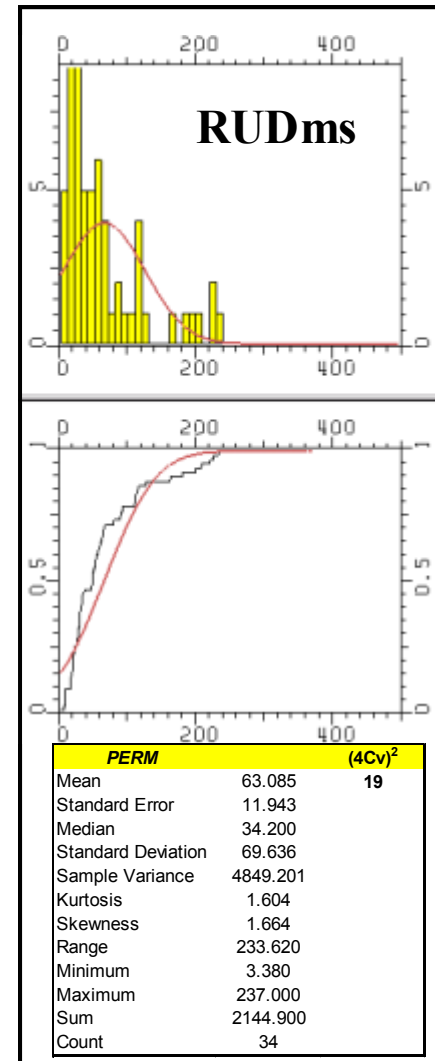
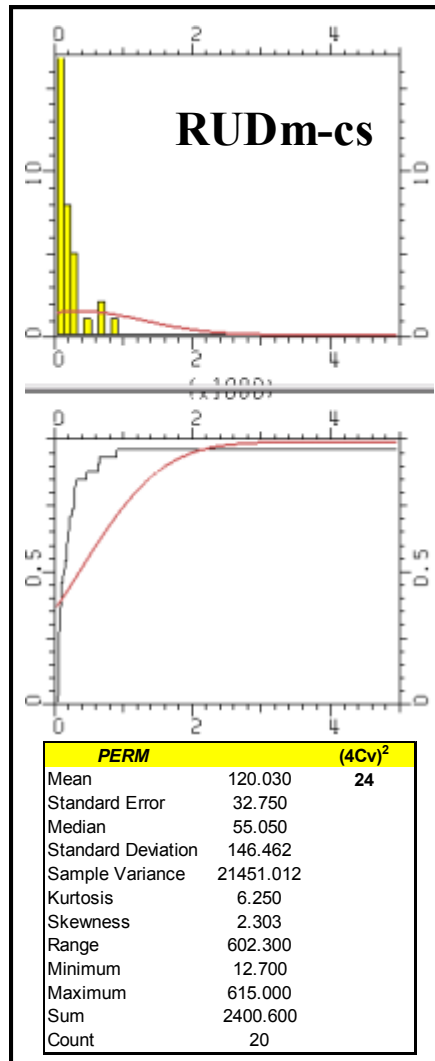
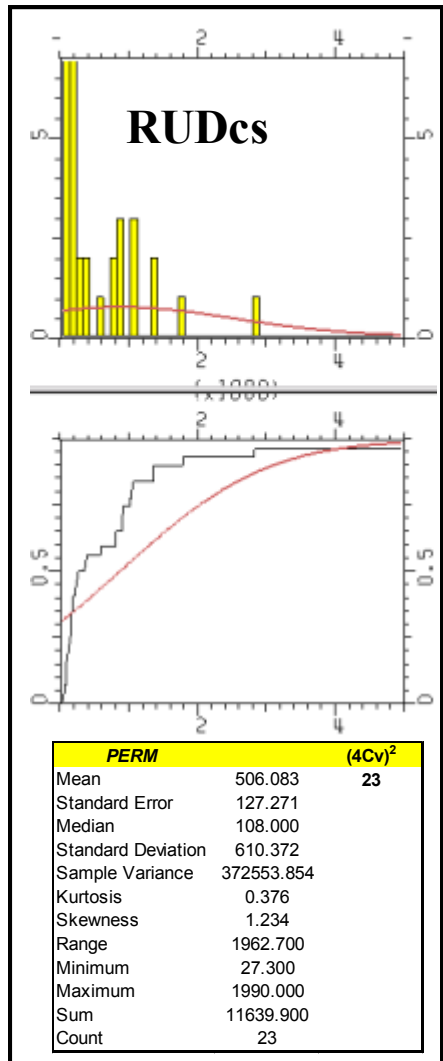
Statistical analysis of individual deformation elements in sample NNR5_291.

	Facies			Statistic	Std. Error			
logNRR5_291	.00	Mean		2.2506	.03636			
		95% Confidence Interval for Mean	Lower Bound	2.1788				
			Upper Bound	2.3225				
		5% Trimmed Mean		2.2637				
		Median		2.2553				
		Variance		.200				
		Std. Deviation		.44686				
		Minimum		.84				
		Maximum		3.20				
		Range		2.36				
		Interquartile Range		.6604				
		Skewness		-.404		.197		
		Kurtosis		.181		.392		
			1.00	Mean			1.3457	.05539
				95% Confidence Interval for Mean		Lower Bound	1.2350	
						Upper Bound	1.4563	
5% Trimmed Mean				1.3374				
Median				1.3579				
Variance				.196				
Std. Deviation				.44315				
Minimum				.58				
Maximum				2.44				
Range				1.86				
Interquartile Range				.6640				
Skewness				.141	.299			
Kurtosis				-.535	.590			
	2.00			Mean		.8223	.09306	
				95% Confidence Interval for Mean	Lower Bound	.6212		
					Upper Bound	1.0233		
		5% Trimmed Mean		.8047				
		Median		.7196				
		Variance		.121				
		Std. Deviation		.34820				
		Minimum		.40				
		Maximum		1.56				
		Range		1.16				
		Interquartile Range		.5625				
		Skewness		.910	.597			
		Kurtosis		-.103	1.154			
			4.00	Mean		.7777		.05436
				95% Confidence Interval for Mean	Lower Bound	.6652		
					Upper Bound	.8902		
5% Trimmed Mean				.7681				
Median				.6968				
Variance				.071				
Std. Deviation				.26632				
Minimum				.31				
Maximum				1.41				
Range				1.09				
Interquartile Range				.3784				
Skewness				.751	.472			
Kurtosis				.323	.918			

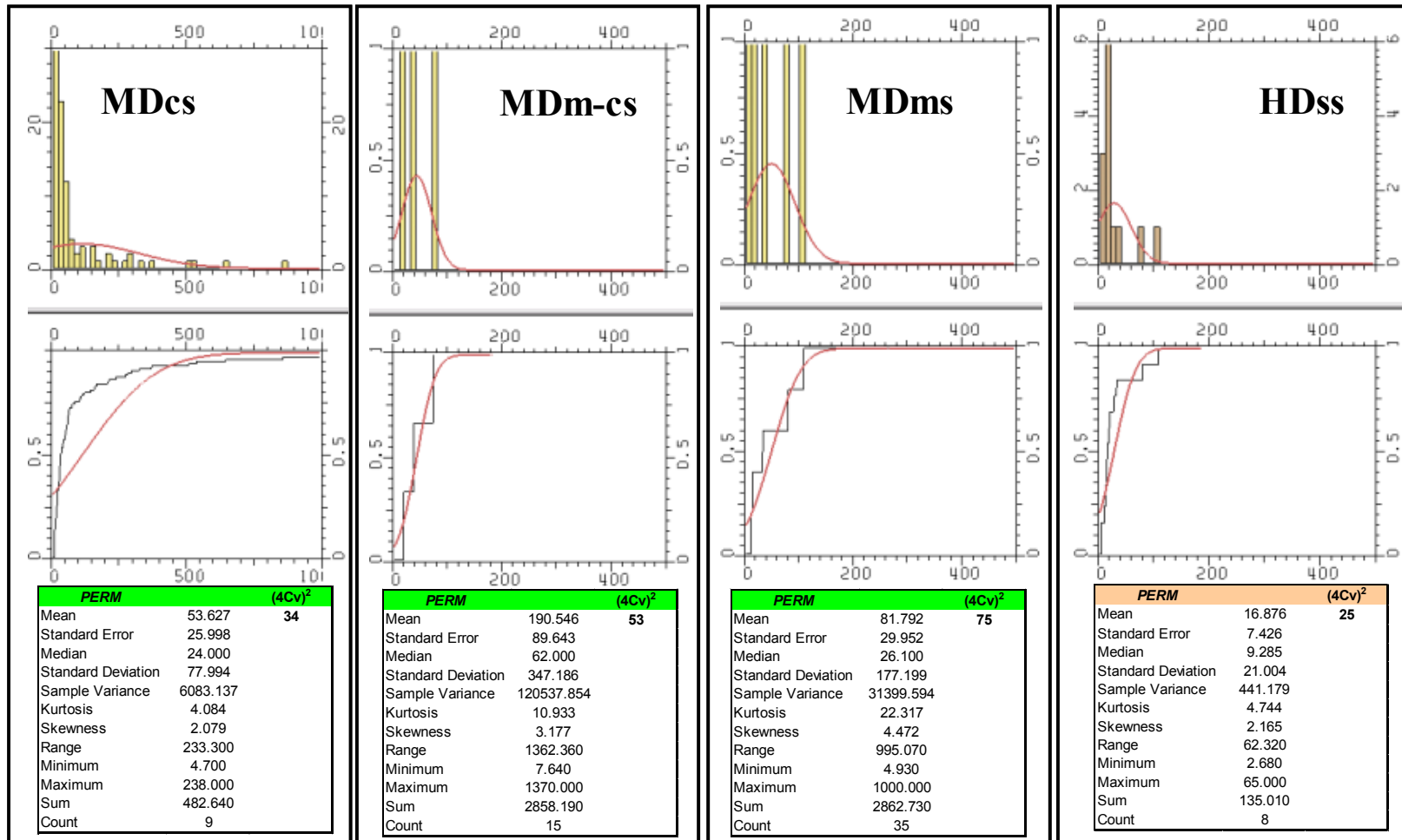
Statistical analysis of the logarithm of permeability for individual deformation elements in sample NNR5_291



Boxplot of the logarithm of permeability by deformation elements in sample NNR5_291

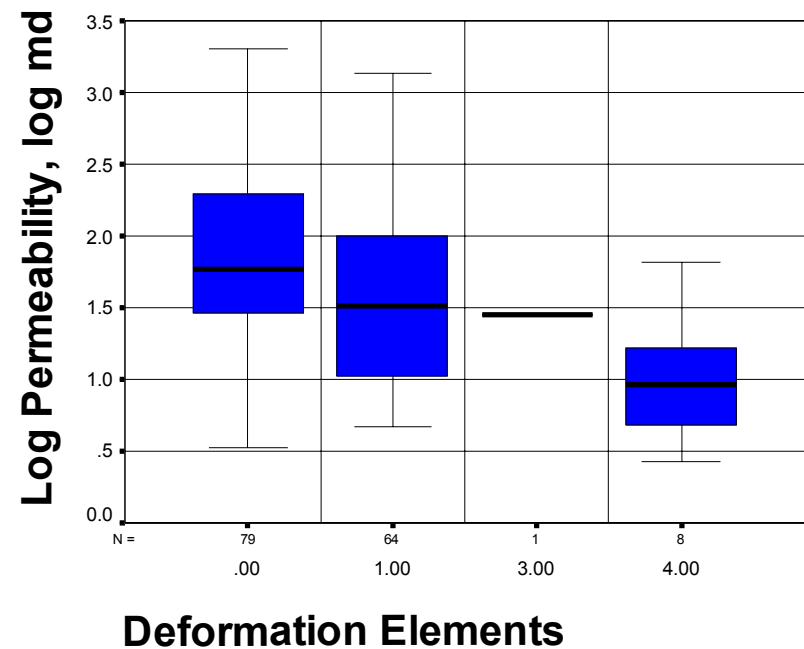


Statistical analysis of individual deformation elements in sample NNR4_300.

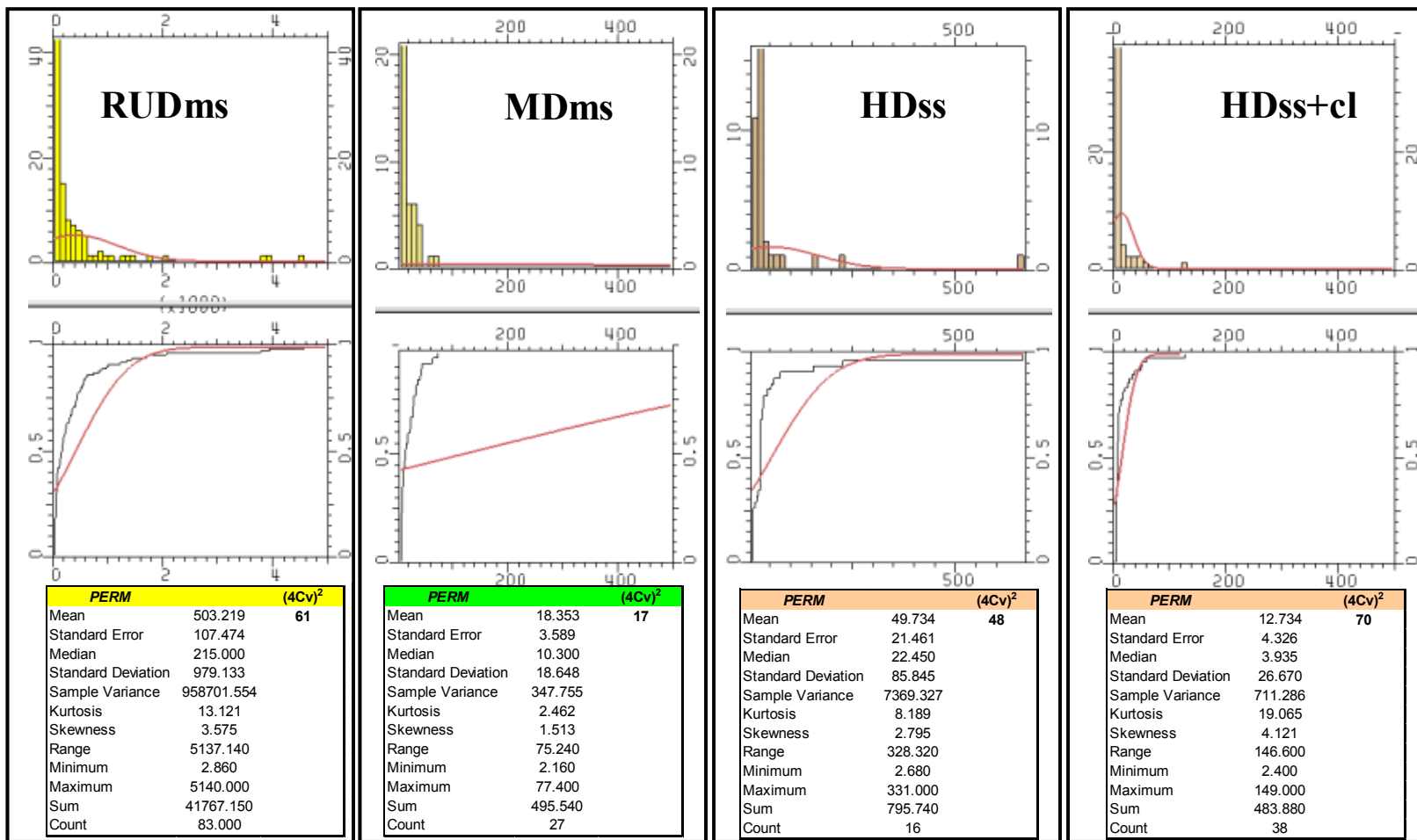


Statistical analysis of individual deformation elements in sample NNR4_300.

Facies		Statistic	Std. Error		
logNNR4_300	.00	Mean	1.8658	.07028	
		95% Confidence Interval for Mean	Lower Bound		1.7259
		Upper Bound	2.0057		
		5% Trimmed Mean	1.8534		
		Median	1.7716		
		Variance	.390		
		Std. Deviation	.62468		
		Minimum	.53		
		Maximum	3.30		
		Range	2.77		
		Interquartile Range	.8328		
		Skewness	.460		.271
		Kurtosis	-.187		.535
		1.00	1.00		Mean
95% Confidence Interval for Mean	Lower Bound			1.4092	
Upper Bound	1.7064				
5% Trimmed Mean	1.5314				
Median	1.5085				
Variance	.354				
Std. Deviation	.59489				
Minimum	.67				
Maximum	3.14				
Range	2.46				
Interquartile Range	.9988				
Skewness	.516			.299	
Kurtosis	-.287			.590	
4.00	4.00			Mean	.9957
		95% Confidence Interval for Mean	Lower Bound	.6075	
		Upper Bound	1.3840		
		5% Trimmed Mean	.9819		
		Median	.9676		
		Variance	.216		
		Std. Deviation	.46440		
		Minimum	.43		
		Maximum	1.81		
		Range	1.38		
		Interquartile Range	.7713		
		Skewness	.548	.752	
		Kurtosis	.150	1.481	

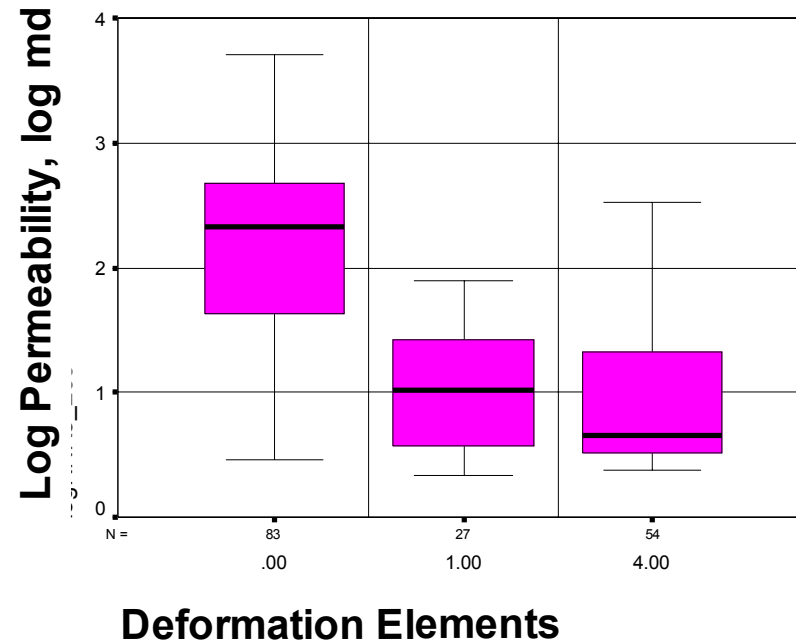


Statistical analysis and boxplot of the logarithm of permeability for individual deformation elements in sample NNR4_300



Statistical analysis of individual deformation elements in sample NNR3_269.

Facies		Statistic	Std. Error		
logNRR3_269	.00	Mean	2.1327	.08776	
		95% Confidence Interval for Mean	Lower Bound 1.9582 Upper Bound 2.3073		
		5% Trimmed Mean	2.1387		
	Median	2.3324			
	Variance	.639			
	Std. Deviation	.79949			
	Minimum	.46			
	Maximum	3.71			
	Range	3.25			
	Interquartile Range	1.0582			
	Skewness	-.325	.264		
	Kurtosis	-.523	.523		
	1.00	Mean	1.0299		.09276
			95% Confidence Interval for Mean		
5% Trimmed Mean			1.0233		
Median		1.0128			
Variance		.232			
Std. Deviation		.48199			
Minimum		.33			
Maximum		1.89			
Range		1.55			
Interquartile Range		.8698			
Skewness		.051	.448		
Kurtosis		-1.383	.872		
4.00		Mean	.9053	.07452	
			95% Confidence Interval for Mean		
	5% Trimmed Mean		.8549		
	Median	.6580			
	Variance	.300			
	Std. Deviation	.54760			
	Minimum	.38			
	Maximum	2.52			
	Range	2.14			
	Interquartile Range	.8118			
	Skewness	1.273	.325		
	Kurtosis	.673	.639		



Statistical analysis and boxplot of the logarithm of permeability for individual deformation elements in sample NNR3_269

VITA

Name: Jorge Enrique Nieto Camargo

Permanent Address: Calle 70 B # 2 – 14E Apt 301 Bogota - COLOMBIA

Education: Bachelor of Sciences in Geology. Degree awarded February 1989.
Universidad Industrial de Santander – Bucaramanga, Colombia.

Master of Science in Geological Sciences. Degree awarded
August 1997 - The University of Texas - Austin, TX.

Master of Science in Petroleum Engineering. Degree awarded
December 2004 - Texas A&M University – College Station, TX.

Experience: BHP Billiton, Houston, TX 2003 - Summer Intern

Empresa Colombiana de Petroleos ECOPETROL, Bogota,
Colombia. 1997 to 2002 - Reservoir Geologist

Bureau of Economic Geology, Austin, TX
1996 to 1997 - Graduate Research Assistant

Empresa Colombiana de Petroleos ECOPETROL, Bogota,
Colombia. 1990 to 1995 - Production Geologist

Universidad America, Bogota, Colombia
1992 to 1995 - Professor of Well Logging, Physical Geology and
Structural Geology.

Instituto Colombiano del Petroleo, Bucaramanga, Colombia
1989 to 1989 - Student - Thesis

E-mail: jen2973@spindletop.tamu.edu
mpnieto@yahoo.com